POLITECNICO DI MILANO

School of Industrial and Information Engineering
Master Thesis in Materials Engineering and Nanotechnology

Synthesis and optical properties of titanium nitride nanostructured thin films

Supervisor: Prof. Andrea Li Bassi
Co-supervisor: Beatrice Roberta Bricchi

Graduation thesis of:
Matteo Mazza, ID 899713

Academic Year 2019-2020

Abstract

Plasmonics has attracted a great attention over the last few decades due to the enticing physical mechanism arising from the interaction of light with resonant structures at the nanometer scale. Such a mechanism enables the confinement of light below the diffraction limit, allowing strong field enhancements. Therefore, plasmonics has being researched for many exciting and promising application fields, like electronics, biosensing, solar energy harvesting, cancer therapy, photocatalysis, photochemistry, telecommunications, metamaterials and optical storage of information.

Noble metals (especially gold and silver) have been commonly used as plasmonic materials because of their strong plasmonic response in the visible region of the electromagnetic spectrum, combined with small ohmic losses, high conductivity, biocompatibility and chemical stability. However, they suffer from many limitations like poor spectral tunability of the plasmonic response, high losses at optical frequencies caused by inter-band transitions, incompatibility with standard silicon manufacturing processes and poor thermal stability. As a consequence, the research of alternative plasmonic materials that could overcome these shortcomings has been recently pursued. In particular, a new class of materials has gained increasing attention: the transition metal nitrides (TMN's). Among these refractory ceramics, titanium nitride (TiN) has aroused the biggest interest, because its non-stoichiometric nature allows (in principle) to adjust its plasmonic response by varying the synthesis conditions. While TiN thin films have been already studied quite widely, a much lower knowledge and control over TiN nanostructures (e.g. TiN nanoparticles and nanoporous TiN films) have been achieved. In particular, TiN nanoporous systems could find exciting and promising applications in certain areas like solar energy harvesting, biosensing and photocatalysis, where their high specific surface may be exploited. However, the synthesis of such nanoporous TiN films still presents many challenges, mainly related to the severe oxidation that occurs because of their high surface area. For this reason, the objective of this thesis work is, first of all, the synthesis of nanoporous TiN films (characterized by a nanostructured morphology consisting of tree-like nanoparticles assemblies) and then, when it is possible, the investigation of their optical properties and plasmonic response. Even if PLD is not the conventional method for the fabrication of TiN films, it allows in principle to control the morphology, composition and structure of the deposit by playing with certain parameters. In this way, the correlation between such features and the optical properties of the films may be investigated.

First of all, we explored different combinations of laser energy density (fluence, 2 and 3.5 J/cm^2) and background N_2-H_2 gas pressure (from 5 up to 100 Pa) in order to obtain adherent and uniform films with nanostructured morphology, and to study the transition

from compact to nanoporous thin films in terms of density, structure and optical properties. We immediately dealt with the problem of oxidation, whose extent was so vast in highly nanoporous films that the titanium nitride characteristic features could not be easily observed. We hypothesized that oxidation was mainly due to oxygen incorporation either during deposition or after air exposure. Thus, we studied the effects of depositing a capping layer on top of the films (without opening the vacuum chamber) to try limit air exposure oxidation, and of using a higher laser fluence (i.e. 6.5 J/cm^2) to try to enhance the reactivity of nitrogen species in the plasma plume, hence limiting residual oxygen contamination during deposition. Then, we investigated the effect of heating the samples for 1 hr in two different atmospheres, vacuum and overpressure of N_2-H_2 (95-5%), and at two different temperatures, 300 and 550°C. Our goal was to reduce oxidation within the films, and to improve their crystallinity. Moreover, with the annealing in overpressure of N_2-H_2 we tried to enrich the films in nitrogen.

Deposition of continuous and uniform films with different morphology on Si and glass substrates was successfully achieved from the very beginning of the work. The capping layer allowed to reduce oxidation within the more porous samples, thus enabling the fabrication of low density tree-like nanostructured TiN films with absorption peaks in the Vis-NIR. The use of a higher laser fluence (i.e. 6.5 J/cm^2) instead led to the formation of nanoporous TiN films with the peculiar characteristic of being strong broad-band absorbers, hence being of potential interest for applications like solar energy harvesting and solar-thermophotovoltaics. Moreover, Raman spectroscopy and UV-Vis-NIR spectrophotometry suggested a strong influence of the annealing atmosphere and temperature on the TiN films structure and optical behavior. However, we were not able to measure neither the quantitative composition nor the charge carriers density of our samples, which is strongly related to the parameter characterizing the plasmonic response of a material (i.e. the plasma frequency). Further studies are necessary to understand the correlation between the optical behavior of such nanoporous TiN thin films and their composition, structure and charge carriers density, in order to achieve a deeper understanding and control on their plasmonic behavior.

Finally, we performed a first attempt of nitrogen ion beam-assisted deposition of a compact TiN thin film. We obtained very good results in terms of electrical properties (i.e. carrier density) and stoichiometry of the film. So, this approach could be further developed in future studies.

Sommario

La plasmonica, negli ultimi decenni, ha portato su di sé grandi attenzioni dovute al particolare fenomeno fisico che la caratterizza, il quale scaturisce dall'interazione della luce con una struttura risonante alla scala nanometrica. Grazie a questo meccanismo infatti la luce può essere confinata al di sotto del limite di diffrazione, aumentando così l'intensità del campo elettromagnetico locale. Dunque, la plasmonica è oggetto di svariate attività di ricerca rivolte a campi di applicazione entusiasmanti e promettenti, quali l'elettronica, il *biosensing*, la fotocatalisi, la fotochimica, la produzione di energia solare in pannelli fotovoltaici, la terapia contro il cancro, le telecomunicazioni, i metamateriali e l'archiviazione ottica di informazioni. I metalli nobili (soprattutto l'oro e l'argento) vengono comunemente usati come materiali plasmonici grazie alla loro forte risposta plasmonica nello spettro visibile combinata a perdite ohmiche ridotte, elevata conduttività, biocompatibilità e stabilità chimica. Tuttavia, l'utilizzo di questi materiali comporta diversi svantaggi, tra cui la limitata regolazione spettrale della risposta plasmonica, elevate perdite a frequenze ottiche causate da transizioni interbanda, bassa stabilità alle alte temperature e scarsa compatibilità con i processi standard di produzione del silicio. Di conseguenza, recentemente sono stati studiati e ricercati materiali plasmonici alternativi che ovviassero a tali problemi. In particolare, i nitruri dei metalli di transizione hanno attirato maggiore attenzione. In questa nuova classe di ceramiche refrattarie il nitruro di titanio (TiN) è il materiale che sta riscuotendo maggior interesse, siccome, data la sua natura non-stechiometrica, è teoricamente possibile regolarne le prestazioni plasmoniche attraverso le condizioni di sintesi. Mentre i film sottili di TiN sono già abbastanza studiati, sono stati acquisiti una conoscenza e un controllo molto minori circa le nanostrutture di TiN (come nanoparticelle o film nanoporosi). In particolare, i sistemi nanoporosi di TiN sono candidati promettenti per determinate applicazioni nelle quali la loro elevata area superficiale specifica potrebbe essere sfruttata, come ad esempio per la fotocatalisi, per il biosensing e per la produzione dell'energia solare. Tuttavia, la sintesi di tali film nanoporosi di TiN presenta ancora molte sfide perlopiù legate alla loro ossidazione, la cui entità è particolarmente severa a causa della loro elevata area superficiale. Pertanto, questo lavoro di tesi ha come primo obiettivo la sintesi di film sottili nanoporosi di TiN (caratterizzati da una morfologia nanostrutturata ad albero); dunque, quando possibile, lo studio delle loro proprietà ottiche e della loro risposta plasmonica. Sebbene la PLD non sia il metodo di deposizione convenzionale per i film di TiN, dà la possibilità di controllarne, in linea di principio, la morfologia, la composizione e la struttura giocando con determinati parametri. In questo modo è possibile esplorare la correlazione tra le sopra citate caratteristiche dei film e le loro proprietà ottiche e plasmoniche.

Per prima cosa dunque, abbiamo analizzato diverse combinazioni di densità di energia del laser (fluenza, 2 e 3.5 J/cm^2) e pressione del gas N_2-H_2 (da 5 a 100 Pa). Il nostro intento era quello di trovare le condizioni di deposizione ottimali per ottenere un film con morfologia nanostrutturata che fosse aderente ed uniforme su tutto il substrato. Inoltre, volevamo

studiare la transizione morfologica da film sottile compatto a nanoporoso dal punto di vista della variazione in densità, struttura e proprietà ottiche. Fin dall'inizio ci siamo imbattuti col problema dell'ossidazione, la cui entità era così significativa nei film più porosi che questi perdevano le caratteristiche tipicamente osservabili in un nitruro di titanio. Abbiamo ipotizzato che l'ossidazione dei film potesse essere perlopiù dovuta a due fenomeni: l'incorporazione di ossigeno durante la deposizione del film o dopo la sua esposizione all'aria. Dunque, abbiamo analizzato da un lato l'effetto prodotto dalla presenza di un film compatto protettivo depositato sopra i campioni senza aprire la camera da vuoto, nel tentativo di limitare l'ossidazione durante l'esposizione all'aria; dall'altro quello generato dall' utilizzo di una fluenza più alta (6.5 J/cm^2) durante la deposizione dei campioni, nel tentativo di aumentare la reattività dei radicali di azoto nella piuma e di limitare quindi l'incorporazione di ossigeno residuo in camera. In seguito, abbiamo studiato l'effetto del riscaldamento dei campioni per 1 ora a due diverse temperature, 300 e 550°C, e in due diverse atmosfere, vuoto e sovrappressione di N_2-H_2 (95-5 %). Il nostro obiettivo era ridurre l'ossidazione dei film e aumentarne la cristallinità. Inoltre, mediante il trattamento termico in sovrappressione di N_2-H_2 abbiamo cercato di arricchire i film in azoto.
La deposizione su substrati di silicio e vetro di film continui, uniformi, e di diverse morfologie è stata conseguita con successo sin dall'inizio del lavoro. Il film compatto protettivo ha ridotto notevolmente l'ossidazione per i film con porosità più elevata; in questo modo è stato possibile ottenere dei film di nitruro di titanio con morfologia nanostrutturata ad albero, caratterizzati da picchi di assorbimento nello spettro del visibile e del vicino infrarosso. L'utilizzo invece di una fluenza più elevata (6.5 J/cm^2) ha prodotto dei film di TiN nanoporosi contraddistinti da un forte assorbimento su tutto lo spettro dell'UV-Vis-NIR, risultando quindi di potenziale interesse per applicazioni che sfruttano la raccolta dell'energia solare.
Inoltre, la spettroscopia Raman e la spettrofotometria UV-Vis-NIR hanno suggerito una forte influenza dell'atmosfera e della temperatura utilizzate sulla composizione dei film di TiN e sul loro comportamento ottico. Tuttavia, non ci è stato possibile misurare né la composizione quantitativa né la concentrazione dei portatori di carica dei nostri campioni, la quale è significativamente legata al parametro che caratterizza la risposta plasmonica di un materiale (cioè la frequenza di plasma). Pertanto, sono necessari ulteriori studi per approfondire il legame che sussiste tra le proprietà ottiche di questi film nanoporosi di TiN e la loro composizione, struttura e densità di portatori; solo così si potranno raggiungere una conoscenza e una capacità di controllo maggiori sul loro comportamento plasmonico.
Infine, abbiamo compiuto un primo tentativo di deposizione assistita da bombardamento ionico (con ioni di azoto) per la fabbricazione di un film compatto di nitruro di titanio. Sono stati ottenuti risultati molto buoni in termini di densità di portatori di carica e di stechiometria del film; potrebbe dunque essere interessante sviluppare questo approccio in studi futuri.

Contents

Abstract **i**

Sommario **iii**

List of Figures **viii**

List of Tables **xi**

Introduction **xiii**

1 TiN thin films and nanoparticles: an overview **1**
1.1 TiN fundamental features 1
1.2 TiN thin films 3
1.2.1 General properties 3
1.2.2 Deposition techniques and properties tuning (state of art) 7
1.3 TiN nanoparticles 23
1.3.1 Plasmonic properties and applications 23
1.3.2 TiN NPs assemblies: nanostructured thin films 40
1.4 Objectives of this thesis 49

2 Experimental methods **51**
2.1 Pulsed Laser Deposition 51
2.1.1 RF ion source 55
2.2 Scanning Electron Microscopy 56
2.3 Raman Spectroscopy 57
2.3.1 Raman Spectroscopy of TiN 58
2.4 UV-Vis-NIR Spectrophotometry 59
2.5 Thermal treatments 61
2.6 Van der Pauw method (four-point probe) 62

3 Optimization of deposition parameters for nanostructured TiN thin films and strategies for oxidation reduction **63**
3.1 Growth of nanostructured TiN thin films by PLD 63
3.2 Strategies for oxidation reduction 75
3.2.1 Oxidation during deposition 76
3.2.2 Oxidation after air exposure 81

4 Effect of post deposition annealing on TiN nanostructured thin films 87
4.1 Effect of annealing atmosphere and temperature 88
4.2 Effect of annealing after strategies against oxidation 95

5 Ion Beam-Assisted Deposition of a compact TiN thin film 103

Conclusions and perspectives 108

Bibliography 112

List of Figures

Figure 1.1	Crystal structure of B1 TiN	1
Figure 1.2	Dielectric function of a B1 TiN film	4
Figure 1.3	EDOS for B1 TiN	5
Figure 1.4	Dielectric functions of TiN, Au, W and Mo	7
Figure 1.5	Figure of merit of TiN and Au for SPP light waveguiding	7
Figure 1.6	Raman spectra of TiN films – Ex. 1	11
Figure 1.7	Optical curves of TiN films – Ex. 1	11
Figure 1.8	Raman spectra of TiN films – Ex. 2	12
Figure 1.9	Raman spectra of TiN films – Ex. 3	13
Figure 1.10	Optical curves of TiN films – Ex. 2	14
Figure 1.11	Optical curves of TiN films – Ex. 3	15
Figure 1.12	Optical curves of TiN films – Ex. 4	15
Figure 1.13	Optical curves of TiN films – Ex. 5	15
Figure 1.14	Optical curves of TiN films – Ex. 6	17
Figure 1.15	Raman spectra of TiN films – Ex. 4	18
Figure 1.16	Dielectric functions of TiN films – Ex. 1	20
Figure 1.17	Raman spectra of TiN films – Ex. 5	21
Figure 1.18	Optical curves of TiN films – Ex. 7	22
Figure 1.19	Quality factors and dielectric functions of TiN and Au and ZrN	27
Figure 1.20	Near field intensity efficiencies for TiN and Au NPs	28
Figure 1.21	Explanation of the photothermal cancer therapy	29
Figure 1.22	Transmittance spectra for nanodisk arrays of TiN and Au	30
Figure 1.23	Illustration of solar-thermophotovoltaic systems	31
Figure 1.24	Optical properties of multilayer TiN-SiO_2 structure	32
Figure 1.25	Absorption efficiencies of TiN, C and Au nanospheres	32
Figure 1.26	Absorption cross sections of TiN NPs and Au nanoshells	34
Figure 1.27	Optical extinction of TiN NPs – Ex. 1	36
Figure 1.28	Absorbance of TiN NPs – Ex. 1	37
Figure 1.29	Optical extinction of TiN NPs – Ex. 2	37
Figure 1.30	Optical extinction of TiN NPs – Ex. 3	38
Figure 1.31	Optical extinction of TiN NPs – Ex. 4	39
Figure 1.32	Absorbance of TiN NPs – Ex. 2	39
Figure 1.33	Optical extinction of TiN NPs – Ex. 5	40
Figure 1.34	SEM images of TiN semi-shells array	41
Figure 1.35	Optical curves of TiN semi-shells arrays	41
Figure 1.36	SEM image of wrinkly nanostructured TiN film	42
Figure 1.37	SEM images of nanoporous TiN film	43
Figure 1.38	SEM images of urchin-like TiN architectures	43

Figure 1.39 SEM image of tree-like nanostructured TiN film 45
Figure 1.40 Density and mean pore volume values for tree-like TiN films 45
Figure 1.41 Raman spectrum of tree-like TiN film 46
Figure 1.42 Absorbance of nanostructured TiN film 46
Figure 1.43 Transmittance of nanostructured TiN film 46
Figure 2.1 Scheme of PLD apparatus 52
Figure 2.2 Different types of PLD deposition atmospheres 53
Figure 2.3 Scheme of SEM apparatus 56
Figure 2.4 Schematics of vibrational Raman process 59
Figure 2.5 Scheme of Raman apparatus 59
Figure 2.6 UV-Vis-NIR Spectrophotometer setups 61
Figure 2.7 Scheme of thermal treatments apparatus 62
Figure 3.1 SEM images of TiN films – Dep. @2 J/cm^2 66
Figure 3.2 SEM images of TiN films – Dep. @3.5 J/cm^2 67
Figure 3.3 TiN films density values for different pressures (1) 70
Figure 3.4 Raman spectroscopy – Results (1) 71
Figure 3.5 Raman spectra of amorphous TiO_2 71
Figure 3.6 Optical curves of TiN films – Dep. @2 J/cm^2 74
Figure 3.7 Tauc plot analysis of sample – Dep. @10 Pa N_2-H_2 74
Figure 3.8 Optical curves of TiN films – Dep. @3.5 J/cm^2 (1) 74
Figure 3.9 Pictures of TiN films on glass – Dep. @3.5 J/cm^2 75
Figure 3.10 TiN films density values for different pressures (2) 77
Figure 3.11 SEM images of TiN films – Dep. @6.5 J/cm^2 (1) 77
Figure 3.12 Raman spectroscopy – Results (2) 79
Figure 3.13 Optical curves and pictures of TiN films – Dep. @6.5 J/cm^2 79
Figure 3.14 Optical curves of TiN films – Dep. @3.5 J/cm^2 (2) 80
Figure 3.15 SEM images of TiN films – Dep. @6.5 J/cm^2 (2) 80
Figure 3.16 Optical curves and Raman spectra of the cap layer 82
Figure 3.17 Targets setup for capped TiN films deposition 82
Figure 3.18 Raman and optical spectra of capped TiN films (1) 84
Figure 3.19 Raman and optical spectra of capped TiN films (2) 85
Figure 3.20 Pictures of capped TiN films on glass 85
Figure 4.1 Raman spectra of annealed TiN films 90
Figure 4.2 Optical curves of annealed TiN films 93
Figure 4.3 Pictures of annealed TiN films 94
Figure 4.4 Raman spectra of annealed capped TiN films (1) 96
Figure 4.5 Raman spectra of annealed capped TiN films (2) 97
Figure 4.6 Pictures of annealed capped TiN films 97
Figure 4.7 Optical curves of annealed capped TiN films 99
Figure 4.8 Raman spectra of annealed capped TiN films (3) 102
Figure 4.9 Optical curves of capped TiN films 102
Figure 5.1 SEM images of TiN films – Dep. By IBAD 104
Figure 5.2 Raman spectra of TiN films – Dep. By IBAD 105
Figure 5.3 Optical curves of TiN films – Dep. By IBAD 106

List of Tables

Table 1.1	TiN NPs composition (1) – Literature	35
Table 1.2	TiN NPs composition (2) – Literature	36
Table 3.1	Examined combinations of fluence and pressure (1)	64
Table 3.2	Microbalance measurements (1)	69
Table 3.3	Microbalance measurements (2)	69
Table 3.4	Examined combinations of fluence and pressure (2)	77
Table 3.5	Examined combinations of fluence and pressure (3)	80
Table 3.6	Deposition conditions for capped TiN films	83
Table 4.1	Annealing conditions for the TiN films	88
Table 5.1	Resistivity values of TiN films – IBAD	106
Table 5.2	Hall measurements for annealed TiN film – IBAD	107

Introduction

Plasmonics has received significant attention recently, even though some of its applications have been known for ages. For example, the Lycurgus Cup of the ancient Romans and the glass decorating medieval cathedrals both get their vibrant colors from the optical plasmonic resonances induced in the metal nanoparticles embedded in the glass. When light interacts with a metal, the cloud of free electrons in the metal can sustain a wave of charge density oscillations on the metals surface known as plasmon. Such wave of charge density fluctuations can either propagate along a metal-dielectric interface (and so it is called surface plasmon polaritons SPP) or can exist as localized surface plasmon resonance (LSPR), which can be sustained by metallic nanoparticles [1]. In general, surface plasmons strongly couple light to the metal surface, hence greatly enhancing light-matter interactions. As a consequence, light can be confined in regions smaller than that predicted by the diffraction limit, and the local electromagnetic field is strongly intensified; these two physical phenomena are of special importance, because they open a horizon to new applications that could revolutionize our daily lives. For example, SPP can be exploited to fabricate optoelectronic circuits with subwavelength components, so that fast and scalable devices for information processing can be obtained [2]. On the other hand, LSPR can be exploited for biosensing, solar energy harvesting, heat assisted magnetic recording and therapeutic applications, due to the great enhancement of the local electromagnetic field and the strong optical absorption at the plasmon resonant frequency [3]. Moreover, metallic nanostructures like hierarchical films or nanoparticles assemblies, thanks to their plasmonic behavior combined with a high specific surface area, can be implemented for Surface Enhanced Raman Spectroscopy [4], solar-thermophotovoltaics, photodetecting [5] and photocatalysis [6].

Noble metals (especially gold and silver) have been conventionally used as plasmonic materials, thanks to their small ohmic losses, combined with their proven biocompatibility and chemical stability. However, problems from a wide range of disciplines awaiting a solution from the field of plasmonics cannot be solved with a limited pool of materials. In order to provide solutions to problems with different requirements such as operating at specific windows of the electromagnetic spectrum and at different ambient conditions, alternative materials are needed. In particular, a new class of materials has recently started gaining attention, the transition metal nitrides (TMNs), thanks to their high thermal and chemical stability combined with cost-effectiveness and CMOS compatibility. Among these refractory ceramics, titanium nitride (TiN) has been studied more widely because, being an intrinsically non-stoichiometric compound, its plasmonic response can be (in principle) spectrally tuned by adjusting the synthesis conditions. Whereas noble metals (due to their lower Ohmic losses) outperform TiN for waveguiding applications based on SPP light confinement [7], titanium nitride (which shows a near-field enhancement comparable to gold) is of significant interest for those plasmonic applications where the

localized surface plasmon resonance of either nanoparticles (NPs) or nanostructured films is exploited [8].

Nevertheless, such TiN NPs and nanostructured films have only been studied since a very short time, and further work is needed to cope with severe oxidation issues during their synthesis and to shine some light on their optical and plasmonic behavior. Thus, the aim of this work thesis is first of all the synthesis of nanoporous TiN thin films characterized by a nanostructured morphology consisting of tree-like nanoparticles assemblies, and then, if possible, the investigation of their optical properties and plasmonic response.

TiN thin films were grown on silicon and glass substrates by Pulsed Laser Deposition (PLD) technique, a PVD method that allows in principle to control morphology, composition and structure of the deposit by playing with some deposition parameters. PLD is not the conventional deposition method for compact TiN films, and has almost never been used to fabricate nanoporous TiN films or TiN NPs. Therefore, at the very beginning, we adopted as guidelines for the choice of the best deposition conditions the results of both the work on compact TiN thin film previously carried on in our laboratory [9] and of the research works found in literature. Starting from these results, we explored different combinations of deposition parameters, namely laser energy density (fluence) and background N_2-H_2 gas pressure, in order to obtain uniform and adherent films with morphology ranging from compact to tree-like and foam-like. This morphological transition was obtained quite easily by increasing the background gas pressure, similarly to what was already done in our laboratory for other materials (i.e. TiO_2 [10]). However, we had to face a serious oxidation issue for the more porous films, due to their very high surface area. Their oxidation extent was so significant that they resembled titanium oxide instead of titanium nitride. We hypothesized that oxidation was mainly due to oxygen incorporation either during deposition or after air exposure. Thus, we investigated the effects of protecting the underlying nanoporous films with a capping layer to try limit air exposure oxidation, and of using a higher fluence (i.e. 6.5 J/cm^2) to try to enhance the reactivity of nitrogen species in the plasma plume, hence limiting residual oxygen contamination during deposition. Afterwards, we submitted the obtained TiN films to heat treatments of 1 hr carried out at different temperatures (300 and 550°C) and atmospheres (vacuum and N_2-H_2), in pursuit of further limiting their oxidation and improving their crystalline quality. The optical properties of the synthesized TiN films were investigated as well, before and after the annealing process, in order to determine the possibility of tuning their plasmonic behavior. Finally, we performed a first attempt of compact TiN thin film ion beam assisted deposition (using a RF ion source integrated in the PLD apparatus) to try to increase the nitrogen content within the films.

The morphology of the synthesized TiN films was studied by Scanning Electron Microscopy (SEM). Raman Spectroscopy gave us indications regarding the qualitative composition of the films; in particular, it was useful in order to understand if either TiO_2 or TiN was obtained, and, in the latter case, it could give us an idea of the stoichiometry. Moreover, UV-Vis-NIR spectrophotometry, which was carried out at the Centre for Nanoscience and Technology (CNST) of the Italian Institute of Technology (IIT) in Milan, was performed for the analysis of the optical behavior. Four-point probe measurements

were done to explore the electrical properties of the compact TiN film deposited with the ion beam assist.

This thesis is divided into five chapters, organized according to the following scheme:

- **Chapter 1**. First of all, some general information on the structure and chemical composition of TiN together with its main properties and applications are reported. Then, an overview on TiN thin films is presented, with a special focus on the state of art regarding TiN thin films' oxidation issue, post-deposition annealing and growth by Pulsed Laser Deposition. The next section is dedicated to TiN nanoparticles, and it is quite extended. A first part introduces the plasmonic behavior of metal nanoparticles. Then, the main fabrication techniques, properties and applications of TiN NPs are described. The focus is on the possibility of tuning the optical properties of TiN NPs by varying the synthesis conditions. Finally, at the end of the section, the state of art regarding nanostructured TiN thin films is reported, with particular attention to their morphology and optical properties. The last part of the chapter contains the detailed exposition of the objectives of this thesis work.

- **Chapter 2**. The experimental setup used during this work is described, including both synthesis and characterization of the films. First, the Pulsed Laser Deposition (PLD) apparatus is presented focusing on the physical processes at the basis of its operation. Then, a brief presentation of the employed characterization techniques is reported, in the following order: Scanning Electron Microscopy (SEM), Raman Spectroscopy, UV-Vis-NIR spectrophotometry, and 4-point probe electrical measurements in the van der Pauw geometry.

- **Chapter 3**. First of all, it deals with the optimization of deposition parameters for nanostructured TiN thin films. Then, the morphological transition from compact to tree-like TiN films is explored in terms of structure and optical properties variation. A main focus is put on the oxidation issue we had to face during the fabrication of the nanoporous TiN films. The different strategies adopted to solve this problem are described, and, finally, the best among the obtained results are reported.

- **Chapter 4.** It concerns the effects of post deposition annealing on the obtained nanostructured TiN films, both before and after the strategies against oxidation have been adopted. Moreover, different combinations of annealing conditions are considered. Raman and optical spectra of our samples before and after heat treatment are compared, in order to discuss the possibility of tuning their properties.

- **Chapter 5.** It is a brief chapter, where a first attempt of ion beam assisted deposition of a compact TiN thin film is presented.

A short summary of the thesis work follows, highlighting the main achievements reached and pointing out possible future developments and perspectives.

During this work I personally performed the synthesis of the samples by PLD technique, and performed the subsequent heat treatments. Moreover, I carried out SEM, Raman spectroscopy, UV-Vis-NIR spectrophotometry and electrical measurements, dealing with the following data elaboration and analysis.

TiN thin films and nanoparticles: an overview

1.1 TiN fundamental features

Titanium (electronic configuration *[Ar] $3d^2 4s^2$*) is a well known element belonging to the IV_b group of the periodic table. Its four valence electrons are able to bond with the *p* electrons of nitrogen (electronic configuration *[He] $2s^2 2p^3$*), constituting titanium nitride (TiN).
This transition metal nitride can be present in different phases, among which the most stable one is B1-TiN. The latter is characterized by a cubic rocksalt crystalline structure (Fig. 1.1) and a bright gold-like color.

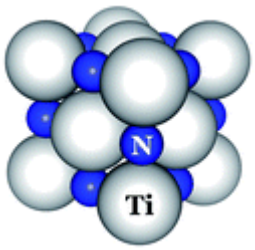

Figure 1.1 : Crystal structure of B1-TiN. Taken from [11].

Titanium nitride is intrinsically a non-stoichiometric compound, since its lower thermodynamic stability with respect to titanium oxides makes it highly prone to oxidation [12]. It is very tough to synthesize stoichiometric TiN, and it is practically impossible to completely avoid surface oxide formation and oxygen incorporation during its synthesis and production, especially in atmospheric or poor vacuum environments. While for bulky TiN coatings surface oxidation is not detrimental to their main functionalities, on the other side, for nanometric thin films, the surface to volume ratio gets so high that oxidation becomes a crucial issue. Furthermore, for nanostructured thin films and nanoparticles the role of oxidation becomes even more dominant and hard to control. These topics will be deeply discussed in section 1.3.2.

Titanium nitride has several interesting properties, which make it a well-established material in various industry sectors. It is characterized by very high hardness, strong resistance towards abrasion and corrosion, relative inertness, low friction coefficient, high chemical and thermal stability (thanks to a high melting point, T_m=3000°C) [13]; therefore it has been used for decades for protective coatings and cutting tools [14]. Moreover, its gold-like bright yellow appearance and color tunability by simply varying the stoichiometry makes it an appealing material for decorative applications [15]. Another main application of TiN is in the field of semiconductor industry, where it is widely used as diffusion barrier in CMOS manufacturing process, thanks to its good electron conductivity and mobility mixed with a perfect compatibility with silicon technology and a good barrier action towards copper diffusing from the chip interconnects [16]. In addition, its electronic properties combined with a refractory character make it a good material for Ohmic and Schottky contacts in microelectronic devices [17]. Thanks to its non-cytotoxical nature, titanium nitride can also be used to protect underlying materials in orthopedic prosthesis [18]. Finally, TiN has been taking a spot in the upcoming field of plasmonics, where the resonant interaction between light and electrons in metal nanostructures is exploited for various applications. This topic will be discussed deeper in the following sections.

1.2 TiN thin films

1.2.1 General properties

B1-TiN films has been studied since the 1930s and have been systematically grown since the 1970s. Nowadays titanium nitride is considered as one of the most technologically important materials thanks to its peculiar features.
In the following paragraphs first of all a brief overview about TiN main properties is presented; afterwards an overview of the state of art regarding TiN thin films properties-tuning by the most common deposition techniques is exposed.

TiN optical and electronic properties

Titanium Nitride exhibits a workfunction value WF ~ 3.75 eV, which coincides with the electron affinity range for most of semiconductors [19]. Therefore, by selecting appropriate semiconductors like Gallium Nitride (GaN) [17] or n-type Silicon [20], respectively Ohmic contacts or Schottky barriers can be developed. Moreover, the possibility to achieve a good lattice match between TiN and such semiconductors may enable the epitaxial growth of these heterojunctions.

Another fundamental property of B1-titanium nitride is the comparable or even higher direct current (DC) conductivity than that of titanium, combined with a superior optical behavior in terms of plasmonic potential. In fact, in a good optical conductor intraband and interband absorptions are not overlapping (i.e. the valence electrons are strongly bound and have a quite deep energy with respect to the Fermi level) and therefore the conduction electrons are interacting with light without much screening. In other words, a good optical conductor should exhibit negative real permittivity (real part of the dielectric function ε_1), with a clear and steep crossing to positive values at the wavelength region where the plasmonic performance is desired, while its imaginary permittivity (imaginary part of the dielectric function ε_2) should be the smallest possible in the entire spectrum, in order to have minimum optical losses [12].
The latter conditions are fully satisfied by B1-TiN (as observable in Fig. 1.2), and the reason lays in its electronic structure. By looking at the electron density of states (EDOS) (Fig. 1.3) calculated from the band structure, it is understandable how the spectral separation of interband and intraband transition in B_1-TiN is directly linked to the energy shift of Ti*3d* states from 0.5-3 eV below the Fermi level (for *hcp*-Ti) to 3-6 eV below the Fermi level, which is caused by the hybridization of Ti*3d* and N*2p* valence electrons during Ti*3d*-N*2p* bond formation. Besides, the *d* electrons of titanium which do not take part in the hybridization between Ti*3d* and N*2p* orbitals give rise to the electronic

conductivity of TiN. Fig. 1.3 depict the electron density of states of B1-TiN, showing two distinguishable regions of occupied states:

a) From -8 eV to -3 eV: strong hybridization of *d* electrons of Ti with *p* electrons of N gives the partial covalent bonding of TiN and the experimentally observed interband transitions. In particular, the transitions from the shoulder and the peak of the EDOS located at around -3.5 eV and -5.5 eV (and denoted in Fig. 1.3 as E_{01} and E_{02}, respectively) towards the unoccupied Ti-*d* states above the Fermi level generate two absorption bands which may be observed in TiN absorption spectra [21]. Therefore, all the titanium nitride interband transitions occur from nitrogen *p* orbitals to titanium *d* orbitals, according to the selection rules for photonic excitation ($\Delta l = 0, \pm 1$).
The lowest energy absolute value where the partial EDOS of N-*p* states is different than zero is also called cut-off energy, and represents the threshold at which the interband losses contribute to the optical response. The cut-off energy value for TiN is around -2.48 eV. It should be taken into consideration that the energy position of N-*p* EDOS' peak and shoulder can shift depending on TiN stoichiometry (N/Ti ratio) [22]. Higher N/Ti ratios have been proven to reduce the lattice parameter of Ti_xN_y, leading to a modification of the Brillouin Zone and of the band structure which redshifts the interband transitions E_{01} and E_{02} [23].

b) From -3 eV to E_f: the energy states are mainly filled by titanium *d*-electrons, and above the Fermi level the unoccupied states are mainly of metal's *d* character. TiN's electronic conductivity comes from the fact that the Fermi level intercepts this partially-filled *d* band.

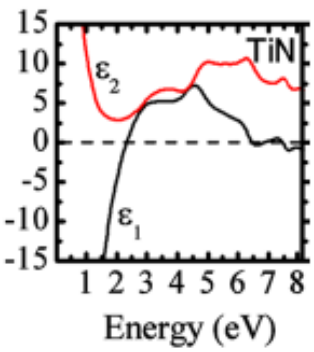

Figure 1.2: Real and imaginary part of TiN dielectric function calculated by density functional theory (DFT). Taken from [21].

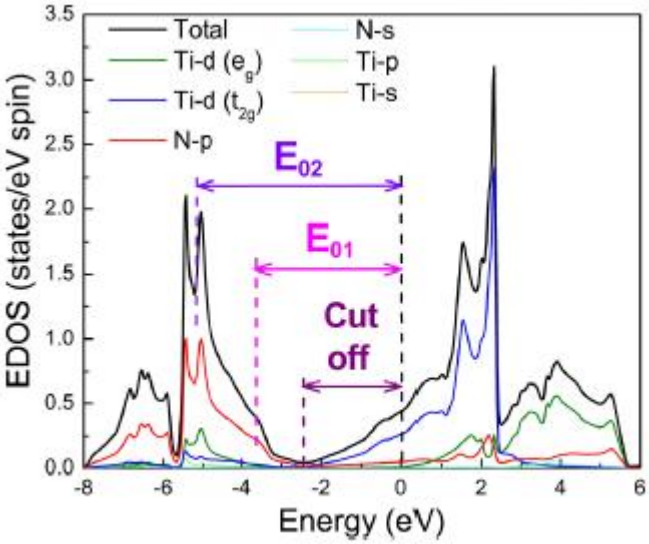

Figure 1.3: Electron density of states for TiN in the B1 structure. Zero energy stands for the Fermi level. The vertical dashed purple, magenta and blue lines denote the cut-off energy and the energy positions of the two interband transitions E_{01} and E_{02}, respectively. Taken from [24].

It should be mentioned that the gold-like color of TiN is due to its reflectivity edge's spectral position, which lays in correspondence of the so called *screened plasma energy* E_{ps}. At this energy the real part of the dielectric function ε_1 goes to zero. While at energies lower than E_{ps} (where $\varepsilon_1 < 0$) the reflectivity is high due to the interaction between light and conduction electrons, at energies higher than E_{ps} (where $\varepsilon_1 > 0$) the reflectivity goes down and light propagation (attenuated by some dielectric losses) is allowed. The calculated values of E_{ps} range from 2 to 2.95 eV (λ_{ps} = 620 and 420 nm, respectively) and directly depend on TiN_x stoichiometry: stoichiometric TiN (x = 1) has E_{ps} = 2.65 eV (λ_{ps} = 468 nm) and shows a bright-yellow appearance; overstoichiometric TiN (x > 1) is instead reddish-brown and more opaque [12]. In fact, increasing the nitrogen content x the number of free electrons decreases, thus reducing the light reflected by the film as well as its brightness. Moreover, since the *unscreened plasma frequency* ω_{ps} is proportionally depending on the carrier density *n*, an higher nitrogen content x leads to a lower free electrons density and, as follows, to a red-shifted plasma reflectance edge [3].

TiN films as plasmonic materials

The coupling between the electromagnetic radiation and the surface charge density oscillation results in a longitudinal wave evanescently confined along film's perpendicular direction: the Surface Plasmon. Because of its metallic character, titanium nitride can sustain these so called Surface Plasmon Polariton modes (SPPs) at its film surface. In this way, light is strongly coupled to the metal surface, thus greatly enhancing light-matter interaction. This leads to a local electromagnetic field intensification and to the possibility

of light confinement below the diffraction limit. The surface plasmon resonance frequency $\omega sp = \frac{\omega ps}{\sqrt{1+\varepsilon d}}$ is directly related to the screened plasma frequency ωps.

A crucial parameter for plasmonic material selection and design is the quality factor of the SPP resonance (Q_{SPP}), in fact the most important question is not whether a resonance can be sustained or not, but which is its quality. The quality factor for a plasmonic material can be defined as the ratio between the enhanced local field to the incident local field. In the case of surface plasmon polaritons propagating along planar interfaces, such ratio can be expressed in terms of the complex propagation wavevector k_x. More specifically, Q_{SPP} can be defined as the ratio of the real part of the propagation wavevector (k'_x) to the imaginary part (k''_x):

$$Q_{SPP} = \frac{k'_x}{k''_x} = \frac{\varepsilon_{1,TiN} + \varepsilon_{1,dielectric}}{\varepsilon_{1,TiN} * \varepsilon_{1,dielectric}} * \frac{\varepsilon^2_{1,TiN}}{\varepsilon_{2,TiN}}$$

The higher the imaginary part of dielectric function ε_2, the bigger the electron losses, the lower the Q_{SPP} .
Titanium nitride gives quite good values of quality factors throughout the whole wavelength spectrum (Q_{SPP} ranging from 1 to 10 in the visible, and up to 100 in the NIR); however, among the IV_b group nitrides (TiN, ZrN, HfN) it performs the worst, despite being the most widely studied so far [12]. Sugavaneshwar et al. [25] showed that TiN has better potential applicability for energy conversion purposes like photothermal or photocatalytic applications (where large ε_2 values are needed; it will be discussed deeper in section 1.3.1) rather than light confinement and waveguiding. In fact, as it can be seen from Fig. 1.4, TiN has large negative values of ε_1 comparable to conventional plasmonic materials (i.e. gold), but also larger ε_2 values and hence a lower Q_{SPP}.
As Naik et al. [2] pointed out, TiN has larger carrier relaxation rates than most of noble metals, which additionally increases the losses due to scattering (Ohmic losses).
Schroeder et al. [7] showed that TiN provides better field confinement than gold and silver; however, field propagation length is smaller. The trade-off between propagation length and confinement width is captured by figure of merit M_1^{1D}, defined as the ratio of propagation length to confinement width for 1D SPP waveguides. From Fig. 1.5 it is clear how gold and silver outperform nitrides for waveguiding applications.

On the other hand, despite worse performances than conventional plasmonic materials like noble metals, TiN films represents an alternative with various other advantages: cost-effective, CMOS compatible, chemically and mechanically stable and with easily adjustable optical properties.
Moreover, titanium nitride represents an extremely interesting and promising plasmonic material for applications others than SPP light confinement. This topic will be widely discussed in section 1.3.1.

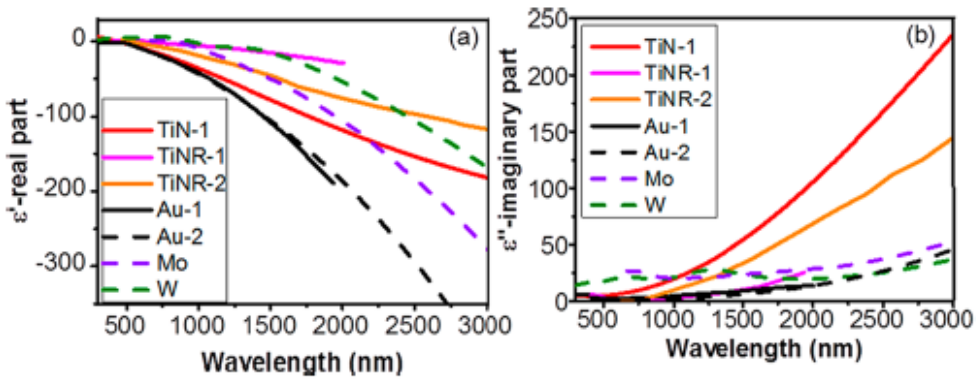

Figure 1.4: Comparison of permittivity data measured via spectroscopic ellipsometry with previous reports on TiN against Au, W, and Mo. (a) Real part; (b) Imaginary part. Permittivity data TiN-R1 and TiN-R2 were deposited with different deposition techniques. Taken from [25].

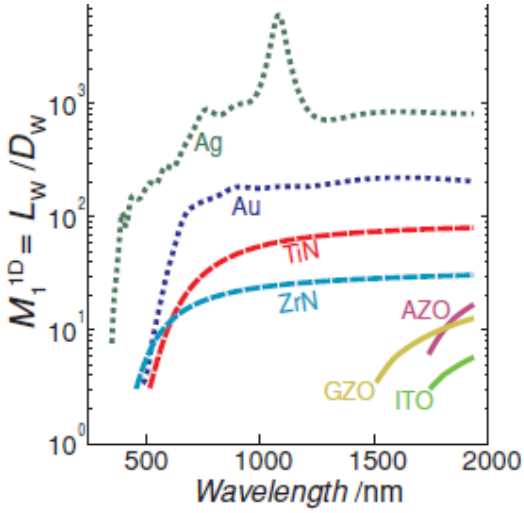

Figure 1.5: The figure of merit M_1^{1D} is defined as the ratio of propagation length (L_w) to confinement width (D_w) for SPPs on dielectric/metal interface. This figure of merit is indicative of the trade off offered by each plasmonic material between confinement and propagation length. Taken from [2]

1.2.2 Deposition techniques and properties tuning (state of art)

A wide variety of fabrication techniques have been used for the growth of TiN films, such as Magnetron Sputtering (MS), Chemical Vapor Deposition (CVD) [26], Cathodic

Vacuum Arc (CVA) [27], Ion Beam Assisted Deposition (IBAD), Atomic Layer Deposition (ALD), High Power Impulse Magnetron Sputtering (HIPIMS) [28], and Pulsed Laser Deposition (PLD).

In the following paragraphs the state of art will be analyzed with particular focus on properties tuning on and main features of TiN films deposited by physical vapor deposition (PVD) techniques, like Magnetron Sputtering and Pulsed Laser Deposition. Only physically deposited TiN films will be considered in pursuance of having indications regarding conditions and deposition mechanisms useful for this thesis work, where PLD will be used.

Magnetron Sputtering is by far the most used deposition method for TiN films, thanks to its capability to form uniform, strongly adhesive, high quality films with high deposition rates and with an excellent control over coating properties by tuning the deposition parameters. The two main drawbacks of this technique are the impossibility to deposit highly porous or nanostructured films and the difficulty to obtain the desired stoichiometry. In fact, two are the main parameters with one can play: power and pressure. However, the range of values where these parameters can be varied is quite limited, since, for example, a too high flux of nitrogen or oxygen may contaminate the target surface (that can get oxidized hence losing its conductivity). Pulsed Laser Deposition technique almost completely overcomes these limitations.

The working principle of PLD is synthetically presented in the following. Inside a vacuum chamber, a pulsed laser beam is focused on the surface of a solid target, which is evaporated. The ablated species form a plasma plume expanding towards the substrate. This process can occur in ultra high vacuum or in the presence of a background gas. In the latter condition the ablated species react with the gas molecules in order to give the desired film composition: it is the so-called *reactive* pulsed laser deposition.
More details about PLD apparatus and process parameters will be given in section 2.1.

Titanium nitride films have been grown by Pulsed Laser Deposition for more than 30 years, and in the last few years the research studies above TiN deposited by PLD are gaining more interest. This is due to some great advantage brought by this technique.
First of all, the target stoichiometry and composition, in principle, can be more easily reproduced in the deposited film. Since titanium nitride is an intrinsically non-stoichiometric compound, hence with optical and electrical properties depending significantly on the N/Ti ratio, being able to tune film composition by varying deposition conditions is crucially important.
Second, the morphology and structure of the deposit can be tuned by playing with some parameters such as deposition pressure and laser energy density. The possibility of obtaining nanoporous films and nanostructured films build up by nanoparticles assemblies (like *nanoforests*,for example) brings up new exciting horizons in titanium nitride study research, especially in the field of plasmonics (this topic will be treated in section 1.3.2).
Finally, PLD shows a great versatility: many types of materials can be deposited in a wide variety of atmospheres and over a broad range of pressures.

The main drawback of the technique lay in its limitations in producing large area uniform thin films, due to inhomogeneous flux and angular energy distributions within the ablation plume. Another disadvantage is the ejection of macroscopic particulate from the target during the ablation process: these droplets mainly affect film electrical properties.

Oxidation issue

When studying titanium nitride, an extremely crucial issue lays in its difficulty to be deposited as a purely stoichiometric compound, due to titanium higher reactivity with oxygen rather than with nitrogen. For this reason, it is essential to first analyze the structural, compositional, optical and electrical properties variation as a function of the oxidation extent. Secondly, the parameters which have been found to influence oxidation (like post-annealing temperature and atmosphere, substrate temperature and film porosity) have to be considered.

Trenczek-Zajac et al. [29] investigated the evolution of structural and electrical properties of *in situ* oxygen-doped TiN films. The TiON films were obtained by a reactive magnetron sputtering process where the oxygen flow rate η_{O2} was gradually increased from 0 to 1.65 sccm. Oxygen is much more reactive than nitrogen, and its excess led to supersaturation effect that put constraints on TiN crystallization. Similar behavior has been reported [30] and attributed to titanium oxynitride formation.

At the highest flow rates (η_{O2} = 1.65 sccm) the onset of precipitation of very weakly crystallized anatase titanium dioxide in the amorphous background was noticed: the excess of oxygen could not be accommodated anymore in TiN_xO_y hence the precipitation of TiO_2 started, as confirmed by X-ray Photoelectron Spectroscopy (XPS) analysis.

Raman spectra (Fig. 1.6) clearly changed with increasing η_{O2} (see section 2.3. for details about Raman spectroscopy of TiN). At first (0 sccm < η_{O2} < 0.46 sccm), an increase in the relative intensity of the acoustic bands (associated to vibrations of Ti^{4+} ions due to nitrogen vacancies) over the optical band (associated to vibrations of N^{3-} ions due to titanium vacancies) and a shift towards higher frequencies of the transversal and longitudinal acoustic modes indicated a deviation from TiN stoichiometry. In fact, according to many literature papers [31, 32], a higher $I_{acoustic}/I_{optical}$ ratio is related to a higher number of nitrogen vacancies (i.e. lower N^{3+} ions vibrating) and therefore to a less stoichiometric titanium nitride.

When the oxygen flow rate was further increased (0.5 sccm < η_{O2} < 1.32 sccm), the number of nitrogen vacancies (which are easily filled by oxygen atoms) raised, thus leading to a significant broadening of the Raman bands due to the progressive amorphisation of the film. Over this range of oxygen flow rates there was TiN_xO_y with a N/Ti ratio (estimated from XPS analysis) that went from 0.8 to 0.35.

Finally, at η_{O2} = 1.65 sccm the shape of the Raman spectrum changed: new broad contributions begun to appear around 150 cm^{-1}, 390 cm^{-1} and 550-600 cm^{-1}, indicating the first appearance of titanium dioxide largely in amorphous phase. Regarding the films

optical properties as a function of η_{O2} (Fig. 1.7a), at low oxygen flow rates (0 sccm < η_{O2} < 0.46 sccm) the reflectance spectrum stayed the same as the one of pure TiN.
Nevertheless, with an increasing oxygen doping (η_{O2} up to 1.32 sccm) a pronounced red-shift in the position of the reflectance minimum and a less steep reflectance edge at long wavelengths were observed.
At η_{O2} = 1.65 sccm the reflectance dip was lost, due to amorphous titanium dioxide formation.
The most significant differences between oxygen-doped and pure TiN manifested themselves in the optical transmission (Fig. 1.7b). Stoichiometric TiN was almost opaque and its transmission coefficient (T ~ 0.3-0.4 %) did not show any dependence on wavelength. However, even the smallest amount of oxygen incorporated in TiN affected the transmission spectrum in such a way that a maximum in T(λ) appeared. This maximum rose in value and red-shifted upon increasing oxygen flow rate.
The reasons for this particular behavior of T(λ) in oxygen-doped TiN films were found to be in two different mechanisms of light absorption: free-electron absorption, which was responsible for the decrease in transmittance at λ > 500 nm; fundamental interband absorption (typical of semiconductors such as TiO_2), which gave a substantial decrease in transmittance for λ < 500 nm. These two mechanisms, normally well-separated, took place almost in the same spectral range, probably because of the oxynitrides formation.
Eventually, at η_{O2} = 1.65 sccm the transmittance maximum was lost, due to amorphous titanium dioxide formation.
Radecka et al. [33] studied the variation of structural and electrical properties of TiN films, deposited by DC-pulsed reactive magnetron sputtering in $Ar:N_{2:}O_2$ atmosphere, as a function of oxygen flow rates. Based on impendance spectroscopy analysis, the transition from metallic to semiconducting-type electrical behavior was proposed to be over the range of η_{O2} = 0.46-0.66 sccm. In this range, TiN_xO_y formation and a general films amorphisation due to oxygen incorporation had started. At η_{O2} > 1.5 sccm the formation of precipitated amorphous TiO_2 phases led to an insulating-type electrical behavior.

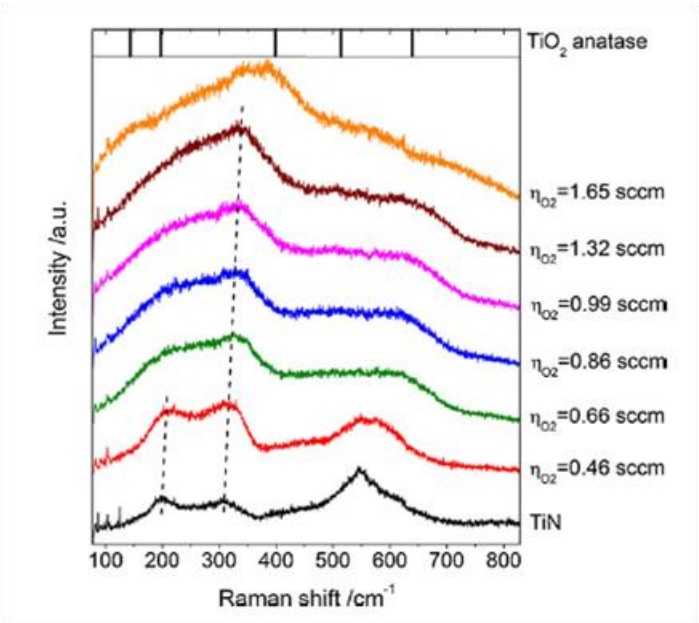

Figure 1.6: Raman spectra of TiN and oxygen-doped Ti(ON) thin films deposited by reactive magnetron sputtering onto amorphous silica at different flow rates η_{O2}; peak positions for TiO_2 anatase are indicated at the top. Taken from [29].

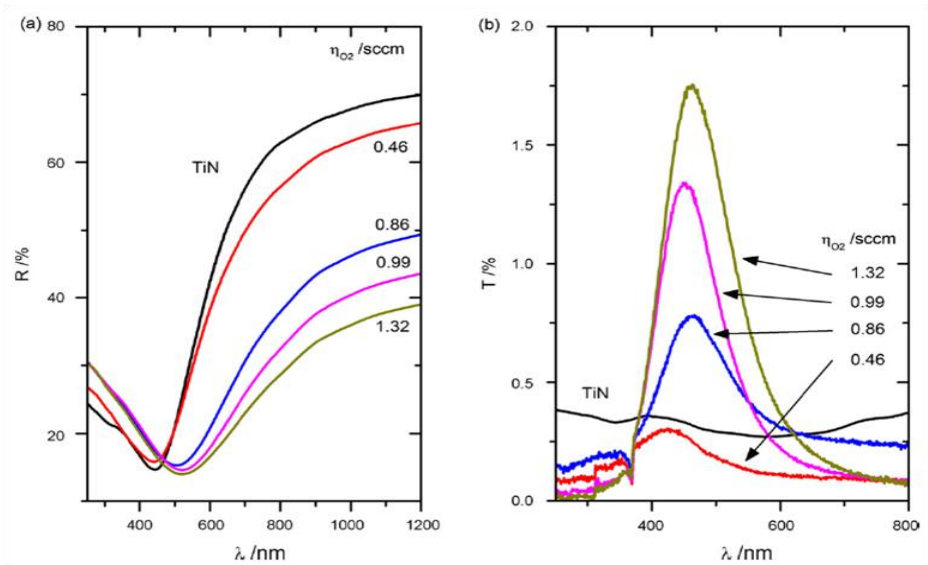

Figure 1.7: Optical coefficient of (a) reflectance R(λ) and (b) transmittance T(λ) as a function of wavelength for TiN and oxygen doped Ti(ON) thin films deposited onto amorphous silica at different oxygen flow rates. Taken from [29].

When the deposition atmosphere is highly oxidizing the characteristic Raman peaks of either Rutile, Anatase or a mixture of the two may start to be visible. For example, by analyzing Raman spectra of reactively magnetron sputtered titanium oxynitride (TiON) in

$Ar:N_2:O_2$ (2:1:1) atmosphere, Padmavathy et al. [34] found (besides the typical modes of TiN bonds) three peaks at 148 cm^{-1}, 518 cm^{-1}, and 398 cm^{-1}, which indicated the presence of crystalline Rutile and Anatase TiO_2 structures coexisting in the film. Also De Sousa et al. [35] pointed out that TiN films deposited with an oxygen flow rate of 3 sccm easily show Raman spectra typical of either Rutile, Anatase or a mixture of the two, depending on thermodynamic conditions induced by deposition parameters.

It has to be underlined how a very thin film of native oxide layer always forms on titanium nitride surface upon air exposure, as observed by many research studies. For example, Ernsberger et al. [36] observed the formation of a very thin (~ 1.1 nm) oxide layer on top of TiN_x coatings after one week of exposure at room temperature and 38% relative humidity. Similarly, Milosev et al. [37] noticed the formation of some few nanometers thick oxynitride layers on top of TiN coatings upon air exposure for 10 days.

Between the most important parameters affecting titanium nitride films' oxidation, porosity plays a primary role: a more open structure leads to a higher surface to volume ratio and therefore to an higher oxidation extent.
On this purpose, Achour at al. [38] magnetron sputtered a titanium target in a $Ar:N_2$ atmosphere at different power values, in order to obtain TiN films with different composition and porosity. It was found that above a certain sputtering power (~ 80 W) the films did not differ much neither in composition nor in porosity. In fact, the three films deposited at power greater than 80 W (which are called T_1,T_2,T_3 in Fig. 1.8) presented the same, typical Raman Spectrum of TiN, and revealed from SEM surface images the same porosity. On the other hand, the film deposited at power P = 80 W (which is called T_4 in Fig. 1.8) showed two Raman peaks at 153.17 cm^{-1} and 518.5 cm^{-1} which have been attributed to the vibration modes of mixed rutile-anatase TiO_2 phase, and presented a higher surface porosity from SEM images. This indicated that the film deposited at lower sputtering power (T_4) had incorporated a higher amount of oxygen because of their more open surface structure with respect to the other, more compact films.

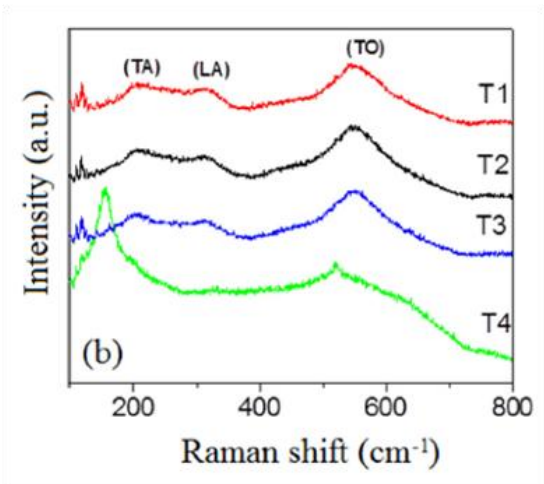

Figure 1.8: Raman spectra of TiN films deposited at different sputtering power: T_1 (120 W); T_2 (150 W); T_3 (200 W); T_4 (80 W). Taken from [38].

These results were confirmed by Yin et al. [39], who deposited TiN films by DC magnetron sputtering at 2.1 Pa pressure of 40% nitrogen in argon. Under this pressure, their samples exhibited higher bulk oxygen content (atomic ratio of ~ 26) due to a low film density.
When porosity further increases (i.e. nanostructured thin films) the oxidation issue gets even more critical: this will be discussed deeper in section 1.3.2.

Post-deposition annealings

Also post-deposition annealings strongly affect many TiN films' features, including its oxidation behavior.
Achour et al. [40] reactively sputtered TiN films and afterwards annealed them at T = 400 °C and 550°C in vacuum (P = $3 \cdot 10^{-2}$ Pa) for 1 hr. From SEM surface images of the as-deposited sample a pyramidal grains morphology was clearly seeable, while a dense columnar structure was visible from the cross section images. No apparent changes in morphology were detected after the annealing. However, Raman spectra (see Fig. 1.9) showed a clear change in film composition: the peak around 550 cm^{-1} associated to nitrogen ions vibrations decreased, probably because of nitrogen that, diffusing from the subsurface to the film surface, was substituted by the residual oxygen present in the chamber. Tarniowy et al. [41] performed thermal treatments in vacuum (P = $1 \cdot 10^{-3}$ Pa), with temperature rising up to 477°C, on amorphous and crystalline TiN films deposited by reactive magnetron sputtering in $Ar:N_2$ (4:1) atmosphere.

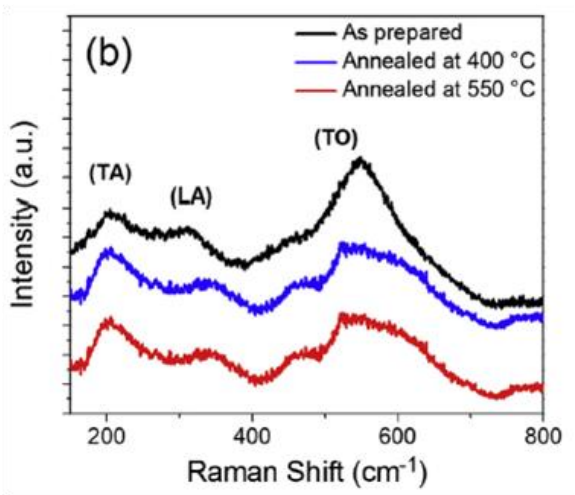

Figure 1.9: Raman spectra of TiN films before and after vacuum annealing. Taken from [40].

As observed from Fig. 1.10, 1.11, the coefficient of transmission of crystalline films was found to be equal to zero, while its reflectance was high (~60-80%) until the plasma reflection edge (in the wavelengths range λ = 420-500 nm). On the other hand, the transmittance of amorphous films resembled the spectrum of a semiconductor containing a very high concentration of defects, with a T(λ) maximum around λ = 480-600 nm, while their reflection coefficient exhibited a red-shifted minimum and a less steep plasma edge.
For already crystalline films the vacuum annealing led to a slightly higher oxidation of the material, and in general did not bring any improvement in material's properties. It was for amorphous films that the annealing represented a way to improve electrical and optical properties. In Fig. 1.12, 1.13, amorphous films annealed at temperature T_{anneal} = 127°C showed a slight drop of transmission and increase of reflection, due to the development of a crystalline phase; on the other side, when the annealing temperature was risen up to T_{anneal} = 477°C a considerable increase of transmission and some oscillations of reflectance coefficient were caused by excessive oxidation of the amorphous phase during the heating.
In Kavitha et al. [42] study research, a 100°C input thermal energy was sufficient to induce in previously magnetron sputtered films some crystallinity, which was further improved at T_{anneal} = 300°C.
Correspondingly, Xi et al. [43] found that after vacuum annealing for 1 hr at 300°C the films structure was transformed from irregular faceted to faceted in the (111) preferred orientation.

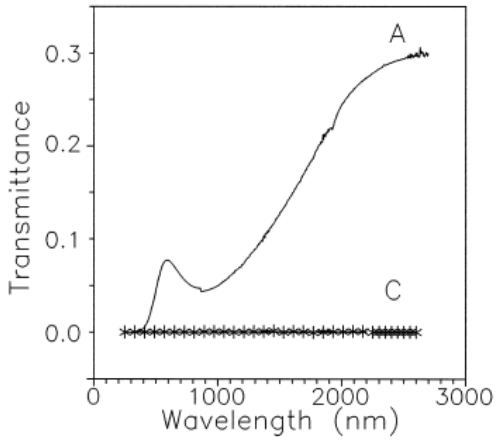

Figure 1.10: Spectral dependence of the transmission coefficient of TiN thin films (film thickness = 800 nm): (A) amorphous; (C) crystalline. Taken from [41].

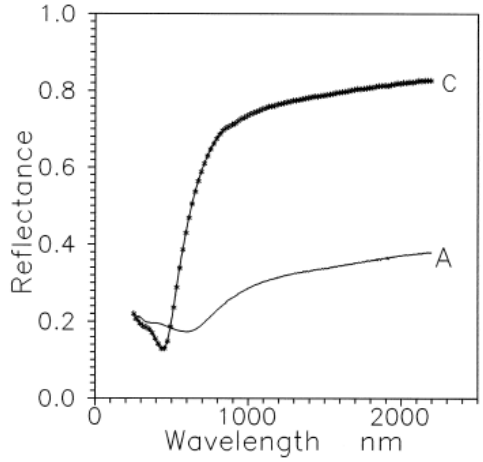

Figure 1.11: Spectral dependence of the reflection coefficient of TiN thin films (film thickness = 800 nm): (A) amorphous; (C) crystalline. Taken from [41].

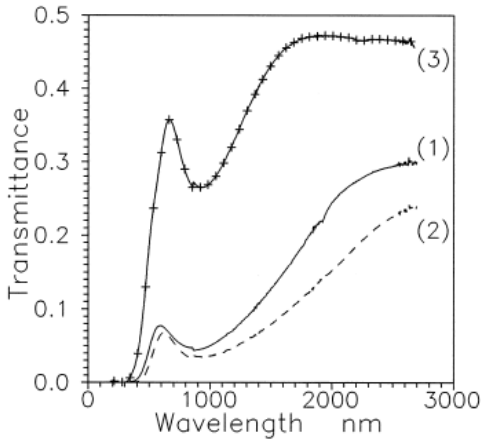

Figure 1.12: Spectral dependence of the transmission coefficient of TiN thin films (film thickness = 800 nm): (1) as-sputtered; (2) after annealing at 127°C; (3) after annealing at 477°C. Taken from [41].

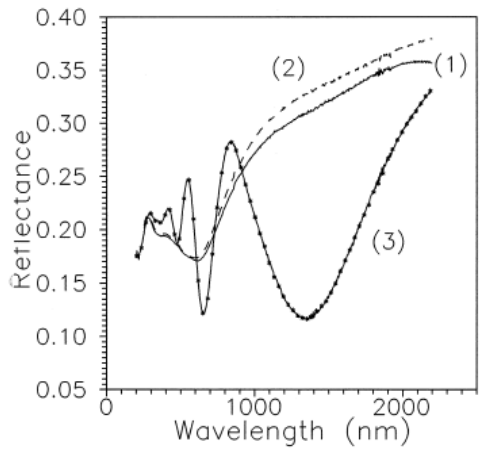

Figure 1.13: Spectral dependence of the reflection coefficient of TiN thin films (film thickness = 800 nm): (1) as-sputtered; (2) after annealing at 127°C; (3) after annealing at 477°C. Taken from [41].

In conclusion: first of all, a good compromise between good crystallization and little oxidation extent of titanium nitride has to be found when selecting the temperature for thermal treatment; then, the more amorphous is the film, the more useful can be the thermal annealing, but also the more challenging can be to find the optimum temperature.

In N_2:H_2 annealing, both oxygen and nitrogen partial pressures in the gases would influence the oxidation chemistry. In fact, the oxidation reaction of TiN can be formulated as:

$$mTiN + \frac{n}{2}O_2 = Ti_mO_n + \frac{m}{2}N_2 \quad \left(where\ \frac{m}{n} = \frac{1}{2}\right)$$

The standard free energy change for the reaction ΔG^0 can be expressed as:

$$\Delta G^0 = -RTln\left(\frac{pN_2^{\frac{m}{2}}}{pO_2^{\frac{n}{2}}}\right)$$

Where, at equilibrium, $(p_{N_2}^{m/2}/p_{O_2}^{n/2})$ as a function of temperature represents a fixed gas ratio at which TiN is in thermodynamic equilibrium with Ti_mO_n.
Therefore, a higher annealing temperature may favor crystallization but at the same time implies a higher $(p_{N_2}^{m/2}/p_{O_2}^{n/2})$ ratio required in order to have thermodynamic equilibrium between TiN and its oxide phases. If the nitrogen relative partial pressure is not high enough, the formation of titanium oxides is thermodynamically favored. In reality, the situation is more complex due to the formation of ternary compounds, i.e. titanium oxynitrides [44].
Lu et al. [45] annealed few TiN films at T_{anneal} = 500-700°C for 2 hr in N_2:H_2 (9:1) mixture. From XPS measurements, the relative intensities of TiN and of titanium oxynitride decreased with increasing anneal temperature, while that of TiO_2 increased. This could have been due to the transformation of amorphous TiO_2 into fully crystalline TiO_2. They reported that, after an anneal at T_{anneal} = 500°C, a theoretical value $(p_{N_2}^{m/2}/p_{O_2}^{n/2})$ > 10^{39} (with: m =1; n = 2) would have been needed to obtain a purely TiN film, which was indeed practically impossible. Also Wang et al. [46] reported that TiN films annealed in N_2 atmosphere at T_{anneal} > 500°C were always subjected to oxidation reactions, which gave rise to oxide phases and therefore to color changes from golden yellow to light blue/purple. They also observed that the thinner was the film (for the same deposition conditions), the lower was the critical T_{anneal} for the oxidation reactions to seriously enhance the film's electrical resistivity. However, together with oxide phases formation, after annealing the films crystallinity considerably increased.
Huang et al. [47] deposited TiN thin films by unbalanced magnetron sputtering and implemented post-deposition heat treatment at 500°C and 700°C for 1 hr in N_2:H_2 (9:1) atmosphere. From Auger Electron Spectroscopy analysis, after annealing the concentration profile of oxygen reached even higher values than as-deposited samples until a depth of

~24 nm, and reached the same *plateau* value deeper inside. But, on the other side, TiN crystallization along <111> direction improved at T_{anneal} = 500°C and even further at T_{anneal} = 700°C.

Substrate heating during deposition

Another important deposition parameter that influences thin TiN films main properties is the substrate temperature.
Subramanian et al. [48] deposited on mild steel substrates heated at T_{sub} = 400°C some TiN thin films by reactive DC magnetron sputtering and studied their structural and optical properties. X-ray diffraction (XRD) revealed that the films had a lattice parameter *a* = 0.424 nm. This is the value of lattice constant for nearly stoichiometric TiN; therefore only a little amount of oxidation was present, mainly at the surface. This result was obtained thanks to the higher ad-atoms mobility given by substrate heating during deposition. These films showed a maximum reflectance value of 60% at λ = 850 nm and a local reflectance minimum at λ = 480 nm (Fig. 1.14), which is typical of nearly stoichiometric TiN films.

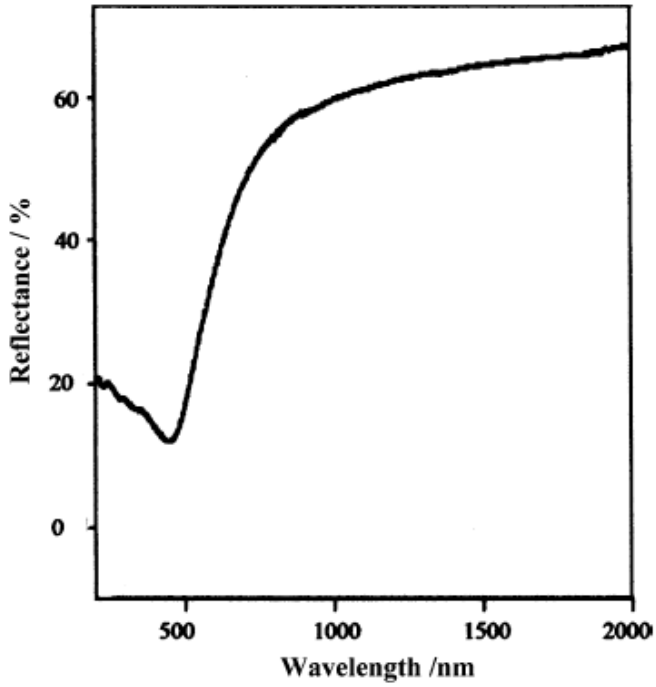

Figure 1.14: Reflectance of TiN film deposited while heating the substrate at 400°C. Taken from [48].

In conclusion, heating the substrate during deposition seems to generally give higher quality stoichiometric films with better optical properties (in terms of high reflectance and bright yellow color appearance) with respect to post-deposition annealing. Presumably, the high temperatures favoring ad-atoms diffusion during deposition are more effective in obtaining stoichiometric TiN rather than thermal treatments performed once the structure (with some oxygen incorporated inside and some adsorbed on the surface) is already

formed,. In fact, as it can be seen in Fig. 1.15, the Raman optical band of TiN films (which is associated to nitrogen atoms vibrations) increases as the substrate temperature during deposition increases. Therefore, nitrogen rich and oxygen poor thin films can be obtained by heating the substrate, while this was not always the case when post-annealings were performed (see Fig. 1.9). However, by properly selecting the post-deposition thermal treatment temperature (not too low nor too high, depending on the case) it is possible to efficiently cope with oxidation, to increase the crystallization and, consequently, to improve the electrical and optical properties of the film.

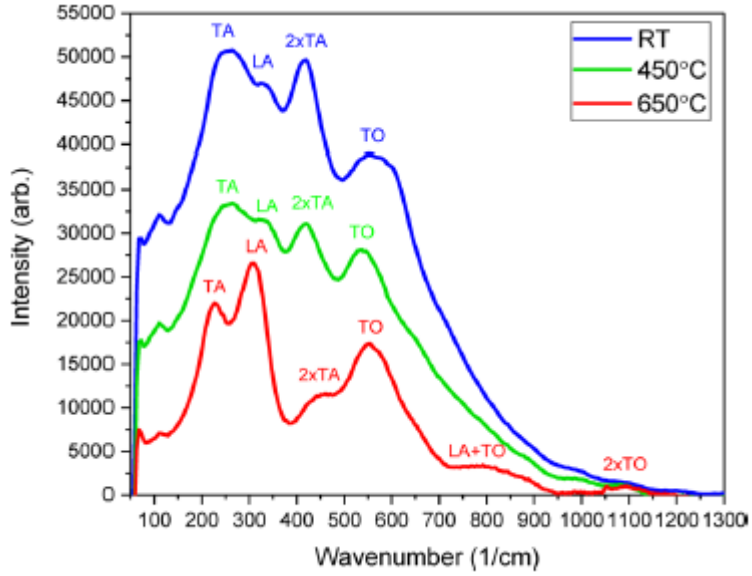

Figure 1.15: Raman spectra of samples grown at different temperatures by PLD. Taken from [49].

Pulsed Laser Deposition

In the following research papers it is showed how the PLD deposition conditions can be used and tuned to control composition, electrical and optical properties, as well as plasmonic behavior of TiN thin films.

Mihailescu et al. [50] deposited TiN films by reactive laser ablation of a titanium target at room temperature in a background pressure of nitrogen and with a fluence (laser energy density) of ~ 5 J/cm^2. In particular, they used a nitrogen pressure (p_0) ranging from $6 \cdot 10^{-2}$ Pa to 1000 Pa, obtaining pure *fcc* TiN for 0.7 Pa < p_0 < 7 Pa. At higher pressures, oxygen impurities concentration present in the reactive N_2 gas rose and got significantly high. On the other side, at lower pressures, the lower presence of nitrogen atoms able to react with ablated titanium particles led to residual oxygen in the chamber which oxidized the film. It was also underlined how some oxygen impurities could have been desorbed from the substrate and from the chamber walls.

Similarly, Gu et al. [51] performed reactive PLD of a Ti target in a nitrogen atmosphere at room temperature. They found that the optimum values of the product between N_2 pressure and target-substrate distance were within $3 \cdot 10^{-2}$ and $4.5 \cdot 10^{-2}$ Pa·cm, using a laser fluence of 6.7 J/cm^2.

Krishnan et al. [52] used a reactive PLD where the process parameters were optimized using Secondary Ion Mass Spectroscopy (SIMS). They made multilayers of TiN_x by varying one key processing parameter (deposition pressure and fluence), keeping all other parameters constant. In order to facilitate a clear distinction on the composition brought about by change in the key processing parameter, a niobium interlayer was deposited between successive TiN_x layers. Resultant multilayer films were characterized for chemical composition using SIMS depth profiling mode. A maximum N/Ti ratio was achieved at a N_2 pressure of 3 Pa. Moreover, increasing the laser pulse energy from 100 mJ to 500 mJ led to an higher N/Ti ratio and a lower oxygen impurities level (besides an higher film thickness). A possible explanation was given: an higher value of energy per pulse dissociates more N_2 gas molecules, resulting in a higher availability of N^+ and N^- radicals for TiN synthesis.

Craciun et al. [53], ablated some TiN targets with laser fluence 8 J/cm^2 under a high purity atmosphere of N_2 10 Pa. The deposition chamber had been previously evacuated to ultra high vacuum (P = 10^{-6} Pa) in order to avoid as much as possible incorporation of residual oxygen atoms, and the substrate temperature was risen up to 500°C. The lattice parameter estimated from XRD measurements was a = 0.4252 nm, not so much bigger than a value for purely stoichiometric TiN (a = 0.4242 nm). Auger Electron Spectroscopy (AES) survey spectra recorded from the as-deposited surface and after removal of more than 10 nm of surface material by argon sputtering, indicated oxygen concentrations below 3 at% within the deposited films.

Guo et al. [54] studied the effect of substrate heating temperature during pulsed laser ablation of TiN target in ultra high vacuum condition (P = $6 \cdot 10^{-5}$ Pa). An higher substrate temperature (which was set at 500°C) enhanced the ad-atoms mobility through temperature dependent thermal vibrations, and led to higher crystallization and more pyramidal surface morphology.

Furthermore, Sugavaneshwar et al. [25] fabricated titanium nitride films by pulsed laser ablation of a TiN target at room temperature on SiO_2/Si and organic flexible substrates. The deposition was performed in vacuum (P = $6.7 \cdot 10^{-4}$ Pa) and the laser fluence was set at 6 J/cm^2. Four films were made at different deposition rates by adjusting the laser frequency. Films deposited at higher deposition rates showed a smaller grain size from AFM images: this resulted in heavier scattering (higher resistivity values), higher losses (higher ε_2 values, see Fig. 1.16) and less stoichiometric N/Ti ratio, but at the same time higher metallicity (higher ε_1, see Fig. 1.16), larger values of charge carrier densities (n ~ 7-8 $\cdot$ 10^{22} cm^{-3}) and higher mobility values (because of less defective films hence bigger relaxation time).

Then, they also evaluated the figure of merit (FoM = - ε_1 / ε_2) in order to assess their SPP waveguiding performance. These TiN films showed a greater plasmonic performance than those obtained with sputtering techniques under similar low-temperature deposition

conditions. However, conventional plasmonic materials like gold still largely overcame these TiN's FoM values by one order of magnitude.

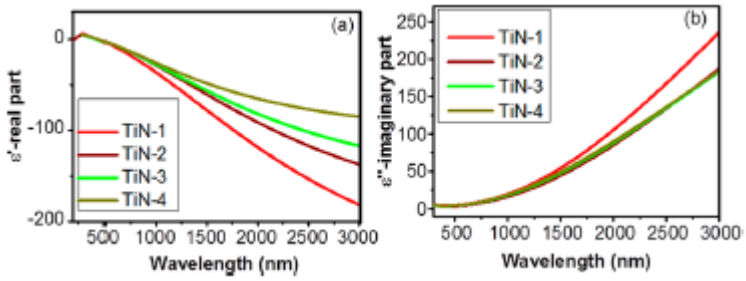

Figure 1.16: Complex permittivities of the TiN films deposited at different deposition rates (TiN-1, TiN-2, TiN-3 and TiN-4 deposited at 0.1, 0.07, 0.05, and 0.03 Å/s, respectively); (a) real part; (b) imaginary part. Taken from [25].

Summarizing, we have seen that PLD of TiN can be performed and that high quality thin films can be obtained. To grow epitaxial and compact thin TiN films, the optimum values of laser fluence and N_2 pressure seem to be 5-7 J/cm^2 and 3-7 Pa, respectively. It is clear that a heated substrate facilitates the crystallization process and limits oxygen incorporation during film growth.

It should be specified that with pulsed laser deposition it is possible to deposit not only compact films (as the ones reported in the papers above), but nanostructured thin films as well. Nanostructured films are constituted by nanoparticles assemblies; therefore, with respect to compact films, they have significantly different electrical, optical and plasmonic properties, as well as different synthesis issues to cope with. For this reason, these so-called hierarchical (or nanoporous) films will be treated in the section about TiN nanoparticles (1.3.2).

A thorough study of titanium nitride thin films deposited by PLD was performed by Garattoni in this laboratory.
In the following the main achievements of Garattoni's research [9] are schematically presented:

1) First of all, the fabrication of continuous and compact thin films by PLD on glass, Si and SiO_2 substrates at room temperature was successfully accomplished. In particular, the issue related to compact film adhesion on glass was overcome by "cleaning" the substrate with a plasma of Ar ions.

2) Second, the effect of some deposition parameters, in particular pressure and fluence, was correlated with the morphology and composition of the obtained samples.

3) Finally, the effects of thermal treatments on the structure, electrical resistivity and optical properties of the samples were investigated. The annealing was performed either in vacuum or with N_2:H_2 (95-5 %) supply at controlled overpressure of 1050 mbar. The process time and temperature were kept constant: T_{anneal} = 550°C was selected amongst the most commonly used annealing temperatures in literature; annealing time was chosen to be of 60 min. The main effects of thermal annealing were:
   - From XRD patterns, both the annealings induced an improved crystallization of the films, mostly along <111> direction.
   - From Raman spectra some general trends can be identified (see Fig. 1.17). First of all, because of the exposure to N_2 during heat treatment, the acoustic peak below 400 cm^{-1} blue-shifted; this effect was much less evident for vacuum-annealed samples. Additionally, the intensity of the optical band around 600 cm^{-1} generally increased after thermal treatment in N_2/H_2 atmosphere, thus appearing strongly related to the film exposure to nitrogen.

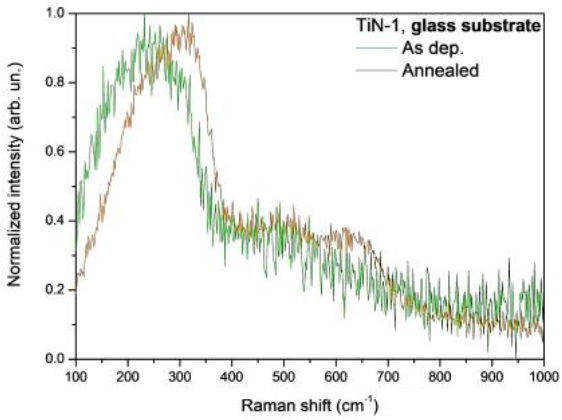

Figure 1.17: Raman spectra of TiN thin film deposited on glass (f = 3.5 J/cm^2; P = 1 Pa N_2) before and after annealing in N_2/H_2. Taken from [9].

- From electrical resistivity measurements, the resistivity values of the films (~ $2.5 \cdot 10^{-4}$ Ωcm) were one order of magnitude higher than the best results found in literature. Moreover, these resistivity values remained unexpectedly unchanged after thermal treatments. Finally, the results of Hall measurements were not presented since, for all the samples, the figure of merit indicated that

the obtained data were unreliable. Therefore, no data on the carrier density have been reported.

- From UV-Vis spectrophotometer measurements, the most evident effect of thermal treatment was the red-shift of film reflectivity and the lower reflectivity minimum, whose intensity dropped almost to zero when annealing was performed in N_2/H_2 (see Fig. 1.18). In fact, by increasing the nitrogen content after annealing, the number of the free electrons in the films was reduced. Therefore, fewer electrons interacted with the incident radiation, reducing the reflected light. On the other hand, the explanation of the red-shift resulted more complicated; the hypothesis made was that, by increasing the nitrogen concentration, the real permittivity ε_1 (which "controls" intraband absorption) became negative at longer wavelengths. Not surprisingly, the lowest measured λ_{min} (wavelength value where the reflectance dip occurs) corresponded to the as-deposited films grown in vacuum (and were ~ 330 nm), while the highest were related to the films deposited and annealed in N_2/H_2 (and were ~ 470 nm). In conclusion, it was underlined how it was still essential to understand the influence of oxidation on the TiN films optical properties and to correlate these properties to the structure, composition and density of carriers. On this purpose, most of these open issues have been investigated in this thesis

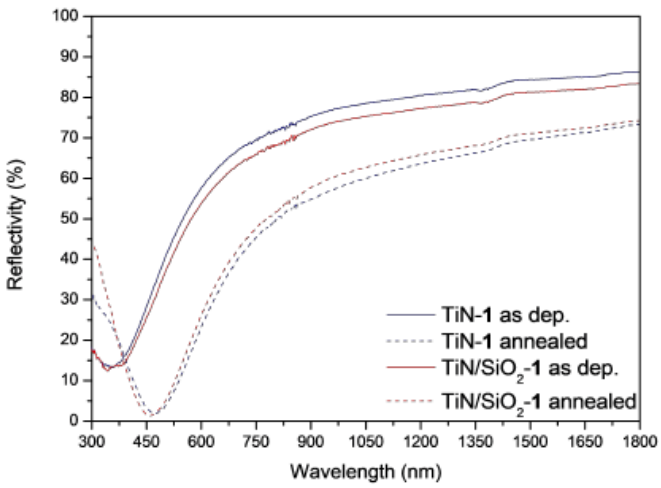

Figure 1.18: Reflectivity of TiN samples deposited on SiO_2 and on glass at 1 Pa N_2/H_2 and annealed in the same atmosphere. Taken from [9].

1.3 TiN nanoparticles

1.3.1 Plasmonic properties and applications

Plasmonics has attracted a great attention over the last few decades due to the enticing physical mechanism arising from the interaction of light with resonant structures at the nanometer scale. The unique characteristic of plasmonic materials consists in their ability to sustain resonant oscillations of free electrons as a response to electromagnetic waves, known as surface plasmons (SPs). These coupled oscillations can either propagate along an interface (and so they are called surface plasmon polaritons SPPs, as reported in section 1.2.1), or they can exist as localized surface plasmon resonances (LSPR). The latter collective fluctuations of charge density can be sustained by metallic nanoparticles (NPs).
In order to analyze the localized surface resonance, we could consider, in a first approximation, an isolated nanoparticle immersed in an electromagnetic field whose wavelength is much longer than the diameter of the particle (quasi-static approximation). In this case, it is possible to consider that the applied electromagnetic is uniform at each instant and at any point of the object volume (no delay effect). In such quasi-static approximation and if the temporal variation of the applied field is set aside, the problem returns to that of a sphere subjected to a uniform field E_0. The application of E_0 induces a polarization of the sphere and the appearance of a charge surface distribution. In this way, the particle is equivalent to an ideal dipole, whose dipole moment directly depends on the polarizability of the sphere α:

$$\alpha = \frac{\varepsilon_1 - \varepsilon_m}{\varepsilon_1 + 2\varepsilon_m} V$$

Where V is the volume of the sphere, ε_m is the dielectric constant of the medium and ε_1 is the real part of the metallic NP dielectric function. The theory of scattering and absorption of radiation by a small sphere predicts a resonant field enhancement due to a resonance of the polarizability α, which occurs when $\varepsilon_1 = -2\varepsilon_m$. Under these circumstances, the nanoparticle acts as an electric dipole, resonantly absorbing and scattering electromagnetic fields..
By expressing the dielectric constants as a function of the plasma frequency ω_p (in the Drude model, hence neglecting electron-electron interactions and considering the charge density as a free electron gas), the *localized surface plasmon resonance frequency* is obtained:

$$\omega_{LSPR} = \frac{\omega_p}{\sqrt{1 + 2\varepsilon_1}}$$

Consequently, both the scattering and absorption spectra of the induced oscillating electric dipole are greatly enhanced at the resonant wavelength, compared to dielectric

nanoparticles of similar size. In other words, the extinction spectrum is maximized in the resonance condition:

$$\sigma_{ext} = \sigma_{abs} + \sigma_{scatt}$$

where σ_{abs} and σ_{scatt} are the absorption and scattering cross sections, respectively.
This theory of the *dipole* particle plasmon resonance is strictly valid only for vanishingly small particles; however, in practice this theory provides a reasonably good approximation for spherical particles with dimensions below 100 nm illuminated with visible or NIR radiation [1].
By writing the absorption and scattering cross sections as a function of polarizability α, where ε_1 and ε_m dependencies on the wavelength λ have been explicated, the cross sections as a function of λ can be obtained:

$$\sigma_{abs} \sim \frac{1}{\lambda}$$
$$\sigma_{scatt} \sim \frac{1}{\lambda^4}$$

For the same nanoparticle, the ratio of the scattering and absorption cross section is proportional to the volume V, so:

$$\frac{\sigma_{scatt}}{\sigma_{abs}} \propto \frac{V}{\lambda^3} \propto \left(\frac{R}{\lambda}\right)^3$$

Thus, in the quasi-static approximation ($R \ll \lambda$), extinction is largely dominated by absorption.
For particles of larger dimensions instead, the quasi static approximation is not justified due to the significant phase-changes of the driving field over the particle volume. The approach know as Mie theory gives an exact general calculation of the optical response of a spherical particle of any diameter. Mie developed a theory of the interaction of an electromagnetic wave with a homogeneous spherical metal nanoparticle based on a multipolar development of the electromagnetic field. The important final result is that the absorption and scattering cross sections are simply expressed as series were the coefficients are functions of the particle size [55].

The major source of losses in metal nanoparticles are electrons collisions; for this reason, one of the most important parameters is the electron mean free path (MFP) l, that can be written (in a first approximation) as: $l = \tau_D V_f$, where τ_D is the relaxation time of conduction electrons and V_f is the Fermi velocity (the velocity of electrons located on the Fermi surface). In order to understand why changing certain process conditions can affect

the LSPR, it is necessary to correlate the observed optical properties with the material. From the following relationships:

$$\omega_{ps} = \sqrt{\frac{Ne^2}{\varepsilon_0 m^*}}$$

$$\gamma_{NP} = \gamma_{bulk} + \frac{AV_F}{D}$$

(where N is the density of conduction electrons, ε_0 the permittivity of free space, m^* the effective mass of the electrons, $\gamma = \tau_D^{-1}$ the damping parameter of the nanoparticles, V_F the Fermi velocity and D the diameter of NPs), it is clear how the particle morphology and surface chemistry play a crucial role in determining its optical properties.

From conventional to alternative plasmonic materials for LSPR applications

The strong plasmonic response from noble metals in the visible region of the electromagnetic spectrum has been the main reason for the frequent use of these materials. In his work, Michael Faraday reported the color changes he observed from metal nanoparticles like gold and silver dispersed in a dielectric body [56]. Another reason for the use of metal nanoparticles is certainly the well-developed colloidal assembly methods, which have been studied extensively over the years [57]. Due to these two important advantages, the material selection in the field of plasmonics naturally resulted in the frequent use of Au and Ag in research studies. Moreover, noble metals have been commonly used for plasmonic devices because of their small ohmic losses (or high DC conductivity) and their proven biocompatibility and chemical stability. However, problems from a wide range of disciplines awaiting a solution from the field of plasmonics cannot be solved with a limited pool of materials. In order to provide solutions to problems with different requirements such as operating at specific windows of the electromagnetic spectrum and different ambient conditions, alternative materials are needed.

Plasmonic resonances of noble metals NPs naturally occur at the shorter wavelengths region of the visible window. Although this may be a great advantage in many cases [56], adapting these materials to applications that require operation at longer wavelengths has been a problem. For example, a big issue has risen in the integration of Au nanostructures for biomedical applications, which need resonances in the near infrared window of the electromagnetic spectrum, due to the lower attenuation of light through biological tissues at these wavelengths [58]. Hirsch et al. [59] tried to solve this problem by modifying the geometry of Au nanoparticles to core-shells (also called nanoshells), thereby red-shifting the resonance peak to the near-IR window. Engineered shapes of metal NPs for efficient operation in the biological transparency window have been extended to various different geometries like nanorods, dimers and multishells [60, 61]. Nevertheless, such big structures with shapes different than spheres are much tougher to be processed by the

human organism. For this reason, plasmonic NPs with smaller sizes and simpler shapes would be more desirable for biomedical applications.
Moreover, gold's poor thermal stability (a problem exacerbated by the reduction in melting point observed in nanostructures) limits its utilization for heating applications at elevated temperature. Although it has been shown that thermal stability of these nanostructures can be increased by use of a relatively thick encapsulating silica shells [62], such geometric modifications would highly affect the optical properties, which is not desired for many applications.
Additionally, an important technological challenge associated with noble metals is that they are not compatible with standard silicon manufacturing processes. This precludes plasmonic devices from leveraging on standard nanofabrication technologies, and diminishes the possibility of integrating such devices with nanoelectronic components. This compatibility issue arises from the fact that noble metals can easily diffuse into silicon to form deep traps, which severely affect the performance of the electronic devices.
Eventually, a major drawback of noble metals is that their optical properties cannot be tuned or adjusted easily. For example, the carrier concentration of metals cannot be changed much with the application of moderate electric fields, optical fields, or temperature. Hence, in applications where switching or modulation of the optical properties is essential, noble metals are not the convenient choice.
Many alternative materials have been proposed that overcome one or more of the abovementioned shortcomings: alloy nanoparticles (like Au-Cd [63], Ga-Mg [64], and Ag-Au [65]), doped semiconductor nanocrystals, transparent conductive oxides (TCOs) and transition metal nitrides (TMNs), like titanium nitride.

TiN nanoparticles for LSPR applications (state of art)

TiN has become a promising alternative to gold because of its high melting point, good chemical stability at high temperatures, bio-compatibility, CMOS compatibility, and cost-effectiveness. Furthermore, TiN may offer an additional degree o freedom in the tuning of its optical properties compared to silver and gold, whose plasmonic response is typically controlled by engineering nanoparticle size and shape. In fact, as a non-stoichiometric material titanium nitride has been studied in terms of adjustable properties with varying deposition parameters.
The strength of LSPR resonance is related to the actual ε_2 value at λ_{LSPR}. The quality factor for a generic plasmonic material can be defined as the ratio between the enhanced local field and the incident field (as already discussed in section 1.2.1). For LSPR, this factor depends significantly on the shape of the metal nanoparticles; in the case of a sphere Q_{LSPR} is given by $Q_{LSPR} = -\frac{\varepsilon_1}{\varepsilon_2}$. By analyzing the quality factors for Au and TiN (see Fig. 1.19) for LSPR applications, where the complex dielectric permittivities used in this calculations are given in Fig. 1.19, it is seeable how Au outperforms titanium nitride (and zirconium nitride) over the visible and near infrared regions of the electromagnetic spectrum. However, when dealing with very small particles (i.e. nanoparticles), additional

mechanisms such as reduced electron mean free path, increased contribution from surface chemistry and shape of plasmonic material have to be considered. For this reason, Mie scattering theory is a very valid tool for the performance comparison of alternative materials for specific applications. Scattering, absorption or extinction efficiencies calculated from Mie coefficients can easily be considered as a figure of merit.

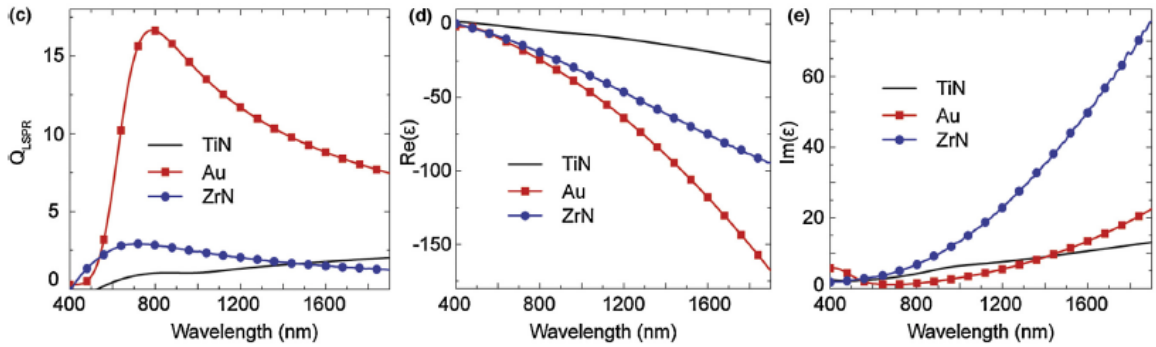

Figure 1.19: (c) Quality factors in the quasi-static regime showing the oscillator quality for Au, TiN and ZrN nanoparticles; (d) real and (e) imaginary part of dielectric permittivities used in quality factors calculations. Taken from [3].

On one side, scattering efficiency is a useful mean to estimate the performance for far field enhancement applications. As visible from Fig. 1.20 (f, g), TiN has a smaller maximum enhancement (which makes gold the material of choice for shorter wavelengths of the visible window), but at least has a broader peak and redshifted towards the biological transparency and the telecommunication windows. Overall, it can be concluded that, although it is not as a good resonator as Au, TiN provides comparable or even better field enhancement in the near-infrared region where the two very important spectral windows are present.

On the other side, absorption efficiency can be considered as a quality factor for applications based on local heating of a confined volume via absorption of electromagnetic energy. As visible from Fig. 1.20 (h, i), the peak values for Au and TiN are rather similar; in addition, TiN has a much broader peak, whose resonance tail elongates towards the biological transparency window.

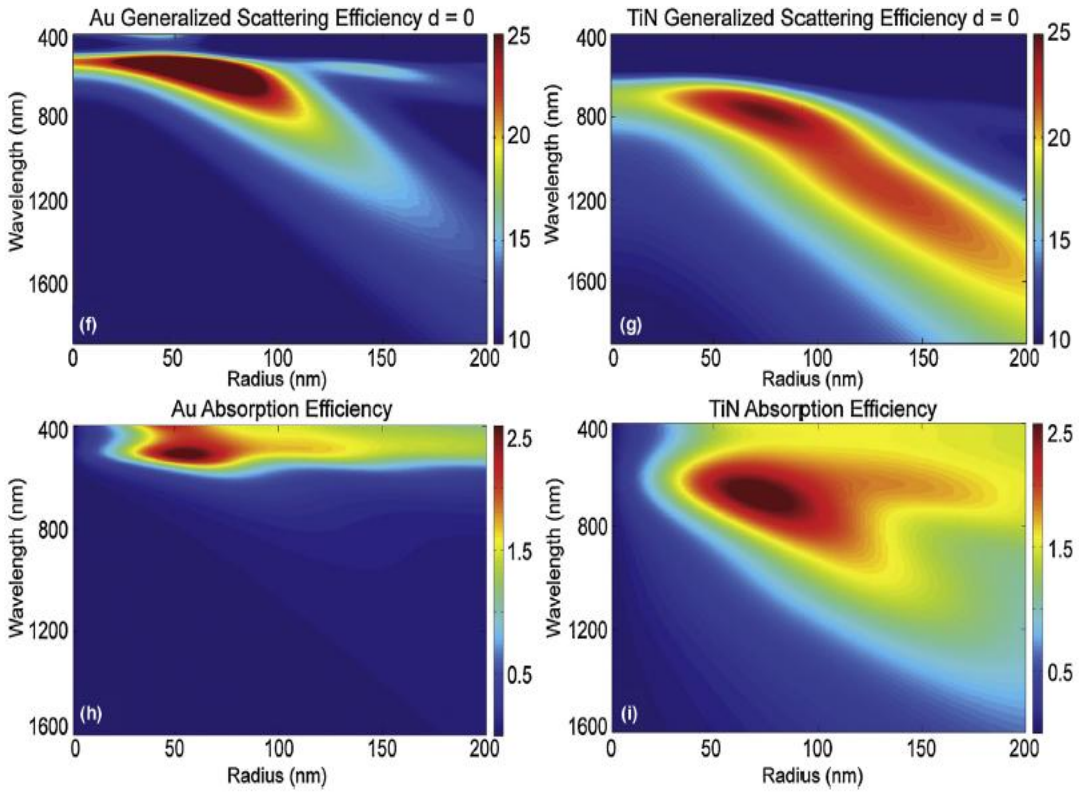

Figure 1.20: (f, g) Near field intensity efficiencies, showing the field enhancement at the surface of plasmonic particle, calculated for spherical Au and TiN nanoparticles based on Mie coefficients; (h, i) absorption efficiency, which is an efficient indicator for electromagnetic-to-heat energy conversion, for spherical Au and TiN nanoparticles with varying radii. Taken from [3].

In the following, the main LSPR (potential) applications of TiN nanoparticles based on absorption of electromagnetic energy will be discussed. Instead, application based on scattering mechanisms will not be considered here, as new developments are still emerging in the field.

- Therapeutic applications. Resonant plasmonic nanoparticles delivered to a tumor region can be heated via laser light with a wavelength in the near-infrared (NIR) region, where the attenuation of light through the biological tissue is low [3]. In this way, the concentrated heating effect generated ablates the tumor region with minimal damage to the healthy tissue (see Fig.1.21).
  Au nanostructures have been successfully used in these experiments; however, the spectral mismatch of the spherical Au NPs and the biological transparency window resulted in a need for a relatively larger dimensions and more complicated nanostructures such as nanoshells and multishells [66, 67]. The problem lays in the fact that larger size NPs have a less effective cellular uptake and clearance from the body after treatment. In order to solve the problem, Huang et al. [68] used biodegradable gold nano-vesicules made of 26 nm Au

NPs closely packed into vesicular assemblies of total sizes around 200 nm, which could be dissociated back into smaller particles after treatment for an easier clearance. However, problems of instabilities due to fragmentation were encountered.

TiN NPs, with a simple spherical shape and no size restrictions, have an even higher heating efficiency than Au NPs within the biological transparency window, hence represent a promissory research opportunity for photothermal cancer therapy (PTT).

Guler et al. [8] fabricated 30 nm thick nanodisks arrays (of various disk sizes) by electron beam lithography on a TiN film previously deposited by DC reactive magnetron sputtering at temperatures 400 and 800°C. As seen from the transmittance spectra (see Fig. 1.22), the spectral position of the transmittance dips of the TiN nanodisks exhibited plasmonic resonances throughout the biological transparency window. Instead, the plasmonic peaks of Au NPs with smaller sizes were located at relatively short wavelengths, and larger particles were required to reach the spectral region of interest.

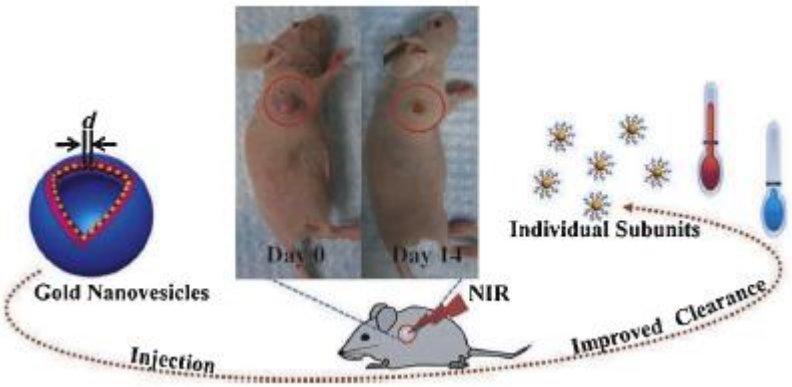

Figure 1.21: Plasmonic photothermal therapy explained in a nutshell. Plasmonic nanoparticles are injected in the body where they accumulate in tumor tissue. Then, after irradiation with a NIR laser in the biological transparency window, thanks to the enhanced absorption cross section given by NPs the tumor is ablated. The photographs of tumor bearing mice before and after treatment can be seen in the inset. Biodegradable Au nanovesicles are recently proposed for improved body clearance. Taken from [3].

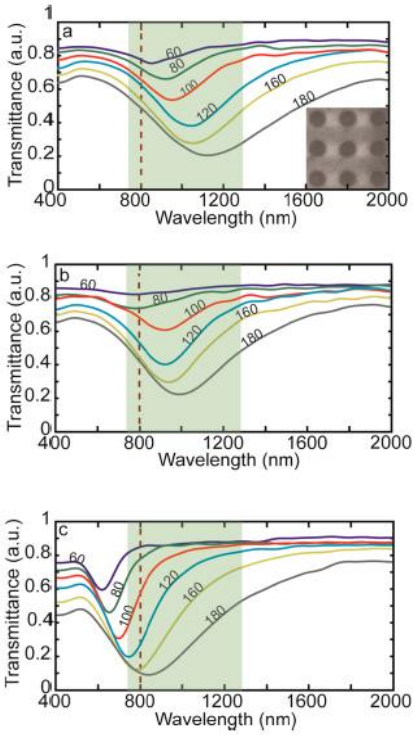

Figure 1.22: Transmittance spectra for 30 nm thick nanodisk arrays of TiN grown at (a) 400°C, (b) 800°C, and (c) Au. Different line colors indicate different nanodisk's diameter (in nm). Taken from [8].

- Solar/thermophotovoltaics applications. Some of the problems in the field of photovoltaics arise from the low light conversion efficiencies and the relatively short term stability of semiconductor devices. Absorption of light with energies higher than the bandgap of the semiconductor is known to result in heating, which in turn causes efficiency degradation. In addition, long term stability reduction due to the over-heating of semiconductors, and environmental conditions such as humidity and UV radiation are known to cause degradation of the device performance. The solar/thermophotovoltaic approach can be a solution to this multiple problems. In such devices (see Fig. 1.23), an absorber designed for broad absorption of solar radiation can be used to heat to elevated temperatures an intermediate layer. The heated body is expected to re-radiate light in the IR region of the spectrum, following Planck's law. This broad emission of light can be engineered in order to obtain a selective emission of light with a narrow energy peak just above the semiconductor's bandgap. As a result of this spectrally matched emission, high conversion efficiencies can be obtained with longer lifetimes [3].

  Because of high temperature operation in such devices, a thermally resistant material like TiN seems to be the perfect candidate for the absorber component. However, by now the reported results in this field are mostly theoretical discussions.

For example, Gao et al. [69] used a finite-difference time-domain (FDTD) software for structure modeling and numerical calculation of a broadband absorber consisting of SiO_2-TiN- SiO_2-TiN four layers structure, arranged in a ring-square array. The obtained optical properties, as shown in Fig. 1.24, were characterized by a very high absorbance spanning all over the wavelength spectrum going from 200 nm to 1200 nm. The simultaneous excitation of different resonances (propagating surface Plasmon, localized surface Plasmon, and Fabry-Perot cavity resonance) that interact with each other gave a broadband "perfect" absorption.

In addition, the Plasmon enhanced absorption of solar radiation could be exploited for solar water-heating systems. On this purpose, Ishii et al. [70] dispersed in water some TiN NPs (with average size 50 nm) produced by RF sputtering, and calculated the absorption efficiency of such system. The broad and intense plasmonic peak around 700 nm (due to high ε_2 at such wavelengths) covered most of the normalized irradiance spectrum (see Fig. 1.25), outperforming gold and carbon, that is the typical material used for solar water-heating systems.

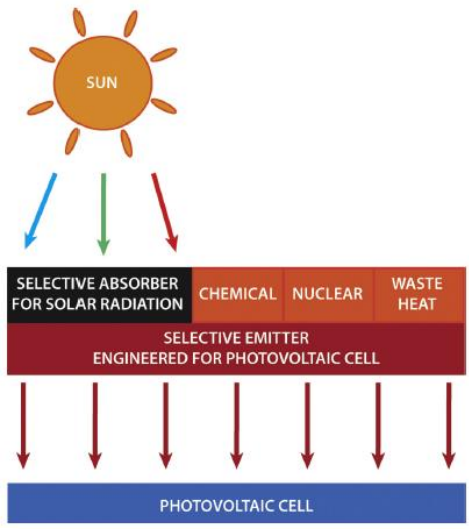

Figure 1.23: Schematic illustration of thermophotovoltaic systems. Heat input can be supplied from a variety of sources including solar, chemical, nuclear and waste heat, or any combination of these. Blackbody emission of the heated body is spectrally engineered with a selective emitter for an optimized coupling to the photovoltaic cell. Taken from [3].

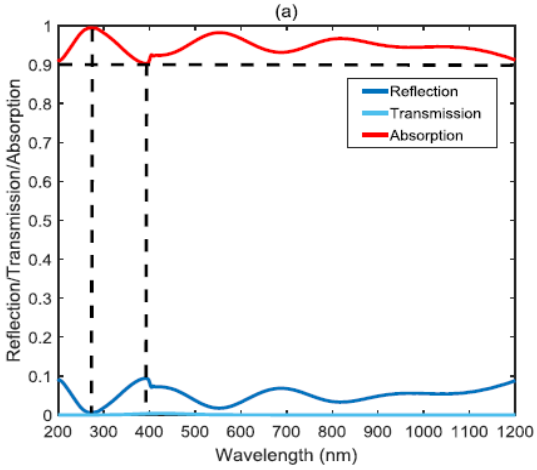

Figure 1.24: Normalized reflection, transmission and absorption spectra of four layer SiO_2-TiN- SiO_2-TiN absorber arranged in a ring-square array, under normal incidence. Taken from [69].

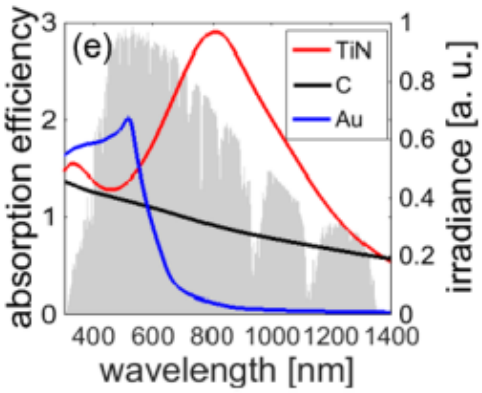

Figure 1.25: Calculated absorption efficiencies of nanospheres dispersed in water made of TiN, carbon, and Au. The radii are 50 nm. The area plot in gray color shows the normalized irradiance of AM1.5G. Taken from [70].

- Heat assisted magnetic recording (HAMR). In magnetic recording technology, achieving higher data storage densities require the reduction of bit sizes, which brings new challenges such as the loss of data in very small grains due to thermal instabilities. A promising solution to the problem is to locally heat the material to high temperatures and thus lower the coercivity for a short amount of time during the writing process. Plasmonic nanoparticle-based tips have the advantage of sub-wavelength focusing of electromagnetic energy with high field strength and heating efficiencies in a confined volume.
  However, long term stability of the optically excited plasmonic near-field transducers remains a problem due to tough operation conditions, and the search for alternative plasmonic materials has become inevitable for HAMR

technology. TiN is known to be corrosion resistant, durable at high temperatures, with stable optical properties with respect to temperature variations, and with a plasmonic performance in the NIR region (where diode laser technology is well established) comparable to Au nanoparticles. Because of these reasons, near-field transducer designs based on TiN nanostructures are believed to potentially bring the technology one step closer to real life products [71].

- Sensing applications. Due to the strong and localized electromagnetic field amplification created by the LSPR resonance, the Raman scattering of molecules (on top of which plasmonic TiN NPs are adsorbed) is greatly amplified. In this way, these molecules are more easily detected at Raman spectroscopy.

- Photocatalysis applications. The plasmonic resonance generates hot electrons, whose subsequent decay from excited states results in the creation of electron/hole pairs at high energy levels that would not be available at room temperature in absence of light excitation. The hot electrons transfer from plasmonic catalyst towards adsorbates manages to drive chemical reactions with visible light. On this purpose, Clatworthy et al. [72] investigated the ability of TiN nanoparticles to enhance the photocatalytic hydrogen evolution activity of a photocatalyst via MeOH reformation using aqueous colloidal suspensions of TiO_2-TiN nanoparticle composites. Under combined UV/Vis irradiation, the composites afford up to a 5-fold improvement in the rate of hydrogen evolution compared to TiO_2 or TiN NPs alone.

Fabrication of TiN nanoparticles and properties tuning (state of art)

Due to the non-stoichiometric nature of titanium nitride, the resonance behavior of TiN nanostructures can be tuned by varying the growth parameters. In addition, the tuning of plasmonic behavior can be done by varying the nanoparticles size.

TiN NPs can be obtained by a great variety of techniques. For instance, the direct nitridation of metal powders or metal hydrides with nitrogen or a mixture of nitrogen and hydrogen can be used [73]. However, it is difficult to precisely control the particles size, content and morphology, and the process temperatures are very high (800°C). Alternatively TiN nanoparticles can be produced by microwave and thermal plasma techniques [74, 75], but broad particles size distributions are obtained. Another way of obtaining TiN NPs is the laser ablation in solution method. Using a TiN thin film with optimized plasmonic properties as a source, one can obtain nanoparticles by ablating such film target [76]. Possible problems that may arise with the laser ablation method are the tough nature of TiN which may push the limits of the method, and the lack of control over

the nanoparticle dimension with small dispersion. Takada et al. [77] used a Ti target in a liquid nitrogen environment in order to avoid the problems that come from the hard TiN source. However, the resulting particle sizes were around 800 nm, which were far larger than dimensions typically used in plasmonic applications. Other alternative fabrication routes like plasma-enhanced chemical vapor deposition and laser ablation in liquid with laser fragmentation are being developed, in order to assure a better control over nanoparticles size and composition [78, 79]. In the following papers it will be shown how the LSPR properties of TiN NPs fabricated by different techniques have been adjusted in order to aim specific applications.

Guler et al. [80] studied the optical properties of three aqueous solutions prepared with commercially available TiN powders with average nanoparticle sizes of 20, 50 and 80 nm. By analyzing the absorption cross sections and efficiencies of the three samples (see Fig. 1.26), it was evident how the LSPR resonance red-shifted and raised in intensity the bigger was the average particles size. Moreover, if compared to Au nanoshells with inner and outer diameters of 110 and 130 nm, respectively, TiN nanoparticles showed a greater feasibility for photothermal applications: the same absorption efficiency was provided with smaller particles size. Another advantage with respect to Au nanoshells was that the broader resonance peak obtained from TiN NPs relaxed the restriction on particles size dispersion.

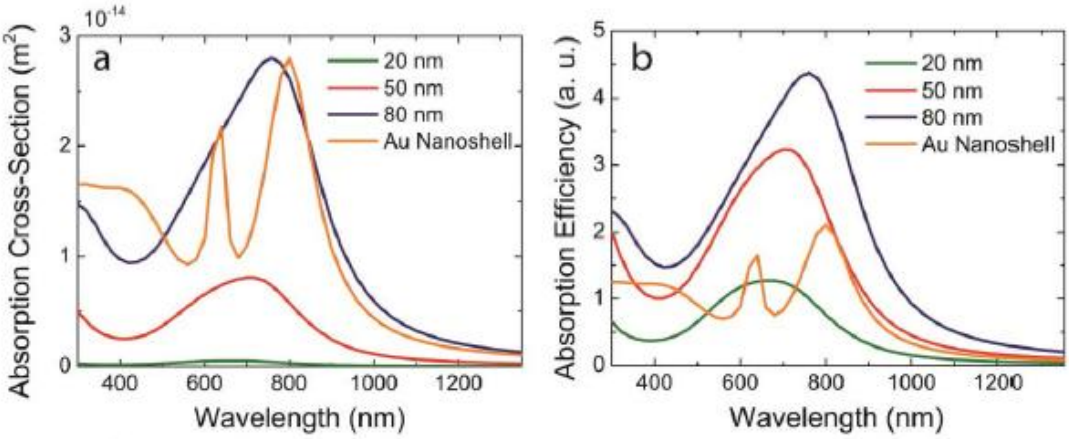

Figure 1.26: (a) Calculated absorption cross section of TiN nanoparticles with sizes 20, 50, and 80 nm compared to Au nanoshells with inner and outer diameters of 110 and 130 nm, respectively. (b) Absorption efficiencies of the same nanoparticles. Taken from [80].

In another work, Yick et al. [81] produced free standing monocrystalline cubic TiN nanoparticles by transferred arc plasma method. They showed that the operating parameters such as gas composition and arc-current had a significant influence on the TiN composition and optical properties. In particular (see in Tab. 1.1), as the helium component of the He:N_2 atmosphere increased, a slight increase of the oxygenated component at the

expense of TiN was observed. This trend was attributed to the fact that the amount of reactive nitrogen species present in the arc lowered as the relative N_2 concentration of the working gas decreased, and to the fact that higher He percentage diminished the arc reactivity. In fact, modeling has predicted that an increasing inclusion of N_2 could raise the temperature profile of the arc and hence its reactivity.

Moreover, the effect of arc current variation was analyzed. As the current increased, the dissociation of molecular nitrogen and thus the availability of nitrogen radicals rose; in addition, the amount of material evaporated got higher because of the plasma temperature increase. The results can be seen in Tab. 1.2, where an increasing current led to greatly lower oxidized fractions.

Additionally, the optical properties variation as a function of gas composition and arc current were investigated. On one side, since the position of the plasmon peak indicates the metallic nature (concentration of conduction electrons *N*) of the material, varying the gas composition did not shift the plasmonic peak position; in fact the compositional variation was not big enough (Tab. 1.1). Instead, the peak blue-shifted with increasing current (see Fig. 1.27) from $\lambda \sim 900$ nm to $\lambda \sim 700$ nm thanks to the substantial increase of the free electrons-containing TiN with respect to oxidized phases (Tab. 1.2). On the other side, the peak widths can change as a result of morphological factors. This can be seen in the size dependence of the damping factor γ_{NP}. In fact, higher arc currents led to narrower peaks (Fig. 1.27), because of the bigger diameters of the so obtained NPs.

It has to be specified that the size of NPs, as described by Mie theory, also affects the plasmonic peak position: larger particles have a lower frequency of resonance for collective charges oscillations. Furthermore, the concentration of conduction electrons *N*, which is inversely proportional to the TiO_2-to-TiN ratio of the TiN NP, has also an impactful influence on the damping factor γ_{NP}: a higher concentration of conduction electrons inevitably increases the scattering losses hence decreasing the bulk relaxation time.

All the possible effects generated by the different contributions have to be accounted when analyzing TiN optical properties. One or the other contribution will be more relevant at a time, depending on the specific case.

He: N_2	Ti-O_2	Ti-N_xO_y	Ti-N
1:1	63.2%	22.7%	14.0%
2:1	62.7%	26.3%	11.1%
3:1	66.5%	22.7%	10.8%

Table 1.1: Composition of TiN NPs at various gas compositions. Values calculated from XPS measurements. Taken from [81].

Current (A)	$Ti\text{-}O_2$	$Ti\text{-}N_xO_y$	Ti-N
100A	54.7%	30.1%	15.2%
150A	46.7%	33.4%	19.8%
210A	42.6%	27.2%	30.2%

Table 1.2: Composition of TiN NPs at various arc currents. Values calculated from XPS measurements. Taken from [81].

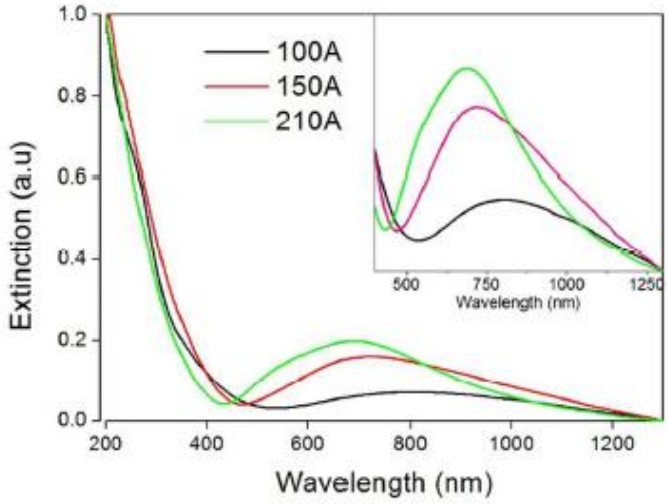

Figure 1.27: Optical extinction measurements of TiN nanoparticles synthesized at different arc currents. Taken from [81].

Other important parameters affecting TiN NPs plasmonic response are the nanoparticles concentration in solution and the dielectric constant of the solvent.

He et al. [82] investigated the dependence of the plasmonic resonance on the concentration of TiN nanoparticles in a colloidal solution. With a NPs concentration higher than 20 $\mu g \cdot mL^{-1}$ a broad-band absorption in the near-IR due to plasmonic resonance started to be visible (see Fig. 1.28). Consequently, the temperature elevation of such colloidal solutions as a function of irradiation time resulted to be greater when the NPs concentration was increased (Fig. 1.28b).

Baturina et al. [83] performed UV-Vis spectrophotometer analysis on aqueous colloidal solutions with different concentrations of 20 and 50 nm TiN NPs. For 20 nm NPs solutions a broad plasmonic resonance located around 650 nm was observed, with increasing intensity for greater NPs concentrations (see Fig. 1.29a). For 50 nm NPs solutions the LSPR peak was narrower and red-shifted to 665 nm, and showed the same dependence on NPs concentration as for smaller particles (see Fig. 1.29b).

Extinction measurements of titanium nitride nanoparticles in solvents with different refractive index (*n*) show how the frequency of the LSPR resonance decreases if the surrounding medium has an higher value of *n* (Fig. 1.30).

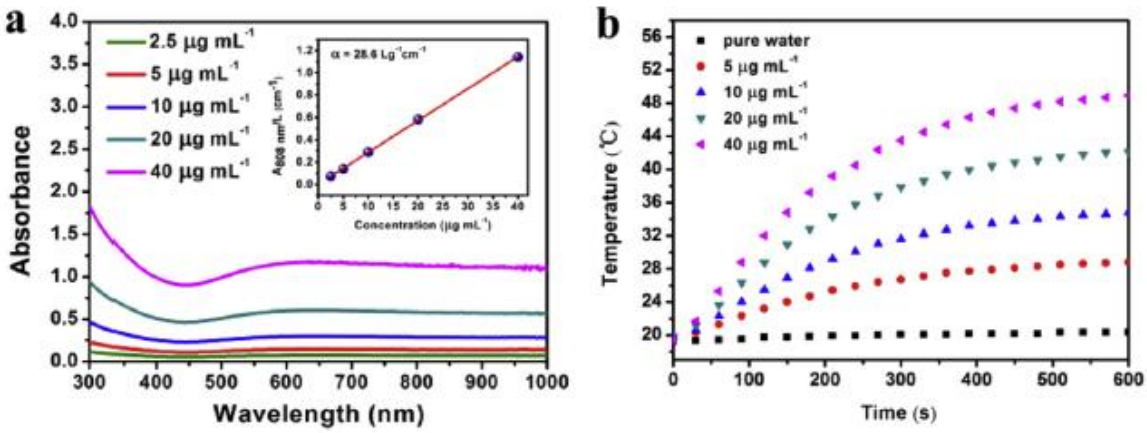

Figure 1.28: UV-Vis-NIR absorption of aqueous solutions of TiN NPs diluted at different concentrations. Inset: normalized absorbance intensity for λ = 808 nm divided by the characteristic length of the cell as a function of NPs concentrations; (b) temperature elevation of pure water and TiN NPs aqueous solution at different concentrations as a function of the irradiation time. Taken from [82].

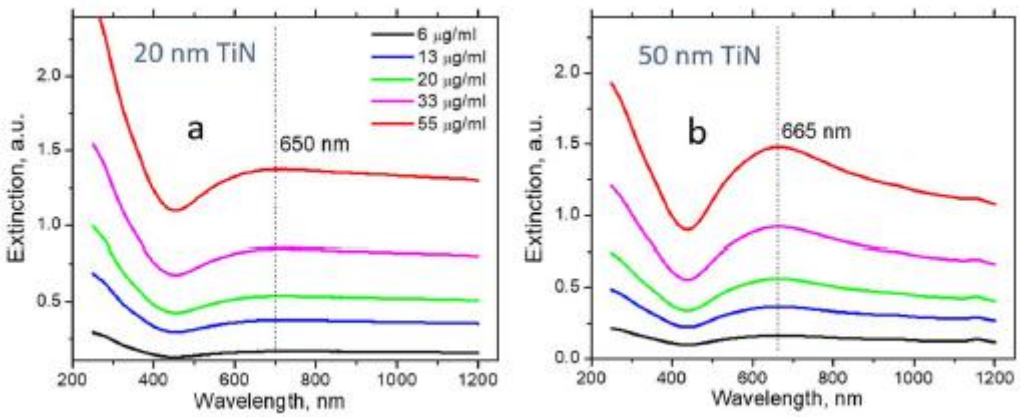

Figure 1.29: Experimental UV-Vis spectra recorded in aqueous colloidal solutions of (a) 20 nm and (b) 50 nm TiN nanoparticles of different concentrations.. The dashed lines indicate the wavelength associated to the LSPR peak. Taken from [83].

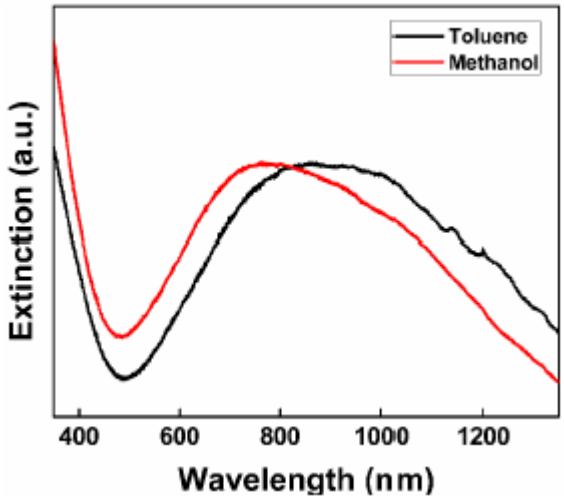

Figure 1.30: Extinction measurements on ~ 8 nm TiN nanoparticles in solvents with different refractive index ($n_{methanol}$ = 1.33; $n_{toluene}$ = 1.49). Taken from [79].

Recently, Popov et al. [78] prepared two colloidal solutions of TiN NPs by laser ablation of a titanium nitride target placed in a vessel filled once with water and once with acetone. Nanoparticles with an average diameter of 30 nm and with rock-salt cubic structure were obtained. Then, in order to reduce the size and to narrow the size distribution, which is essential to have proper renal filtration in biomedical applications, such colloidal solutions were exposed to radiation of the same laser in the absence of the target: the so-called laser fragmentation process. In this way, the average diameter was decreased to 5 nm and the size dispersion was seized down. After fragmentation the water solution of TiN NPs presented a fast loss of blue coloration, related to the disappearance of the plasmonic peak. The extinction spectra got similar to the one of TiO_2, indicating the higher oxidation extent occurred for the smaller diameters NPs. On the other side, in acetone the oxidation was limited, and the plasmonic peak in the NIR (600-800 nm) survived (Fig. 1.31).
The oxidation issue related to TiN nanoparticles have been treated only by few other study researches. For instance, Barragàn et al. [79] studied the effect of oxidation on TiN NPs optical properties. The particles were prepared via a plasma-enhanced chemical vapor deposition method, using a $TiCl_4$ precursor, a NH_3 reactive gas at different flow rates, an Ar carrier gas and keeping low temperatures. The NPs produced at lower NH_3 flow rates appeared bigger (average diameter 8 nm) and with a neater cubic shape compared to smaller NPs (average diameter 4 nm) fabricated at lower $TiCl_4$/ NH_3 ratios. The oxidation issue rose when considering that the extinction peaks of bigger particles were blue-shifted: this seemed in contrast with Mie theory dependence of plasmonic peak with size; in fact, according to the theory bigger particles show red-shifted peaks. The reason for this behavior was found by air-annealing the NPs at different temperatures. The extinction spectra red-shifted, got broader, and eventually fade away when the air-annealing temperature was increased. Since oxidation extent is directly related to air-annealing temperature, such absorption spectrum variation was not dependent much on particles size but rather on their oxidation extent once exposed to air after deposition (see Fig. 1.32). As

a confirm, smaller particles appeared from X-ray photoelectron spectroscopy (XPS) measurements nitrogen-deficient and oxygen-rich, while bigger ones were almost stoichiometric and had a lower oxygen content, mostly on surface. In order to prevent the red-shift of plasmonic peak due to oxidation, which additionally lower the intensity and can lead to fading of the LSPR resonance, a silicon-oxynitride diffusive barrier layer was deposited as a capping for the nanoparticles. Such capping layer was obtained by adding, in a second moment, SiH_4 precursor in the chamber. As seeable from Fig. 1.33, an overall blue-shift, narrowing and enhancement of the plasmonic peak was observed for coated TiN with respect to bare TiN; moreover, an increased thermal stability of optical properties upon air-annealing was achieved.

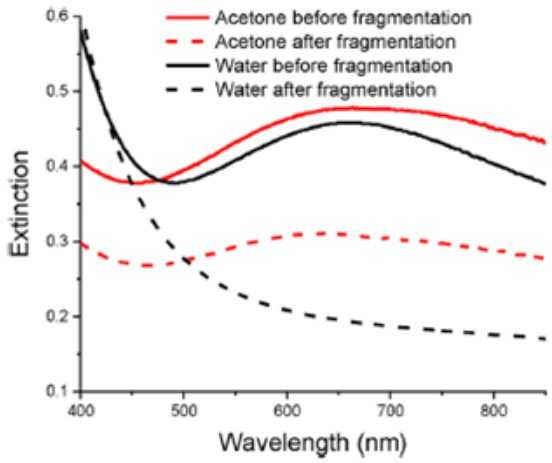

Figure 1.31: Extinction spectra of 30 nm TiN NPs synthesized by pulsed laser ablation in liquid. NPs prepared in water (black) and in acetone (red) before (solid lines) and after (dashed lines) femtosecond laser fragmentation of initial NPs. Taken from [78].

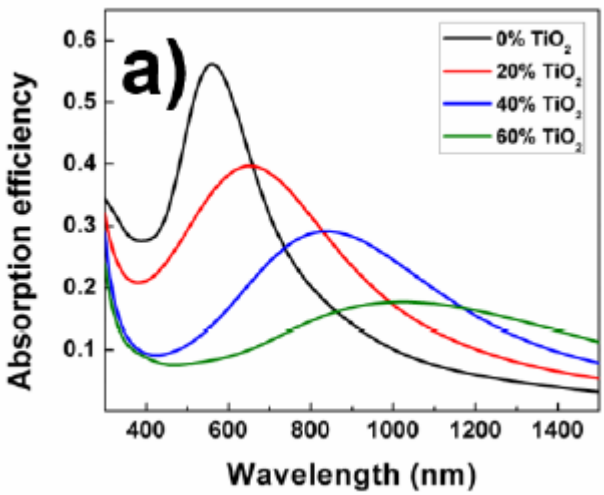

Figure 1.32: FTDT simulation of absorption efficiency of a 10 nm TiN nanoparticle with different degrees of oxidation. Taken from [79].

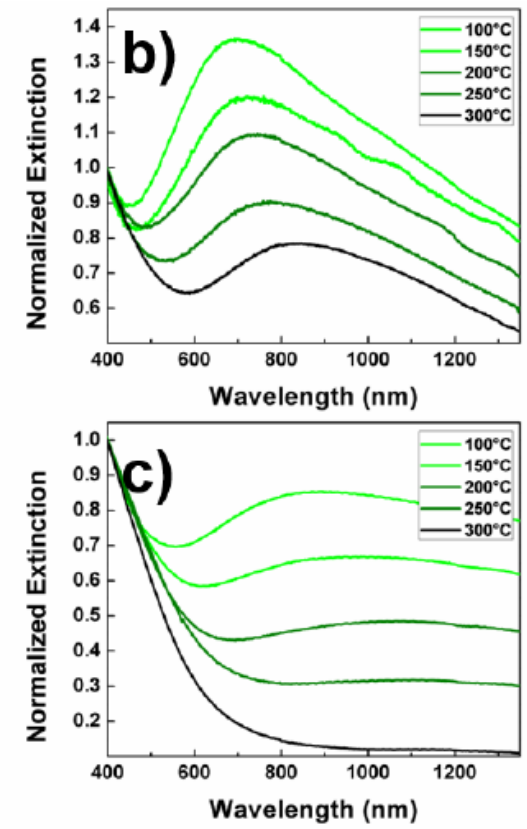

Figure 1.33: (b) normalized extinction of SiO_xN_y-coated TiN nanoparticles after an air-annealing process at increasing temperatures; (c) normalized extinction of bare TiN nanoparticles after an air-annealing process at increasing temperatures. Taken from [79].

1.3.2 TiN NPs assemblies: nanostructured thin films

In the middle between a compact thin film and isolated nanoparticle morphologies, the so-called nanostructured or hierarchical thin films are present. Such films are characterized by assemblies of nanoparticles with various size, shape and architectures. Their nanoporosity and extremely high surface area make them not only highly interesting for various applications, but also promising for a wide range of possible developments.

Obviously, as a direct consequence of their very high porosity and open structure, nanostructured thin films are very prone to external agents action; in particular, if the material suffers oxidation already when its morphology is compact, such issue will become critical both during the synthesis process of the hierarchical film and after its exposure to air.

Already in 2010, Cortie et al. [84] used a nanosphere-template technique in order to fabricate TiN thin films with a nanoscale semi-shell motif. Their aim was to analyze the optical phenomena operating in such nanostructures using a combination of experiment and simulation, and to show that semi-shells of TiN exhibit a tunable localized plasmon

resonance. Titanium nitride was deposited by magnetron sputtering of a Ti target in N_2 3 $\cdot 10^{-2}$ Pa atmosphere on top of a layer of spherical polystyrene particles of 200 nm diameter , previously spun-cast onto a glass substrate. Figure 1.34a shows a typical semi-shell structure obtained, which is characterized by a rough upper surface (Fig. 1.34b). The reflectance and transmittance of such array of TiN semi-shells were compared to that of a plain TiN thin film (see Fig. 1.35). Both the array and the plain samples had the same nominal coverage of TiN, produced by identical chamber deposition conditions. It could be seen that the big differences in optical properties between the two sample geometries were:

- The transmittance rose for $\lambda > 900\, nm$ for nanostructured film, while it decreased for the plain one.
- The reflectivity of compact thin film was significantly higher than that of nanostructured film, because of the much higher concentration of charge carriers.

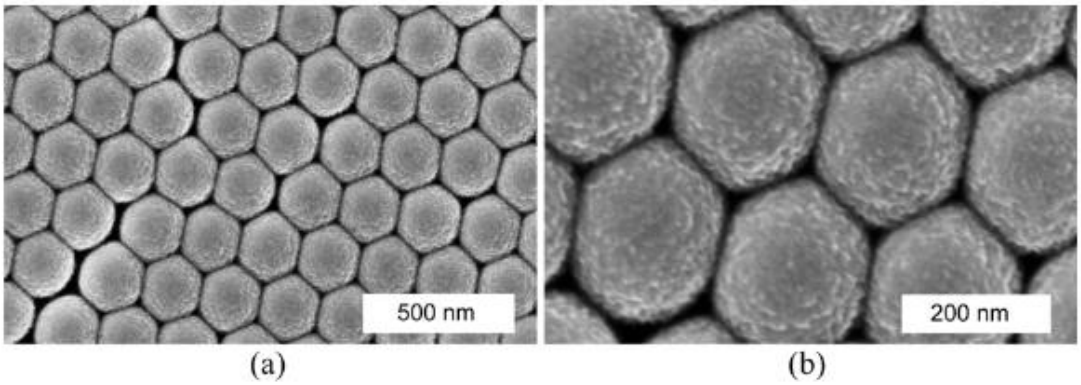

Figure 1.34: (a) Scanning electron microscope (SEM) image of an array of TiN semi-shells formed on a colloidal crystal monolayer of polystyrene nanospheres; (b) High-magnification view of TiN deposit, showing surface roughness. Taken from [84].

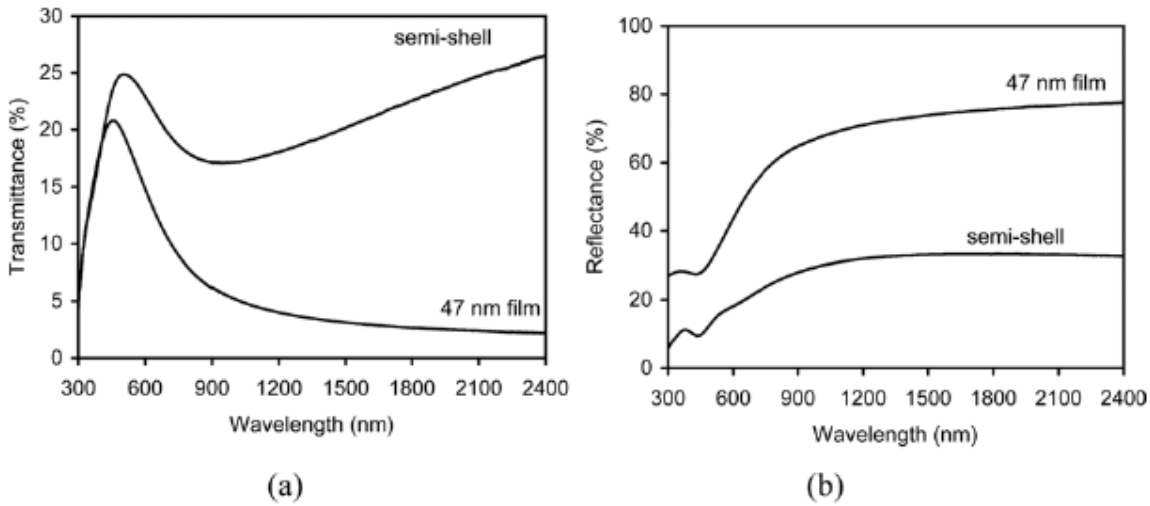

Figure 1.35: Optical properties of arrays of TiN semi-shells compared to those of a TiN thin film deposited under the same conditions. (a) Transmittance; (b) reflectance. Taken from [84].

Later on, Kaisar et al. [4] prepared TiN films by reactive sputter deposition onto a silicone oil-coated Si substrate and obtained a wrinkled morphology (see Fig. 1.36). After deposition, the silicone oil was evaporated. The resulting wrinkly TiN film was compared with flat TiN film deposited on a blank Si substrate for Surface Enhanced Raman Scattering (SERS) study using R6G as the Raman probe molecule. Raman intensity enhancement of ~ $1.3 \cdot 10^4$ was demonstrated for the wrinkly film. In fact, thanks to its nanoscaled granular morphology, a local electromagnetic field enhancement occurred in the high curvature regions; moreover, besides the fact that more adsorption sites were present because of the higher surface area, thanks to its hierarchical wrinkles with average size 80 nm a higher signal was given at wrinkles' ridges and nanogaps. The surface plasmon resonance (SPR) wavelength, in correspondence of which the extinction cross section peak had its maximum, was found to be centered around 550 nm. Such SPR wavelength was similar to those reported by other experimental works. For instance, Dong et al. [85] found an absorption peak centered around 480 nm for nano-sized TiN thin film fabricated via nitridation of sol-gel derived TiO_2 film. The obtained structure was porous, due to the decomposition of the residual polyvinylpyrrolidone PVP (that was used for sol-gel process) during nitridation (see Fig. 1.37). An island-like particles clustering resulted in a high roughness and open structure, which resembled to be highly suitable for SERS applications: a Raman intensity enhancement of ~ $4.1 \cdot 10^3$ was obtained.

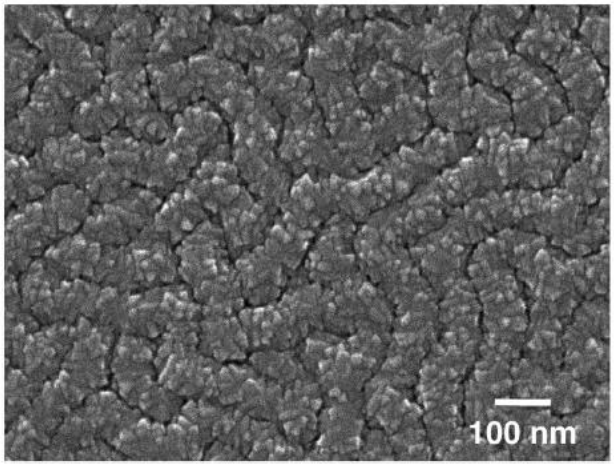

Figure 1.36: SEM top view image of wrinkly nanostructured TiN film. Taken from [4].

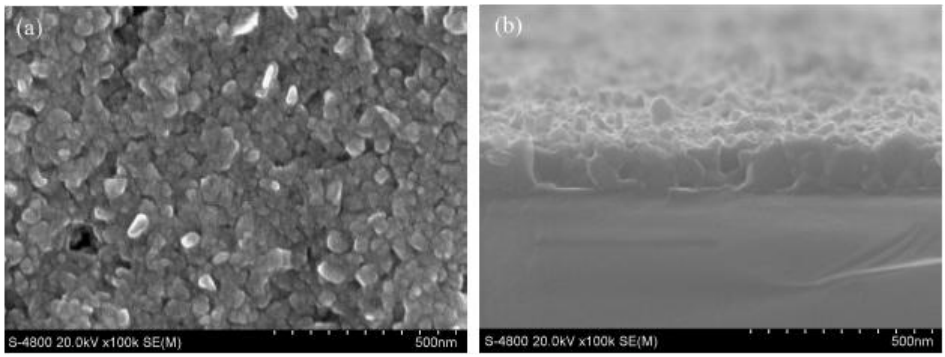

Figure 1.37: SEM images from the surface and cross section of nanoporous thin TiN film obtained via TiO_2 nitridation at 1000°C for 2 hr. Taken from [85].

The general synthetic approaches for nanoporous titanium metal nitrides had heavily depended on templates methods, and the necessary removal of the templates were usually incomplete, hazardous, time and energy consuming [86]. In this regard, the rational synthesis of highly porous TiN-based nanostructure with a facile and highly efficient strategy at low cost is extremely desirable, but it is still a challenge.
In the beginning of 2019, Liu et al. [6] developed a two step route for the synthesis of 3D, porous TiN architectures with well defined shape, size and composition. The two steps consisted of a simple solvothermal process and a subsequent high temperature nitriding process of the TiO_2 precursors. The obtained 3D urchin-like TiN nanostructures (Fig. 1.38) were composed of plentiful and highly interconnected thin nanowires (NWs), which exhibited a high surface area and effective charge transfer. In addition, the as-synthesized materials showed excellent electrochemical stability of structure and compositions, and the existence of enormous sharp corners and edges which hold great potential for the high performance of various catalytic processes.

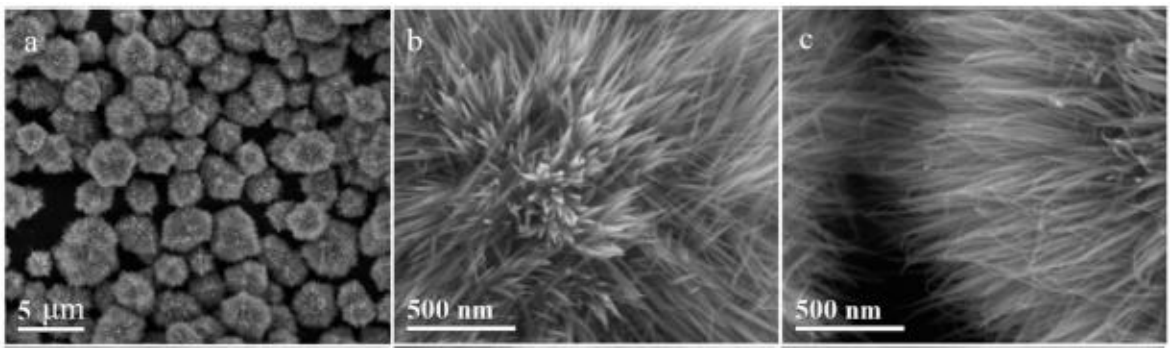

Figure 1.38: SEM images of urchin-like TiN architectures. Taken from [6].

In the same year, Perego et al. [87] realized a hierarchical TiN nanostructured thin film electrode consisting in an array of quasi-1D TiN nanostructures grown via pulsed laser

deposition technique. Thanks to its great versatility, the PLD process made it possible to fabricate a thin film whose morphology (see Fig. 1.39) consisted of tree-like nanostructures (also called *nanoforest*) with outstanding chemical stability, good conductivity, tunable porosity and high roughness factor. Deposition was performed, after previously evacuating the chamber to a base pressure of $3 \cdot 10^{-3}$ Pa, in a N_2-H_2 (95-5%) atmosphere at different operation pressures (from 15 to 100 Pa) with the aim of tuning the resulting thin film morphology. The fluence of the KrF excimer laser ($\lambda = 280\ nm$) was set constant at the value 3.4 J/cm^2. The evolution of films mesostructure from columnar (at 15 Pa) to tree-like (at 30 Pa) and to areogel-like (at 100 Pa) translated in a relevant increase in the thickness, total pore volume and mean pore size with pressure, and a decrease in density (see Fig. 1.40). A high percentage of oxygen (> 35 % at) was found by high-angle annular dark field STEM, probably due to the oxidized surface layer present all over the vast surface area. Raman spectra, which were obtained with a IR diode laser ($\lambda = 785\ nm$) with power $P = 100\ mW$, reported the presence of slightly sub-stoichiometric TiN (Fig. 1.41). Moreover, from high-resolution TEM and XRD measurements the presence of nanocrystalline TiN domains (composed by TiN cubic crystals of 7-8 nm size) immersed inside an amorphous matrix was encountered. In conclusion, thanks to PLD versatility, they managed to fabricate a stable electrode, which demonstrated high electrochemically active surface area and power densities.

Eventually, in the late 2019, Podder et al. [5] tuned the plasmon absorbance band of nanostructured TiN films from visible to NIR region by varying the stoichiometry of the samples along with changing of size and distribution of the nanoparticles. TiN nanostructures having different morphology were synthesized by pulsed DC reactive magnetron sputtering technique by varying the working pressure and the deposition time. Being a dry plasma-based process, it had the advantage of forming very stable nanostructures which improve the quality of the fabricated device. These films with finely tuned LSPR bands were incorporated into two IR photodetectors operating in different wavelength ranges, improving their performances in terms of light harvesting efficiency. The first sample, named TiN-1 in Fig. 1.42, was produced at higher pressure (p = 15 Pa) and hence was constituted by an assembly of spherical NPs of average size ~ 6.5 nm (with a rather narrow size dispersion). The LSPR peak laid in the visible ($\lambda = 570\ nm$). On the other side, the second sample (TiN-2 in Fig. 1.42) was made at lower pressure (p = 7.5 Pa); consequently it was characterized by a nanostructure formed by spheroidal nanoparticles with quite heterogeneous sizes with an average value of ~ 12 nm. In this case the LSPR peak was lower in intensity, much broader, red-shifted towards the NIR and centered at $\lambda = 1000\ nm$. In Fig. 1.43, the transmittance spectra of TiN-1 and TiN-2 are shown. Stoichiometry played a very important role in tuning the LSPR of TiN samples. From XPS analysis, the amount of titanium atom in TiN-1 and TiN-2 was 37.42% and 36.05% respectively, while the nitrogen atomic percentage was estimated to be 2.07% and 32.64% respectively. An higher nitrogen concentration led to lower carrier concentration and the departure from metallic character: the LSPR resonance red-shifted and decreased in intensity. Moreover, the ratio of Ti-N over Ti-N-O in sample TiN-1 was 0.58, while it was

0.40 for TiN-2: an higher oxygen incorporation caused an additional further distance from the metallic behavior.

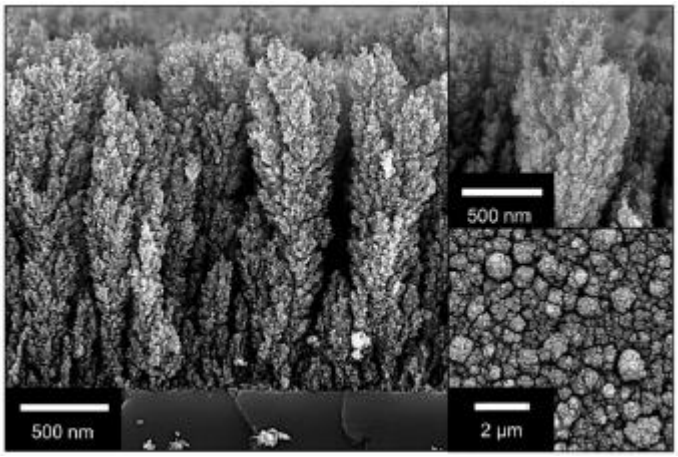

Figure 1.39: Cross-section SEM image of TiN nanostructures grown at 60 Pa N_2-H_2 by Pulsed Laser Deposition. Details and top-view in the inset. Taken from [87].

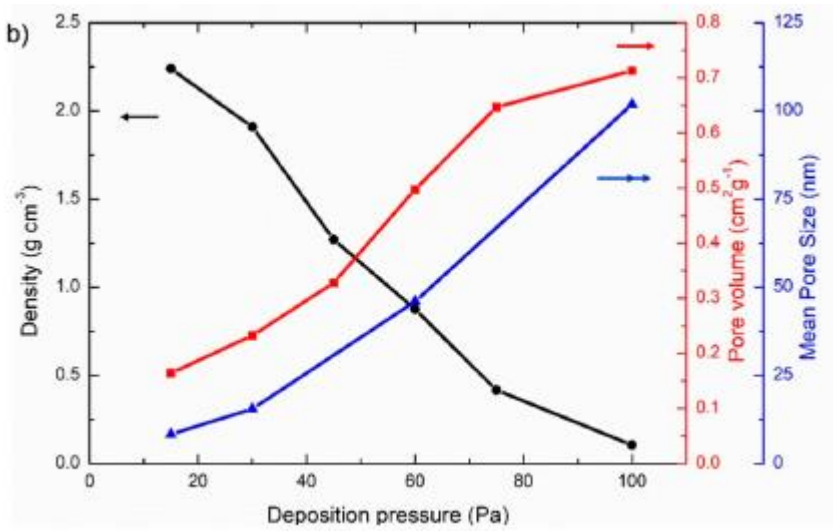

Figure 1.40: Density, pore volume, and mean pore size dependency on the operating pressure of the hierarchical TiN nanostructured thin films. Taken from [87].

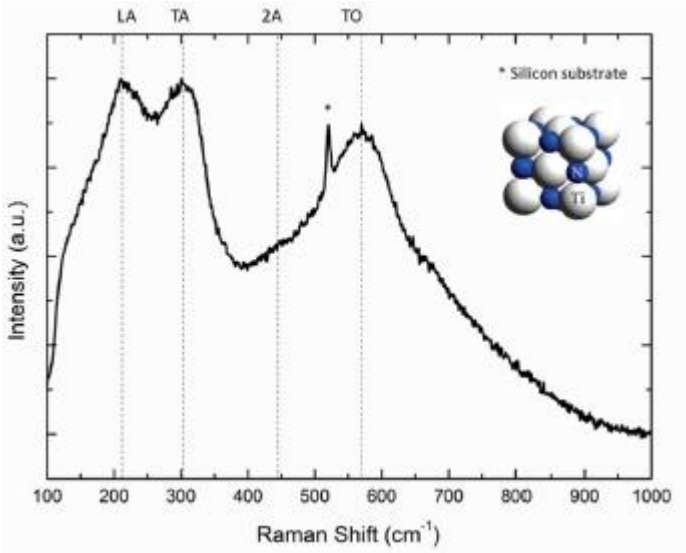

Figure 1.41: Raman spectrum of the hierarchical TiN nanostructured thin film with indication of the position of the vibrational modes from the literature. Taken from [87].

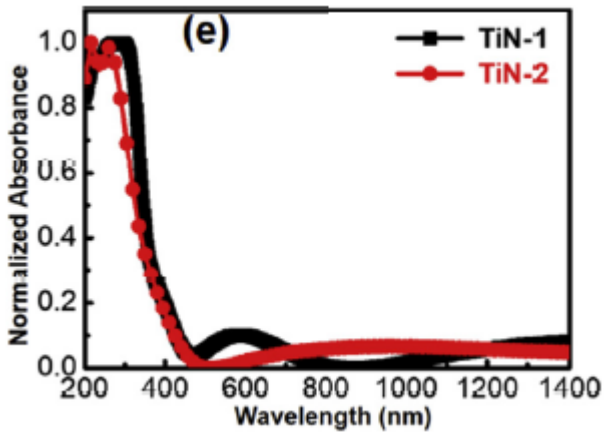

Figure 1.42: tuning of LSPR of TiN from visible to NIR region by varying the deposition pressure. Taken from [5].

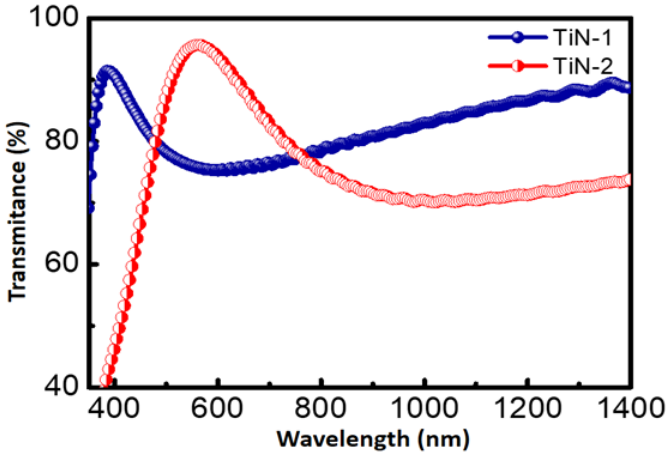

Figure 1.43: Transmittance spectra showing the tuning of LSPR from visible to NIR region by changing deposition pressure. Taken from [5].

Conclusions

In conclusion, various groups have demonstrated that TiN NPs are a promising alternative plasmonic material, being able to provide light energy harvesting as well as near-field enhancement due to their localized surface plasmon resonance. The resonant peaks naturally fall in the visible and NIR region of the electromagnetic spectrum, where TiN performance is comparable to that of gold. However, there are not enough studies in literature regarding TiN NPs in order to get a systematic and extensive comprehension about size and stoichiometry tuning and about their relation to LSPR peak position, intensity and width. Only some scattered examples are present, from which it is possible to summarize the following main achievements.

First of all, the peak width is mostly depending on particle size and particle sizes dispersion, but also on the plasma frequency ω_p. In fact, higher values of conduction electrons N increase the dumping term of the Drude model, hence generating a peak broadening. In addition, the plasma frequency directly depends on the free electron density N, and therefore it is inversely proportional to the nitrogen-to-titanium (i.e. N/Ti) and to the oxide phases-to-TiN phases (i.e. TiO_2/TiN) ratios. Because of this, an higher oxidation and/or an higher nitrogen incorporation lead to broader peaks. Furthermore, the relation between peak width and particles size can be understood through the equation $\gamma_{NP} = \gamma_{bulk} + \frac{AV_F}{D}$: bigger particles have smaller damping factor and so narrower LSPR peak.

Besides, the peak position is mainly affected by the nanoparticle composition and size. The size depends on the growth conditions (like gas flow rate, deposition rate, temperature, etc.) and fabrication technique. The typical sizes of the obtained TiN NPs go from 5 nm to 80 nm, giving a red-shift of the LSPR peak position from $\lambda \sim 600\, nm$ to $\lambda \sim 800\, nm$. Thus, the influence of size on LSPR peak position is rather small. On the other side the influence of composition on peak position is more relevant. Nevertheless, the control over stoichiometry (i.e. N/Ti ratio) has not been completely achieved yet, since the high presence of oxygen makes the N/Ti ratio very low and in general extremely difficult to adjust; consequently, by now, the N/O ratio has been the only tunable parameter. N/O ratios from 0.10 to 0.60 have been obtained, and the percentage of oxide phases in TiN NPs has been found to be typically around 50-60 %, hence giving LSPR broad bands centered around $\lambda \sim 1000\, nm$ with very low intensity. Since oxidation strongly influences composition, it plays a crucial role in determining the optical properties of TiN NPs. However, only few groups have tried to cope with this problem: laser ablation in acetone resulted to give more intense plasmonic peak due to lower NPs oxidation than in water; capping layer of Si_3N_4 on top of the NPs seemed to lower the air-exposure oxidation; and high arc currents in arc plasma method produced NPs with lower oxide phases due to higher reactivity of nitrogen radicals in the plasma.

Furthermore, few researches have focused on the fabrication of TiN nanostructured thin films with various architectures, considered as promising candidates for various

applications where an high specific surface area and porosity are needed (like substrates for Surface Enhanced Raman Scattering or electrodes for fuel cells). From the very few and scattered works investigating the plasmonic response of nanostructured TiN films, this seems to consist in a localized surface plasmon resonance occurring in a vast wavelength range spanning from $\lambda \sim 450\ nm$ up to the near-IR region ($\lambda \sim 1000\ nm$). As for isolated nanoparticles, the LSPR peak position, width and intensity are expected to be highly depending on morphological factors (like NPs size, size distribution and arrangement in space), and on film stoichiometry (N/Ti and Ti-N/Ti-N-O ratios). However, in literature only scarce examples of TiN nanostructures can be found, where very different architectures are examined. Moreover, very few of these papers take into consideration the plasmonic properties of such films. As a consequence, it is practically impossible, by now, to find any consistent correlation between optical properties and nanostructures morphology and composition (especially because only very weak and fading intraband absorption peaks have been observed: Fig. 1.46). Additionally, oxidation has only been stated as an actual issue for nanoporous films, but no strategies to reduce it have been proposed yet, nor its influence on film's plasmonic behavior has been investigated. A deeper analysis on the optical properties of such TiN films architectures, with a main focus on the oxidation issue and its influence on the plasmonic behavior, is still needed.
On this purpose, because of its great versatility (in terms of tunable deposition conditions) and possibility to control film stoichiometry, structure and morphology, Pulsed Laser Deposition could be useful in order to investigate some of the aforesaid open issues.

1.4 Objectives of this thesis

As already discussed in the previous paragraph, nanostructured TiN thin films have only been studied since a relatively short time. Thus, a detailed and systematic analysis on the optical properties of such TiN films and on optical properties-tuning, with a strong focus on the oxidation problem and its consequences on the films plasmonic behavior, is still missing. Especially, the fabrication of nanostructured TiN films using Pulsed Laser Deposition could shine some light on the relation between the deposition conditions, the films morphological and compositional features and their optical properties. For this purpose, the objective of this thesis work is in first instance the synthesis by PLD of nanoporous TiN thin films characterized by a nanostructured morphology consisting of tree-like nanoparticles assemblies. Then, their optical properties and plasmonic response are investigated. Furthermore, a strong stress is put on the possible strategies to reduce oxidation, and thus to obtain higher quality TiN nanostructured films.
The experimental work was divided in four main parts:

1. First, we studied the effect of PLD process parameters on the deposition of TiN films. In particular, we investigated the effects of background pressure of N_2-H_2 (from 5 to 100 Pa) and laser fluence (i.e. energy density) variation (2 and 3.5 J/cm^2), in order to find the optimum deposition conditions to obtain uniform and adherent films with nanostructured morphology. Moreover, such conditions were chosen in order to extend to higher background pressures a previous study carried on by our group in this laboratory; in this way, the transition from compact to nanoporous thin films was investigated in terms of density, morphology, qualitative composition and optical properties.

2. Once uniform nanostructured thin films were obtained, we dealt with the problem of oxidation, whose extent resulted to be so vast in highly nanoporous films that, in such films, titanium nitride characteristic features could not be easily observed. Hence, two approaches to limit oxidation were investigated, since it was not clear whether the most of contaminating oxygen came from air-exposure after deposition or from residual impurities in the chamber.

   a) Cap layer: aluminum nitride diffusion barriers were deposited on top of the nanoporous films without opening the vacuum chamber, in order to try to reduce surface oxidation due to air-exposure.

   b) Higher energy of plume species: depositions at high fluence (6.5 J/cm^2) were performed, in order to try to reduce oxygen incorporation during deposition. In fact, a higher energy per pulse may lead to higher nitrogen gas molecules dissociation, hence to higher nitrogen radicals reactivity in the plasma plume.

3. Then, we analyzed the effect of thermal treatments on the structure and optical properties of our samples. The annealings were performed either in vacuum or with N_2-H_2 (95-5 %) supply at controlled overpressure of 1050 mbar; the process time was kept constant while two different temperatures were selected (300 and 550°C, similar to those used in literature). In particular, after annealing in vacuum a higher film crystallinity and the desorption of surface oxygen were expected, while after annealing in N_2-H_2 atmosphere the film composition was expected to become enriched in nitrogen and depleted in oxygen, and the film crystallinity was likely to improve as well. Two different annealing temperatures (i.e. 300 and 550°C) were investigated in order to find a good compromise between amorphous phase oxidation and crystallization (which are both favored by higher temperatures).

4. Finally, only for compact films, a first attempt of nitrogen ion beam-assisted deposition was performed. The electrical and optical properties were investigated, and very good results in terms of electrical properties and stoichiometry were obtained, which could be further developed in future studies.

All samples in this study were synthesized by pulsed laser deposition at room temperature on silicon and glass substrates, in a N_2-H_2 (95-5 %) atmosphere. The obtained films were characterized in terms of structure and morphology using scanning electron microscopy (SEM) and Raman spectroscopy. The optical properties were investigated by UV/Vis/NIR spectrophotometry. Finally, the standard four-point probe method was used for the electrical measurements of the compact films fabricated with a nitrogen ion-beam-assisted deposition.

Experimental methods

2.1 Pulsed Laser Deposition

Pulsed Laser Deposition (PLD) belongs to the family of Physical Vapor Deposition (PVD) techniques as it is based on the production of a plasma from a target material irradiated by intense laser pulses. It is a simple yet versatile deposition method, able to produce compact and nanostructured films, either metallic, polymeric, oxide, semiconducting or ceramic. Along with the possibility to deposit a wide range of materials, another main advantage of PLD is the capability to produce films with highly complex stoichiometry.
The properties of the deposited film strongly depend on the deposition conditions, which influence the formation of the plasma plume and the generation and propagation of aggregates such as nanoparticles, clusters and molecules. Therefore, by choosing appropriate deposition conditions, it is possible to adjust the growth process in order to produce films with a great variety of morphologies, in a wide range of thicknesses and densities. Moreover, in the absence of reactions with the background gas, the target stoichiometry can be maintained in the deposited film.
On the other side, this large numbers of parameters affects the reproducibility of the process, which, in some cases, turns out to be low. In addition to this, another drawback of the technique is the difficulty to obtain a uniform substrate coverage for surfaces larger than few cm^2, due to the inhomogeneous angular distribution of energy in the plume, and due to shadow effects which only allow deposition on planar substrates. Furthermore, the quality of the deposited film is often reduced by the re-deposition of drops of molten material on the target surface, especially for low-melting target materials (like metals). Consequently, other techniques (like sputtering) are preferred above PLD for industrial applications.

In Fig. 2.1 a schematic diagram of PLD apparatus is shown, and it is composed by a laser source and a vacuum chamber containing the target material and the substrate. Laser pulses hit the target at an angle of about 45° with respect to the normal, while the substrate is located in front of the target. In order to ensure a uniform ablation of the target and a uniform deposition on the substrate, the latter experiences a rotational motion, while the former undergoes a roto-translation. As well as a uniformly covered substrate, also a uniformly ablated target is desirable, in order to have a selfconsistent plasma plume and consequently an even deposition. The uniform deposition area is of the order of some square centimeters.
The apparatus is also equipped with a RF ion source (see section 2.1.1.) and with systems for the control of deposition rate (quartz crystal microbalance, QCM). QCM device consists in a vibrating quartz piece which must be placed close to the substrate, in a region

deemed to undergo the same level of covering as the actual film. The increase in film thickness results in a change in the vibration frequency, as the crystal gets covered. In this way, film growth can be monitored in real time.

The deposition process takes place inside a vacuum chamber, typically made of stainless steel. Vacuum is obtained by a pumping system which consists of a primary scroll pump and a turbomolecular pump, which are connected in series, and a gas inlet system. The pressure is measured with different methods according to the pressure range. The primary pump typically reaches pressures in the order of 1 Pa, while the turbomolecular pump can bring the pressure down to 10^{-4} Pa. After vacuum is made, the target is irradiated with laser pulses of a certain intensity and duration (in this work, between 160-510 mJ and ~6 ns, respectively). When the energy density (fluence) exceeds a threshold value, depending on the target material, a cloud of vaporized (ablated) species (atoms, molecules, ions, electrons and clusters) is produced, forming a plasma. The aforesaid ablated species expand in the deposition chamber, which can be filled with a background gas, forming a visible "plume" that travels in the direction perpendicular to the target. Eventually, the ablated species reach the substrate placed in front of the target, producing the deposited film.

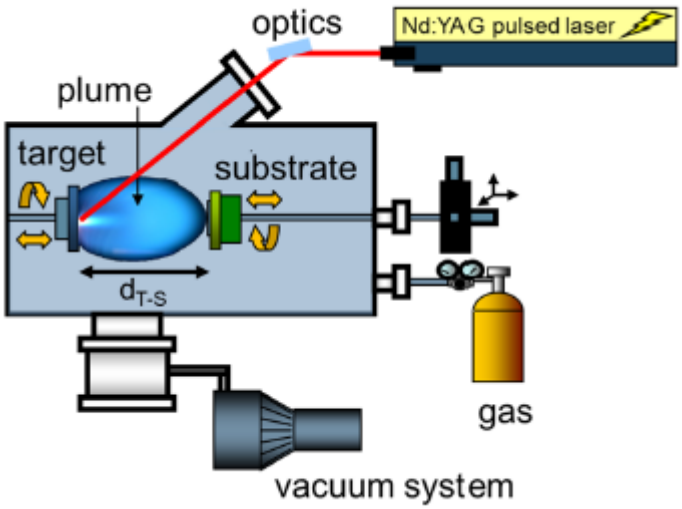

Figure 2.1: Scheme of a typical PLD system. Taken from [9].

Many process parameters can be tuned in order to control the morphology of the deposited film; the most important are background pressure, substrate temperature, target-to-substrate distance (d_{ts}), and laser fluence.

The presence of a background gas strongly influences the dynamics of plume propagation and the kinetic energy of the ablated species. Therefore, three different deposition regimes can be distinguished (see Fig. 2.2) :

1) When deposition is performed in vacuum (thus in absence of a background gas) , an atom-by-atom (or ion-by-ion) deposition is obtained. Since the propagation of the ablated species is almost collision-less, the expansion of the plume is highly forward-directed. Moreover, the plume shows a weak brightness and its species reach the substrate with a high kinetic energy. As a consequence, a compact film is obtained.

2) When deposition is performed with an inert background gas pressure, the high speed of the propagating species creates a compression region at the interface between gas and plasma that can lead to the creation of a shock wave. Therefore, the plasma plume is spatially confined by the background gas, favoring cluster nucleation in the gas phase. These clusters may diffuse in the background gas, hence reducing their kinetic energy. The deposition becomes less directional, and the fluorescence increases due to the radiative de-excitation produced by ablated species collisions both in the plume and, especially, at the expansion front. The plasma plume shows an hemispherical shape, where the maximum extension is greater along the transversal direction with respect to the longitudinal one. Consequently, the substrate is reached by low energy clusters which may partially maintain their structure and properties upon aggregation. Furthermore, the deposited film is characterized by a more or less porous and disordered structure, depending on the deposition pressure and on other process parameters.

3) When deposition is performed in the presence of a reactive background gas (e.g. oxygen or nitrogen), the clusters' composition is controlled via chemical interactions, so that a film with variable stoichiometry can be deposited.

.

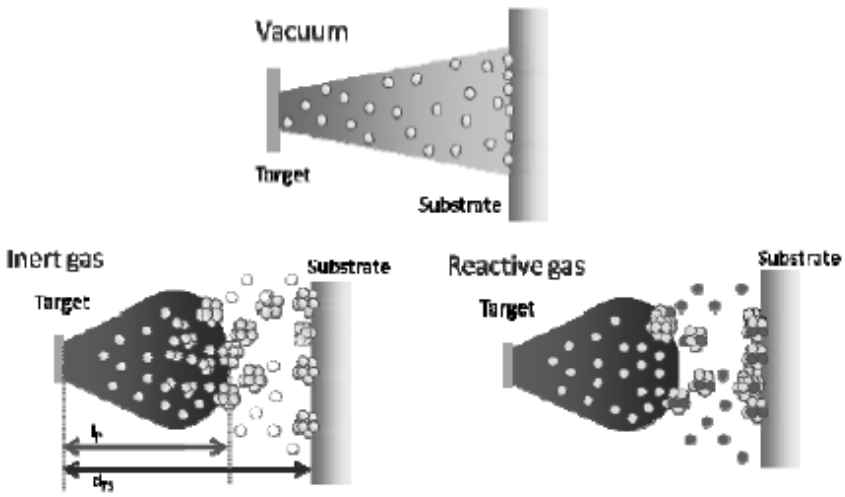

Figure 2.2: Three types of deposition atmosphere exist. Vacuum deposition results in highly energetic impinging particles, while a background gas will slow them down. Reactive deposition is preferred for compounds, while vacuum and inert deposition is used for metals. Taken from [88].

In the case of a well-defined shock front (P > 10 Pa), it is possible to introduce a non-dimensional characteristic length L, defined as the ratio between the target-to-substrate distance d_{ts} and the visible plume length l_p. This parameter L is a useful tool to control the deposition mechanism [89].
According to the L value, three different regimes can be distinguished:

- $L < 1$: the substrate is "contained" in the plasma plume. The ablated species have a high kinetic energy and are highly forward-directed towards the substrate. Cluster growth during expansion is limited. The result is a compact film with smooth surface.

- $L \sim 1$: the substrate position coincides with the plume edge, that is the maximum position of the shock front. The ablated species have a reduced kinetic energy due to the interaction with the surrounding gas. In this way, the deposition of vertically oriented porous films is allowed. In the case of oxides and nitrides, peculiar hierarchical nanostructures called "nanoforests" or "tree-like" nanostructured films can be obtained. These kind of architectures feature interesting properties like high porosity, high specific surface areas and light scattering [90].

- $L > 1$: the substrate is not "touched" by the plume. Cluster nucleation is favored, increasing the scattering with the background gas. The kinetic energy of the deposited species is always lower as L increases. In this condition, cluster-assembled nanostructured films are expected.

Moreover, it should be pointed out that the mass of the atoms/molecules constituting the background atmosphere affects the plume length l_p, which decreases as the mass increases. Another key parameter affecting the deposition rate is the laser fluence: by increasing the fluence, deposition rate increases as well as the plume length l_p.

Regarding the substrate temperature, when it is sufficiently high, atomic mobility is favored and the film tends to reorganize in more stable structures (crystals). Since in this work all films were deposited at room temperature, we tried to control the TiN films crystallinity by performing post-deposition annealing.

In this work, PLD was done with pulses in the nanosecond regime. Nanosecond pulses make the target ablation a thermal process, since they are longer than the typical time scale for energy transfer from the electrons to the crystal lattice (phonons) [91]. Thus a region greater than the irradiated one will be thermally affected. This usually results in a high deposition rate, but also in an intense incidence of droplets.

The ablation laser used in this work is a solid state Q-switched Nd:YAG laser providing pulses in the visible (second harmonic, 532 nm wavelength, 10 Hz repetition rate, pulse duration ~ 6 ns). All films were grown at room temperature on Si(100) and soda-lime glass by ablating a pure (99.9 %) TiN target with a diameter of 2 inches. The target-to-substrate distance was kept constant at $d_{ts} = 5\ cm$, while the fluence was varied between 2 and 6.5 J/cm^2. The films were deposited in vacuum and at background pressure of 5, 10, 20, 50, and 100 Pa (N_2/H_2).

2.1.1 RF ion source

Integrated into our deposition system, the RFMAX60 ion source generates beams of accelerated ions which can be used to modify and erode surfaces under vacuum conditions (maximum pressures of $p \sim 10^{-2} Pa$). By carefully selecting the energy and composition of the ion beam, the ion source can be used, for example, to improve the characteristics of a growing film both by increasing the film density and by modifying its chemical composition. Alternatively, ion beams can be used to erode existing films or sputter target material to project a plume of material for deposition on a substrate. In our work, RF ion source was used during compact TiN thin film deposition in order to furnish nitrogen species to the plasma plume. In other words, an ion beam-assisted deposition was performed. N_2/H_2 (95-5 %) was chosen as working gas.
Our RF ion source is designed for use in HV or UHV deposition systems. The source can generate ion beams from 50 eV up to 1000 eV and with beam currents between 10 mA and 150 mA. The relationship between RF power and beam current is close to linear. The ion source contains a helical coil wrapped around a ceramic discharge tube; RF power at 13.56 MHz is applied to this coil with a power between 100 and 600 W at the same time as a compatible gas (in our case, nitrogen) is introduced into the discharge tube through a mass flow controller. The RF field generates a plasma within the discharge tube, thus supplying the charged particles which form the basis of the ion beam. The discharge tube is enclosed by a pair of grids: the inner grid has an applied voltage which is equal to the selected energy of the ion beam; the outer grid is held at ground potential. The field gradient created by this potential difference draws ions from the plasma and through the holes in the outer grid. The multiple “beamlets” combine, forming one broad ion beam which emerges into the chamber. Operation at high RF power requires efficient water cooling to prevent overheating of the source components.

In the ion beam-assisted deposition performed in this work the forward power was set at 300 W and the applied voltage at 380 V, giving a current of 45 mA. The N_2/H_2 gas flow was fixed at 10 sccm.

2.2 Scanning Electron Microscopy

Scanning Electron Microscopy (SEM) is one of the most common microstructural characterization techniques. It allows to acquire images of any electrically conducting sample with a lateral resolution of the order of the nanometer, corresponding to both the diffraction constraints imposed by the scanning electrons and the dimension of the electron beam. The working principle of a SEM apparatus is shown in Fig. 2.3.
After having placed the samples into a chamber, the system is brought under high vacuum conditions ($p \sim 10^{-4}\ Pa$). The high vacuum ensures a smooth travel of the electron beam without it getting scattered due to any residual gas molecules.
Electrons are emitted from a field-emission electron gun. First, the electron beam is accelerated by a potential difference of 0.3-30 kV; then, it passes through an electromagnetic collimator to be deflected, hence generating the scan. Eventually, the beam is focused on the stage containing the sample to be analyzed. The beam is constantly guided by deflection coils and it scans the surface according to a raster pattern. Once the beam hits the material, a variety of signals are generated, but in this case *backscattered* and *secondary electrons* are exploited. *Backscattered electrons* are sensitive to crystal structure and orientation, and in particular allow to distinguish compact and a porous structures. *Secondary electrons* instead give a strong sense of depth and are used to understand the surface morphology of the film [92].
In this work a Field Emission Zeiss SEM SUPRA 40 based on a GEMINI column was used to obtain the top surface and cross section images of the samples.

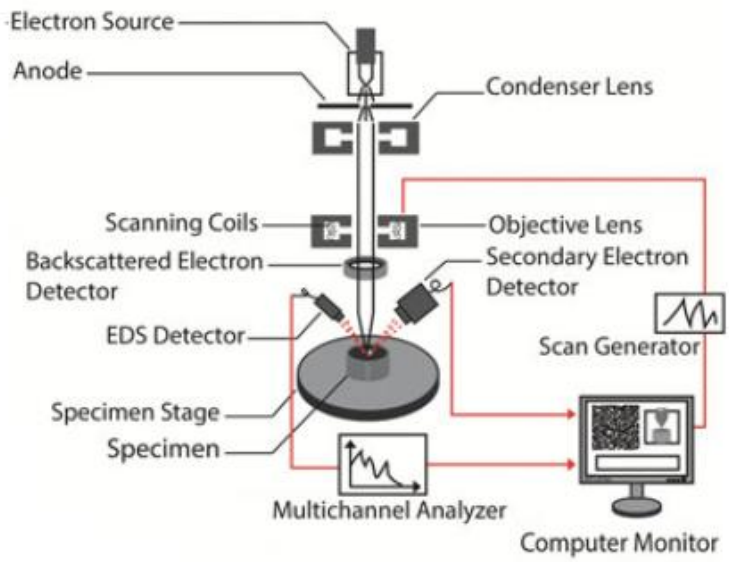

Figure 2.3: Schematic representation of SEM apparatus. Taken from [92].

2.3 Raman Spectroscopy

Raman spectroscopy is based on inelastic scattering of light by a molecule or a crystal: this means that scattered photons have a different energy with respect to the incident ones. When a photon hits a molecule, the overall system (composed by the photon and the molecule) gets excited to a "virtual" state (if the energy does not correspond to an electronic transition, which happens in the case of the so-called resonant Raman); then, three phenomena can happen, as it is described in Fig. 2.4:

1. Rayleigh scattering. The molecule remains in the same vibrational state as before the collision, meaning that radiation has been elastically scattered. It is the most frequent event, and gives a Raman intensity peak centered at the frequency of the laser. This signal is very intense and must be filtered out not to cover the "real" Raman effect.
2. Stokes scattering. The molecule goes to a higher energy level, while the scattered radiation has a greater wavelength. The energy difference has been transferred from the photon to the molecule. The energy exchange that brings the system back to the original state leads to the creation of vibrational energy, the Stokes scattering.
3. Anti-Stokes scattering. The molecule goes to a lower energy level, since it has ceded energy to the photon. Therefore, the frequency of the scattered light is greater than that of the incident one. The energy exchange that brings the system back to the original state leads to the annihilation of a phonon, the anti-Stokes scattering. Since the anti-Stokes process requires that a molecule is already in an excited vibrational state before the interaction with light, the intensity of the anti-Stokes peaks is always lower than the Stokes signal. Therefore, Raman spectroscopy exploits Stokes transitions.

Only those vibrations modes that produce a change in the molecule's or crystal's polarizability are Raman active. The entirety of this work, however, deals with crystalline and amorphous solids rather than molecules. Raman is particularly sensitive to the crystallinity of a sample, since different crystalline structures means different vibrational modes. The Raman spectrum of a crystal typically shows narrow peaks, which are associated to optical phonons at the center of the Brillouin zone, for reasons of conservation of energy and momentum. If we move to amorphous materials or confined nanostructures with a reduced crystal size, the uncertainty in the momentum (and so in the wavevector) increases, according to Heisenberg's uncertainty principle:

$$\Delta x \Delta p \geq \frac{\hbar}{2}$$

Where ħ is the reduced Planck constant. Due to the shape of the phonon dispersion relation, the Raman peaks are broadened and shifted, or even substituted by large bands.

A typical Raman apparatus, as shown in Fig. 2.5, is composed of a monochromatic coherent light (laser), an optical system to collect the scattered light, a diffraction grating (wave selector) and a detector.
In this work, all the Raman spectra were collected using a Renishaw InVia micro Raman spectrometer, equipped with an optical microscopy. An argon ion laser ($\lambda = 514\ nm$) was used as excitation source and the laser power was set at 1 mW, in order to avoid laser-induced modifications. The Raman spectra were collected in the 100-1000 cm^{-1} wavenumber range.

2.3.1 Raman Spectroscopy of TiN

Titanium nitride *fcc* rocksalt structure has in principle no first order Raman-active vibrations due to its O_h crystallographic symmetry. However, a Raman effect of first order is induced by the presence of defects and vacancies, which reduce the symmetry of the crystal. In other words, there is a relaxation of the Raman selection rule which imposes that the phonons involved in the Raman process are those at the center of the Brillouin zone ($q \cong 0$, where q is the phonons wavevector). The origin of TiN Raman spectrum is reflected in the fact that it is characterized by broad bands instead of sharp peaks. Therefore, a precise characterization of the material crystallinity on the basis of its Raman spectrum it is much more complicated than in the cases of materials with Raman active modes (e.g. TiO_2). This represents a big issue when investigating structural and compositional properties of TiN nanostructured thin films and nanoparticles, where the lack of extended crystalline domains and the great presence of amorphous phase makes the Raman signal associated to TiN even weaker and hard to be detected.

The disorder-allowed modes and second order scattering modes which can be observed (as reported in literature [31; 32]) are (see Fig.1.45):

- two low-frequency bands associated with scattering of acoustic phonons and positioned at ~ 210 cm^{-1} (Transverse Acoustic Mode) and ~ 310 cm^{-1} (Longitudinal Acoustic Mode). These are given by heavy Ti^{4+} ions vibrations due to N vacancies;
- one high-frequency broader band associated to scattering of optical phonons and positioned at ~ 510-540 cm^{-1} (Transverse Optical Mode). This is given by lighter N^{3-} ions vibrations due to Ti vacancies.
- One “shoulder” at ~ 440-450 cm^{-1} corresponding to second order scattering of the Transverse Acoustic Mode.

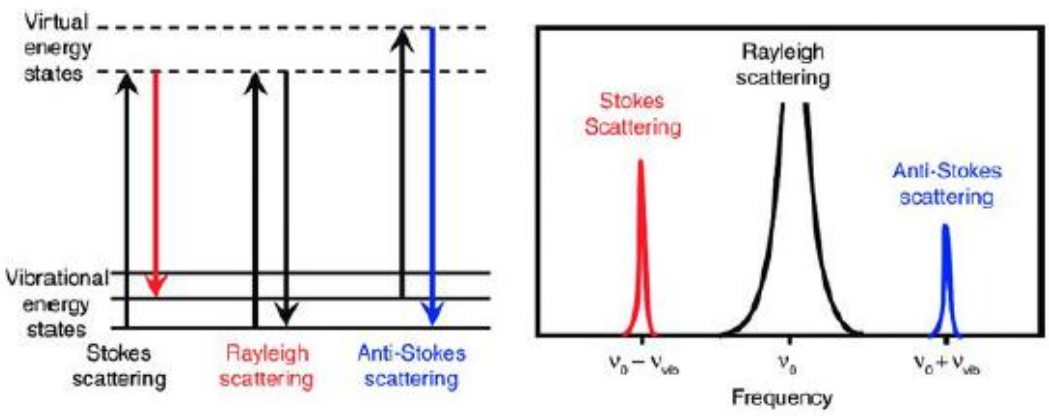

Figure 2.4: Stokes process gives scattered lights that are lower in energy than incident light, and anti-Stokes process gives scattered lights higher in energy than incident light. Taken from [93].

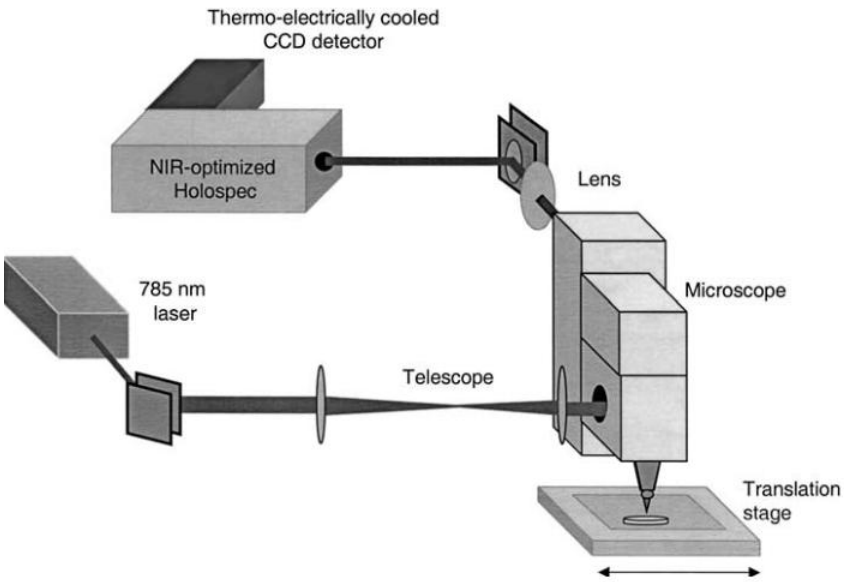

Figure 2.5: Schematic representation of Raman apparatus. Taken from [94].

2.4 UV-Vis-NIR Spectrophotometry

The optical measurements of the deposited TiN thin films have been performed at the Centre for Nanoscience and Technology (CNST) of the Italian Institute of Technology (IIT) in Milan using a LAMBDA 1050 UV/Vis/NIR spectrophotometer. A spectrophotometer is an instrument able to measure the intensity of light wavelength by wavelength. A monochromator produces a narrow light beam centered around a selected wavelength: the ratio of the beam intensity as it enters and leaves the sample is recorded thanks to a CCD detector, and a optical spectrum is obtained.

The LAMBDA 1050 system features a PMT, InGaAs and PbS 3-detector module for testing across the entire UV-Vis-NIR range. Moreover, it is equipped with a 150 mm Perkin Elmer snap-in integrating sphere, which manages to capture diffuse and specular reflectance.

When a film surface is hit by electromagnetic radiation, a portion of it will be transmitted, while another portion will be reflected. Then, as light travels across the whole thickness, some of it will be absorbed and some will be scattered. Adding together these contributions one should get the overall intensity as:

$$R + T + A + S = 1$$

To assess these quantities across a selected portion of the electromagnetic spectrum, a spectrophotometer can be used.
The scattered light is of a certain relevance when porous films are characterized.
In this work, the optical reflectance and transmittance (total and diffused) have been measured in the wavelength range between 250 and 2000 nm, with data interval of 2 nm. For this purpose, three different setups have been used, as shown in Fig. 2.6. In order to obtain the transmittance spectra, the sample (constituted by the TiN film deposited on glass substrate) was placed at the entrance of the integrating sphere, with the film facing the sphere. At the opposite side of the sphere, a hole is present; this can be left open or closed with a dedicated spectralon disk. If the disk is present, all the light passing through the sample is collected, thus the total transmittance is obtained. If instead the hole is left open, only the diffused transmittance is measured, since the radiation that passes through the sample without being diffused gets out of the integrating sphere through the aperture. The same hole was then closed by the sample itself (with the film facing the light beam) when the reflectance spectra were measured. All the recorded data have been normalized to the glass substrate contribution, to extrapolate the information related to the film. This was done by neglecting the interference phenomena brought by the glass substrate, according to the following relations:

$$T_{film} = \frac{T_{tot}}{T_{glass}}$$

$$R_{film} = R_{tot} - \left(R_{glass} \cdot T_{film}^2\right)$$

In addition, for nanoporous films, the haze factor was calculated as:

$$H = \frac{T_{diff}}{T_{tot}}$$

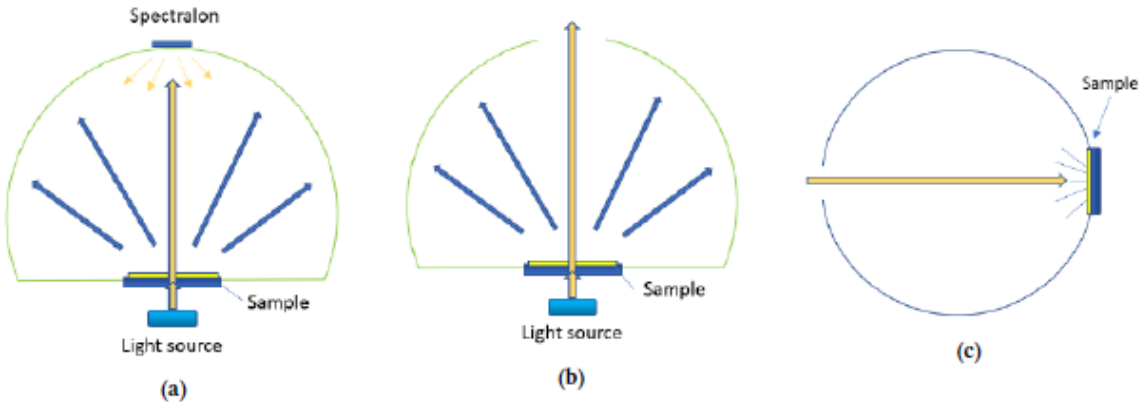

Figure 2.6: (a) Total transmittance, (b) diffused transmittance, and (c) reflectance measurements schemes. Taken from [95].

2.5 Thermal treatments

Thermal treatments were performed with a custom built furnace, capable of carrying on annealing treatments in a controlled atmosphere. The apparatus comprises a vacuum chamber, a heating system located inside the chamber and the vacuum system (see Fig. 2.7).

The samples are placed onto an alumina plate, in thermal contact with a Joule effect heating component. It is possible to flux gases such as argon or nitrogen into the chamber by manual mass flow control, thus changing the annealing atmosphere. Moreover, by controlling the heating ramp, it is possible to perform thermal treatments at different speeds. The vacuum system relies on an Edwards rotary pump, which acts as a primary pump, connected in series with a Varian Turbo-V 250 MacroTorr turbomolecular pumo. The heating system is run by Tectra HC3500 Heater Controller, and the temperature data are collected by an Impact IGA 120 pyrometer.

In this work, vacuum annealing treatments were performed at 550°C (reached with a smooth 10°C/min ramp) for 1 hr , after having evacuated the chamber to ~ 10^{-4} Pa. Furthermore, overpressured annealing treatments were done by fluxing N_2-H_2 (95-5%) gas until a 1050 mbar pressure was reached, after a previous evacuation of the chamber to ~ 10^{-4} Pa. Here, the temperatures selected were 550 and 300°C, while the annealing time and the heating ramp were still set at 1 hr and 10°C/min, respectively. The choice of adopting also a lower treatment temperature (300°C) was done in order to try to reduce oxidation of the largely amorphous nanostructured TiN films, while promoting at the same time their crystallization and nitrogen incorporation.

Figure 2.7: Schematic representation of the thermal treatments apparatus used in this work. Taken from [96].

2.6 Van der Pauw method (four-point probe)

The most widespread method for the electrical characterization of thin films is the four-point probe method proposed by Van der Pauw in 1958. Supposing to have a continuous (with no holes) thin film of uniform thickness, independently of the sample's shape it is possible to obtain and calculate its electrical properties. Four contacts of negligible size and resistance are placed onto the sample, and an impressed current flows between two of the four electrodes. The voltage drop between the two other electrodes is measured. This procedure is carried out for the four pairs of adjacent contacts, and then repeated inverting the current direction, for a total of eight configurations. Since the current is at a fixed known value, the degrees of freedom in each configuration are limited. Therefore, the average resistances values of two sides of the sample can be evaluated and, using the Van der Pauw's equation, the sheet resistance and, afterwards (by knowing the film thickness), the resistivity are easily obtained [97]. Using the same setup it is also possible to measure the carrier type, concentration and mobility, by exploiting the Hall effect. The voltage created by the charge separation induced by an applied magnetic field is the *Hall voltage*. This is inversely proportional to the carrier density. The sign of the voltage reveals if the carriers are either holes or electrons. Carrier mobility can be calculated from the carrier density. The measurements are performed the same way as the resistivity ones, except "cross" configurations are used instead of parallel ones. By setting a current (in both directions) across opposite electrodes, four configurations are obtained. Since the magnetic field can be inverted too, a total of eight configurations can be reached. Besides, in order to separate the naturally arising voltage contribution of flowing currents from the Lorentz-induced Hall voltage, zero-magnetic field measurements are performed as well. The apparatus used in this work comprises a Keithley 2400 SourceMeter, used as a current source, and a Keysight 34972A LXI Data acquisition unit controlled remotely with a computer, to log the voltage measurements. A custom built switch allowed to progressively select every required electrical configuration. Five pieces of data were collected for each configuration and then averaged before proceeding with the calculations, which were performed by an ad-hoc made Matlab code. Hall measurements were performed using a 0.57 T permanent magnet. In order to obtain an error bar, each sample was characterized three times.

Optimization of deposition parameters for nanostructured TiN thin films and strategies for oxidation reduction

In this chapter, different combinations of laser fluence and background pressure were tested in order to investigate the different TiN films morphologies obtainable by pulsed laser deposition. In particular, the transition from compact to tree-like nanostructured thin films was analyzed in terms of structural, compositional and optical properties.
Our aim was to obtain samples with the best possible TiN film stoichiometry; however, we found ourselves dealing with critical problems of oxidation, due to the extremely high surface area of the fabricated nanostructured and nanoporous films. For this reason, different strategies were adopted in order to reduce oxidation and thus manage to obtain TiN nanostructured films.
For all the films, optical properties in the UV/Vis/NIR range were investigated, as well as structural and compositional features.

3.1 Growth of nanostructured TiN thin films by PLD

All the TiN films in this first part of the work have been produced by PLD using a pure (99.9%) TiN target with diameter of 2 inches, located at 5 cm from the substrate stage. The ablation laser used for all the samples of this work is a solid state Q-switched Nd:YAG laser providing pulses in the visible (second harmonic, 532 nm wavelength, 10 Hz repetition rate, pulse duration ~ 6 ns). Two types of substrates were used: Si(100) and glass. The deposition atmosphere consisted in N_2-H_2 (95-5 %) gas at different pressures. The substrate was kept at room temperature during deposition.

At the beginning of this work thesis, different combinations of laser fluence and background deposition pressures were examined, as summarized in Tab. 3.1. The samples will be referred to with the denomination indicated in the table. The energy density and background pressure values were chosen on the basis of literature and of the work previously carried on by our group in this laboratory (see section 1.2). Besides, the study done by our research group in collaboration with ORNL (the Oak Ridge National Laboratory) was considered a further starting point.

Background pressures of 5, 10, 20, 50 and 100 Pa were chosen in order to investigate the different thin films morphologies obtainable by PLD. In fact, it is known from researches made on PLD deposition of other materials (e.g. titanium dioxide [10]) that increasing the background pressure can lead to a morphological transition from compact to tree-like nanostructured thin films, and ultimately to foam-like structures. However, only one group [87] investigated this effect for TiN thin films; from this work, it is clear that (considering a fluence $f = 3.5\,J/cm^2$) N_2-H_2 (95-5 %) background pressures p from 5 to 10 Pa are sufficient to decrease a lot the film density (see Fig. 1.40) , while pressures $p > 30\,Pa$ induce a tree-like nanostructured morphology with increasing pores' volume and size. In addition, based on the previous work carried on in this laboratory (where a maximum N_2-H_2 (95-5 %) background pressure of 10 Pa was used) our intention was to extend the operating conditions range by investigating higher deposition pressures. In this way, the abovementioned transition from compact to tree-like thin film structure can be investigated.

Fluence values (f) of 2 and 3.5 J/cm^2 have been obtained with a laser pulse energy of 120 and 210 mJ (respectively), considering that the ablation spot size S was approximately equal to 6 mm^2. It is important to note that, together with a slower deposition rate, lower energy densities lead to smaller kinetic energy of the ablated species, thus favoring the formation of less compact films. So, since the objective was to produce nanoporous films, we decided to investigate also $f = 2\,J/cm^2$, a lower fluence with respect to $f = 3.5\,J/cm^2$ (which was taken as a reference value, based on previous works on TiN films by PLD). It is worth mentioning that the evacuation of the chamber to $\sim 4 - 5 \cdot 10^{-3}\,Pa$ before deposition was needed in order to limit the contamination from residual oxygen.

	5 Pa	**10 Pa**	**20 Pa**	**50 Pa**	**100 Pa**
2 J/cm^2	TiN_P5_F2	TiN_P10_F2	TiN_P20_F2	TiN_P50_F2	TiN_P100_F2
3.5 J/cm^2	TiN_P5_F3.5	TiN_P10_F3.5	TiN_P20_F3.5	TiN_P50_F3.5	TiN_P100_F3.5

Table 3.1: Summary of the examined combinations of laser fluence and N_2-H_2 deposition pressure, and denomination of the grown films.

We decided to set the deposition time at 30 minutes for all the samples reported in Tab. 3.1. This was easier to do rather than adjusting the deposition time to have films with comparable thickness. In that way, the deposition times for the more compact films would indeed have been too long.

All samples listed in Tab.3.1 and deposited on Si have been cross-sectioned and analyzed using the SEM apparatus described in section 2.2. SEM images were also used in order to

evaluate the thicknesses of the films. Fig. 3.1 shows the cross sections of films deposited at $f = 2\,J/cm^2$. It is clear that, with increasing background pressure, the morphology of the films goes from almost compact (sample TiN_P5_F2 and TiN_P10_F2) to porous tree-like (sample TiN_P20_F2 and TiN_P50_F2) and, eventually, to foam-like (sample TiN_P100_F2), due to in plume clusterization (as described in section 2.1). Fig. 3.2 shows the cross sections of films deposited at $f = 3.5\,J/cm^2$. Also in this case higher background pressures lead to the aforesaid morphological transition; however, such transition is shifted towards higher pressures with respect to the case of $f = 2\,J/cm^2$, since greater laser energy values favor the formation of more compact structures. Fig. 3.1 and 3.2 also show the top-view images of samples deposited at 2 and 3.5 J/cm^2, respectively. It can be observed the transition (with increasing p) from a smooth and compact surface to a rough and nanostructured one, until an extremely open surface with high specific surface area starts to appear.

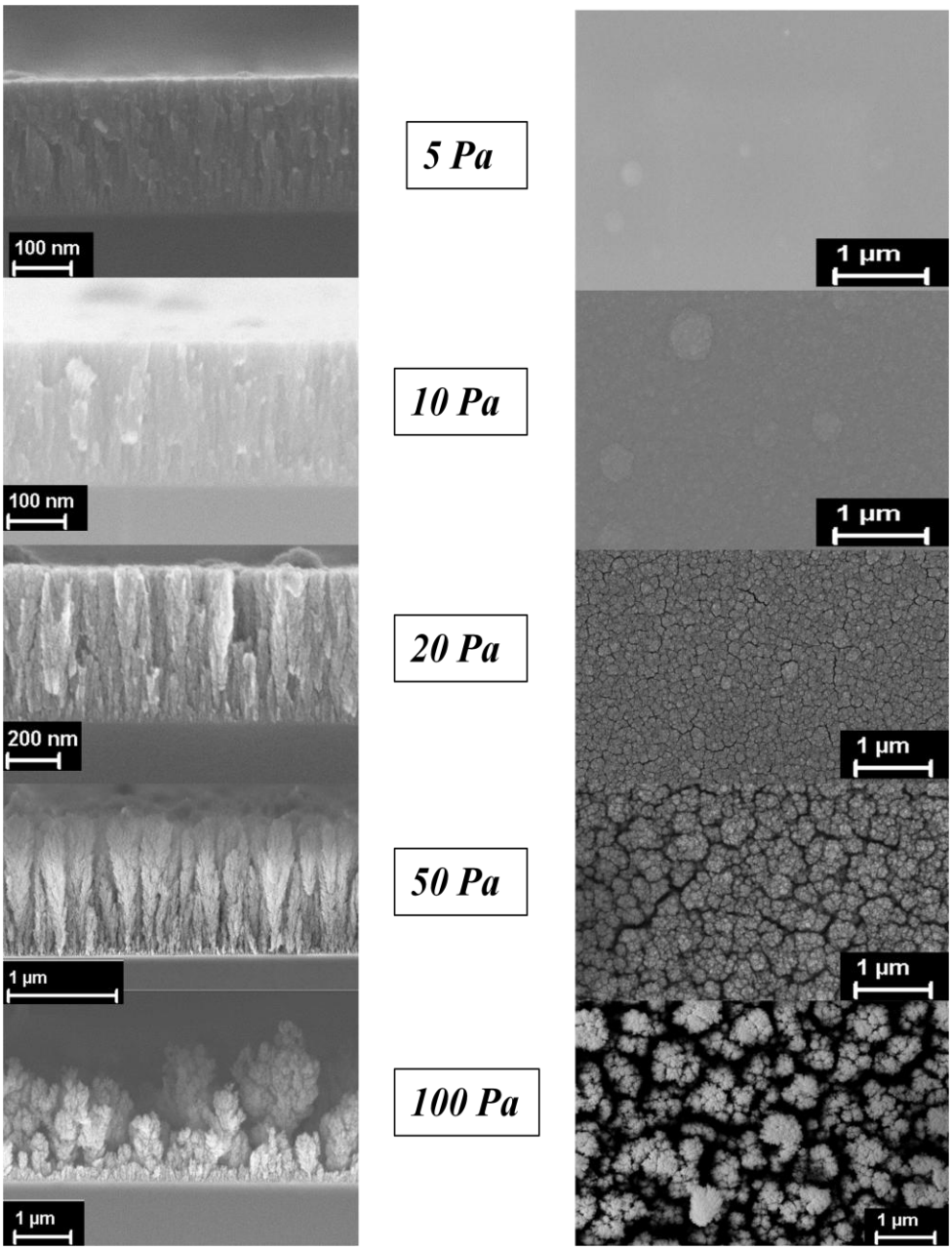

Figure 3.1: SEM images of (left) cross sections and (right) top-view surface of samples TiN_P5_F2, TiN_P10_F2, TiN_P20_F2, TiN_P50_F2, and TiN_P100_F2.

.

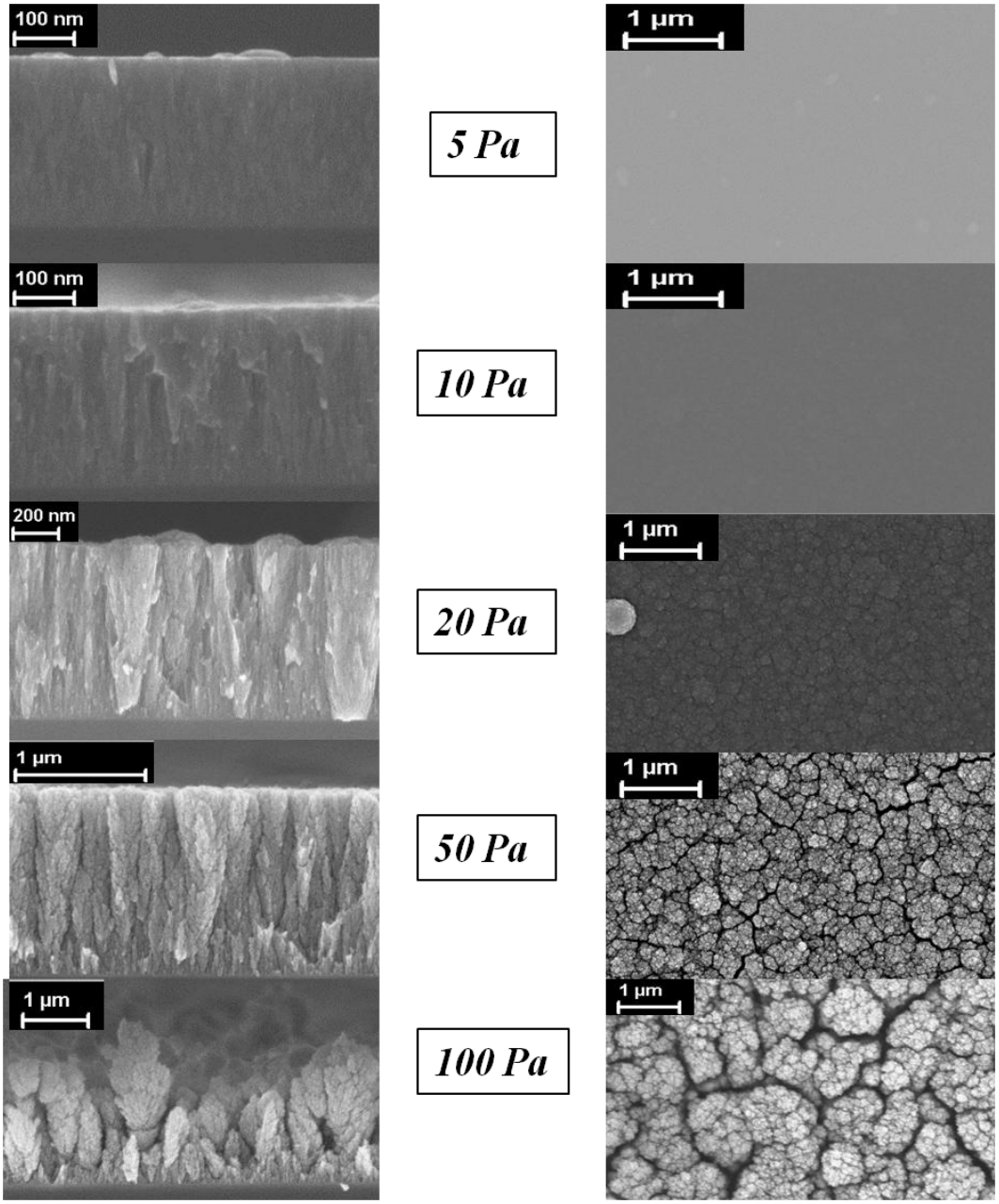

Figure 3.2: SEM images of (left) cross sections and (right) top-view surface of samples TiN_P5_F3.5, TiN_P10_F3.5, TiN_P20_F3.5, TiN_P50_F3.5, and TiN_P100_F3.5.

In order to estimate the density values of the obtained films, microbalance measurements were performed. A quartz crystal microbalance (QCM) was manually put in front of the target, at a distance equal to 5 cm (equal to the distance adopted during all the depositions). This device measures the density of mass (m_A) deposited at the various fluence and pressure conditions. Then, by fixing the density at a value equal to 1 g/cm^3 so that $m_A = 10\ ng/cm^2$ corresponds to an equivalent thickness of 1 Å, the device converts the mass deposited per unit area (m_A) into a deposition rate (d_r), expressed as the thickness that a

equivalent film with density $\rho = 1\ g/cm^3$ would have if deposited with 1000 laser shots ($K\text{Å}/1000\ shots$). Consequently, the equivalent thickness b_{eq} of a film with density $\rho = 1\ g/cm^3$ but deposited with a laser shot frequency (ν) of 10 Hz and for a time (t) of 30 min could be calculated as following:

$$b_{eq}(K\text{Å}) = \frac{d_r \cdot \nu \cdot t}{1000} = \frac{d_r(K\text{Å}/1000\ shots) \cdot 10(Hz) \cdot 30 \cdot 60(s)}{1000(shots)}$$

However, during the effective film depositions the substrate was not put exactly in front of the target (like it happened during QCM measurements) but it was slightly offset with respect to it. Such offset substrate position was optimized for every deposition conditions, in order to obtain the most uniform film thickness possible all over the substrate. On the other side, this offset implied a lower quantity of material directly depositing on the substrate. Therefore, in order to consider the fact that the QCM measures overestimated the quantity of material deposited per unit area, the calculated m_A values were reduced by a corrective factor CF, so that the final density value was obtained from the following formula:

$$\rho = \frac{m_A}{CF} \cdot \frac{1}{b}$$

where b is the film thickness measured from SEM cross-section images. In order to calculate CF values for the various offset configurations, an assumption was made. The deposition condition consisting in $f = 3.5\ J/cm^2$ and vacuum atmosphere (where an offset of 7 mm was adopted in order to obtain an uniform film) was considered to produce compact films with a density equal to the bulk TiN one (i.e. $\rho = 5.24\ g/cm^3$). Hence, the corrective factor related to this case was evaluated from:

$$CF = \frac{m_A}{\rho} \cdot \frac{1}{b}$$

where ρ was set equal to $5.24\ g/cm^3$. $CF = 2.74$ was found. Consequently, the CF related to the other offsets (i.e. 5 mm and 10 mm) were easily calculated by the use of simple proportions. All the results obtained at every calculation step are reported in Tab. 3.2 and Tab. 3.3.

Sample	d_r (KÅ/1000 shots)	b_{eq}(KÅ)	m_A ($\mu g/cm^2$)	Offset (mm)	CF	$b(nm)$	ρ (g/cm^3)
TiN_P5_F2	1.50	27.00	270.00	7	2.74	300	3.29
TiN_P10_F2	1.15	20.74	207.36	7	2.74	320	2.37
TiN_P20_F2	1.26	22.61	226.08	10	3.10	540	1.35
TiN_P50_F2	0.83	14.99	149.94	10	3.10	1170	0.41
TiN_P100_F2	0.61	11.03	110.34	10	3.10	3250	0.11

Table 3.2: Summary of calculation steps adopted in order to evaluate the densities of samples TiN_P5_F2, TiN_P10_F2, TiN_P20_F2, TiN_P50_F2, and TiN_P100_F2 based on QCM measurements.

Sample	d_r (KÅ/1000 shots)	b_{eq}(KÅ)	m_A ($\mu g/cm^2$)	Offset (mm)	CF	$b(nm)$	ρ (g/cm^3)
TiN_P5_F3.5	2.82	50.69	506.88	5	2.38	545	3.91
TiN_P10_F3.5	2.71	48.83	488.34	5	2.38	625	3.29
TiN_P20_F3.5	2.605	46.89	468.90	5	2.38	950	2.08
TiN_P50_F3.5	2.12	38.07	380.70	10	3.10	1350	0.91
TiN_P100_F3.5	1.59	28.58	285.84	10	3.10	2900	0.32

Table 3.3: Summary of calculation steps adopted in order to evaluate the densities of samples TiN_P5_F3.5, TiN_P10_F3.5, TiN_P20_F3.5, TiN_P50_F3.5 and TiN_P100_F3.5 based on QCM measurements.

In Fig. 3.3 the estimated density values are plotted as a function of the different background pressures for the two laser fluences adopted. It can be seen how a higher laser pulse energy leads to more compact films, but the density difference stays relatively small and almost constant for all the investigated background pressures. Moreover, the density values obtained at $f = 3.5\, J/cm^2$ are similar to those obtained by Perego et al. [87] at the same pressure and fluence conditions (see Fig 1.40 for comparison). In general, we can say that highly porous thin films with significantly low densities have been fabricated.

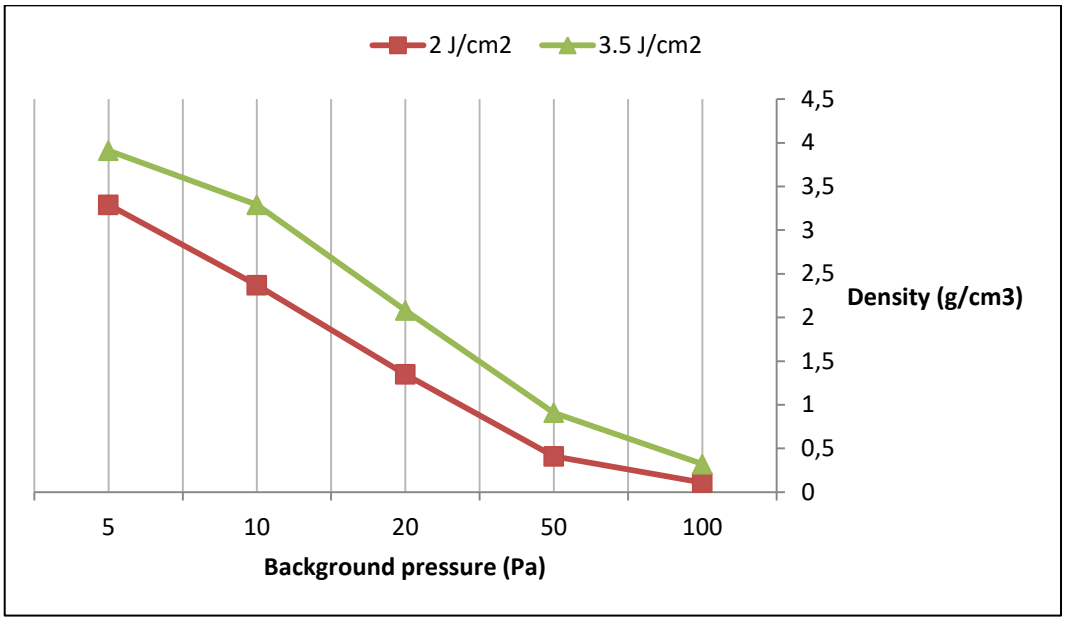

Figure 3.3: Density dependency on the operating pressure for films obtained at laser fluences (red line) 2 J/cm^2 and (green line) 3.5 J/cm^2.

In the following, the results obtained from Raman spectroscopy will be illustrated. For all the measurements, the highest peak has been normalized to 1 so as to make them comparable to each other. Only Raman spectra of films deposited on a glass substrate will be reported. In fact, the weak signal given by nanoporous films resulted to get always covered by the strong signal given by the silicon substrate.

Fig. 3.4 displays the Raman spectra of the samples deposited with $f = 2\,J/cm^2$ and $3.5\,J/cm^2$, at those operating pressures where a neat change in the spectrum is identified. For instance, Fig. 3.4a shows that, at $f = 2\,J/cm^2$, by increasing the pressure from 5 to 10 Pa the Raman spectrum clearly goes from the typical one of amorphous TiO_2 (see Fig. 3.5) to one with features associable to sub-stoichiometric TiN (i.e. very low signal around 500-600 cm^{-1}, as discussed in section 2.2). The Raman spectra of the samples TiN_P20_F2, TiN_P50_F2 and TiN_P100_F2 are not reported here, since they are practically identical to those of sample TiN_P10_F2. The films deposited above a certain pressure are constituted by a considerably lower amount of material (see Tab.3.2 and Tab.3.3), hence giving a much weaker Raman signal. Moreover, it is likely that the more porous films have such an amorphous structure that the defect-induced first order Raman scattering typical of B1-TiN is too weak, and gets completely overcome by the stronger TiO_2 signal. In addition, it is reasonable to expect that the more porous films are characterized by a higher oxidation extent, considering their greater specific surface area.

For $f = 3.5\,J/cm^2$ (Fig. 3.4b), only the spectra relative to samples TiN_P5_F3.5, TiN_P10_F3.5 and TiN_P20_F3.5 have been illustrated, considering that TiN_P50_F3.5 and TiN_P100_F3.5 ones were very similar to those of sample TiN_P10_F2. It can be observed that an increase in N_2-H_2 background pressure from 5 to 20 Pa leads to a blue-

shift of the acoustic band, between 200 and 300 cm^{-1}, and to a strong increase of the 500-600 cm^{-1} band intensity. The latter intensity increase could be associated to a higher nitrogen content within the sample, due to a higher exposure to nitrogen (i.e. higher background pressure), but it may be also due to the higher signal coming from oxide and oxynitride phases.

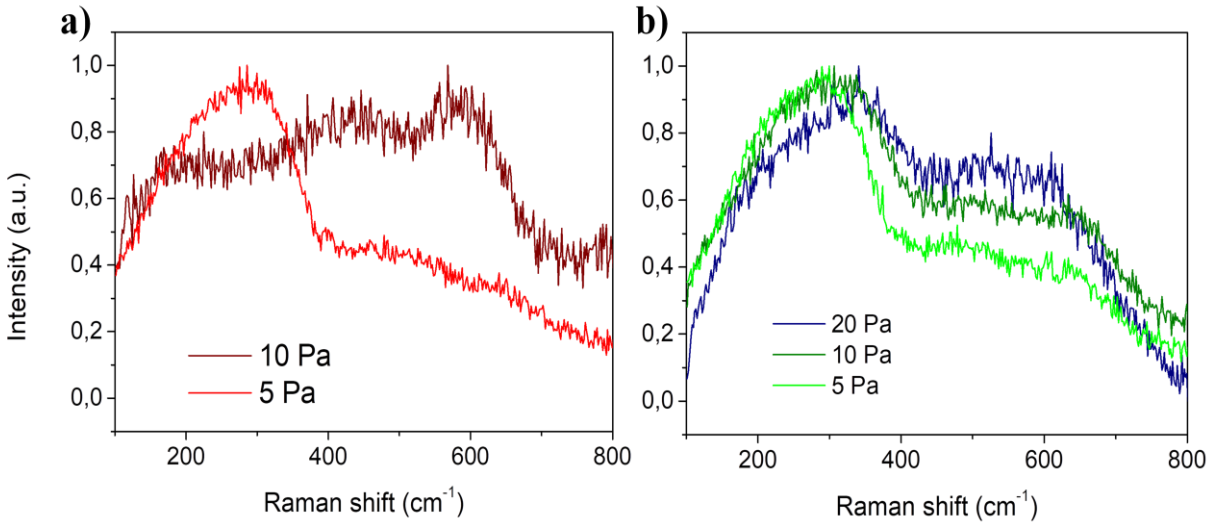

Figure 3.4: Raman spectra of TiN thin films deposited at : (a) f = 2 J/cm^2, P = 5, 10 Pa; (b) f = 3.5 J/cm^2, P = 5, 10, 20 Pa.

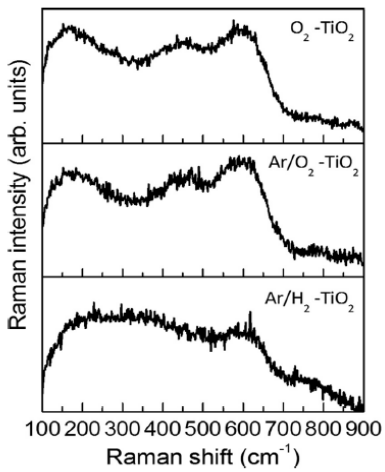

Figure 3.5: Raman spectra of amorphous TiO_2 obtained by PLD using different gas atmospheres. Taken from [10].

Finally, the optical properties of the samples were analyzed after UV-Vis-NIR spectrophotometer measurements were performed (as described in section 2.4). In Fig. 3.6 the absorption, reflectance and transmittance spectra of samples TiN_P5_F2 and TiN_P10_F2 (whose Raman spectra are shown in Fig. 3.4a) are illustrated. Accordingly to Raman analysis, sample TiN_P10_F2 shows optical properties which are very similar to those of amorphous titanium oxide: very high transparency and low absorbance and reflectance for energies below the energy gap. The energy gap of sample TiN_P10_F2 has been calculated by Tauc plot analysis to be $E_g = 3.44\ eV$ (i.e. $\lambda = 360\ nm$) and $E_g = 3.13\ eV$ (i.e. $\lambda = 396\ nm$), respectively for direct and indirect transitions. In Fig. 3.7 the direct and indirect band gap linear extrapolation is shown. The E_g for indirect transitions is comparable to the typical values for anatase ($E_g = 3.23\ eV$). In particular, an energy gap $E_g \approx 3.13\ eV$ has been associated in literature to an anatase phase $TiO_{2-x}N_x$ with some nitrogen incorporated ($\approx 8\ at\%$) [98]. Analogously to Raman spectra representation, the optical spectra of samples TiN_P20_F2, TiN_P50_F2, and TiN_P100_F2 have not been reported since they were similar to those of sample TiN_P10_F2. Sample TiN_P5_F2 shows a neat absorption peak which corresponds to the minimum of the reflectance, that in literature is associated with the plasma frequency [99, 100]. Besides, sample TiN_P5_F2's transmittance curve tends to zero for all the measured wavelength interval. By polynomial fitting of the optical curves, a reflectance minimum of ~ 15.5 % and an absorbance maximum of ~ 84 % located at $\lambda = 462\ nm$ were obtained. Moreover, a steep plasma reflectance edge that brings R to a *plateau* value around 60% is observed.

Considering now the samples deposited at $f = 3.5\ J/cm^2$, their color changes from reddish-brown (sample TiN_P5_F3.5) to dark-blue (sample TiN_P10_F3.5) to black/dark-green (sample TiN_P20_F3.5), suggesting a completely different structure and composition (see Fig. 3.9).

Regarding these samples optical properties, from Fig. 3.8 the following observations can be made:

- Increasing the N_2-H_2 background pressure from 5 to 10 Pa leads to the formation of a transmittance peak around 480 nm. At N_2-H_2 20 Pa such transmittance peak raises in intensity and gets red-shifted to wavelengths around 550 nm (Fig. 3.8b). As discussed in section 1.2, this behavior is found to be due to a higher oxygen incorporation within the TiN crystal lattice, forming TiO_xN_y [29].

- The reflectance decreases with increasing N_2-H_2 background pressure. In particular, at 10 Pa the reflectance edge typical of compact TiN thin films gets less steep, until it disappears at 20 Pa (Fig. 3.8c).

- The absorbance increases with increasing N_2-H_2 background pressure. Moreover, the qualitative behavior of the absorption spectra clearly changes. At 5 Pa there is a well defined and narrow peak, whose location can be estimated at $\lambda = 472\ nm$ by polynomial fitting of the curve. At 10 Pa the appearance of another, smaller peak

at shorter wavelengths can be observed, while the "main" peak at longer wavelengths gets broader and red-shifted to $\lambda = 612\ nm$. Finally, at 20 Pa the contribution at shorter wavelength becomes much more visible, so that two absorbance maxima can be seen; at the same time the "main" peak extends to a wide range of wavelengths, and it is centered at $\lambda \approx 791\ nm$.

The features observed in these absorption spectra could be associated to intra-band (peak at longer $\lambda's$) and inter-band (peak at shorter $\lambda's$) transitions.

For compact TiN films the contribution given by intra-band transitions lays in the same wavelength interval of the other one, and it is much stronger. For this reason, in compact TiN films the inter-band absorption peak is not visible (as reported in literature [21, 22]). On the other hand, for TiN NPs the contribution of inter-band transitions at shorter wavelengths can always be observed, and has a higher intensity with respect to the LSPR peak located al longer wavelength. This is due to the fact that the LSPR peak in TiN NPs on one side has a weak intensity (mainly because of oxidation) and on the other side is well separated in wavelength from the inter-band contribution (as discussed in section 1.3). Therefore, it may be hypothesized that for nanostructured TiN films constituted by NPs assemblies we observe a qualitative behavior in the middle between the two aforesaid ones: the intra-band and inter-band contributions have similar intensity, and are located in a nearby spectral region. The more porous and nanostructured is the film, the more the intra-band absorbance peak red-shifts and the contribute given by inter-band transitions starts to be visible.

This optical behavior as a function of N_2-H_2 operating pressure can be associated to the variation of free electron concentration and to the change in morphology. In particular, by increasing *p*, the nitrogen content increases (as Raman spectra in Fig 3.4b may suggest) and thus the number of free electrons in the film is expected to reduce. However, without any data on carrier density and stoichiometry, the following discussion is an interpretative hypothesis that should be verified. As a consequence of the assumed lower charge carrier density, not only fewer electrons interact with the incident radiation hence reducing the reflected light (Fig 3.8c), but also the plasma frequency is decreased hence red-shifting the intra-band absorption peak (Fig. 3.8a). Furthermore, the increasing nanoporosity given by higher *p* favors oxygen incorporation within the sample (as Raman spectra in Fig. 3.4b may also suggest); also this may induce a lower free electron concentration.

It should be specified that, analogously to Raman spectra representation, the optical spectra of samples TiN_P50_F3.5 and TiN_P100_F3.5 have not been reported since they were similar to those of sample TiN_P10_F2.

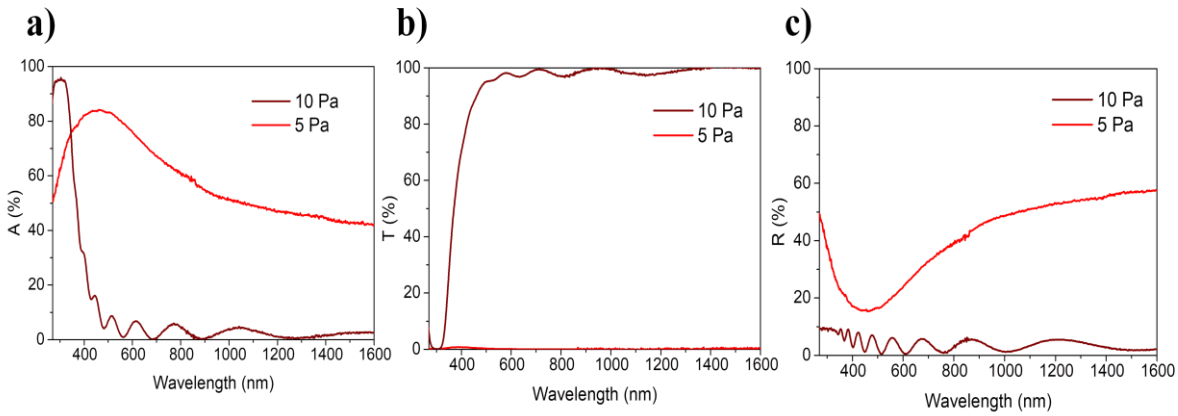

Figure 3.6: (a) Absorbance, (b) transmittance and (c) reflectance of samples TiN_P5_F2 (5 Pa) and TiN_P10_F2 (10 Pa), deposited at f = 2 J/cm^2

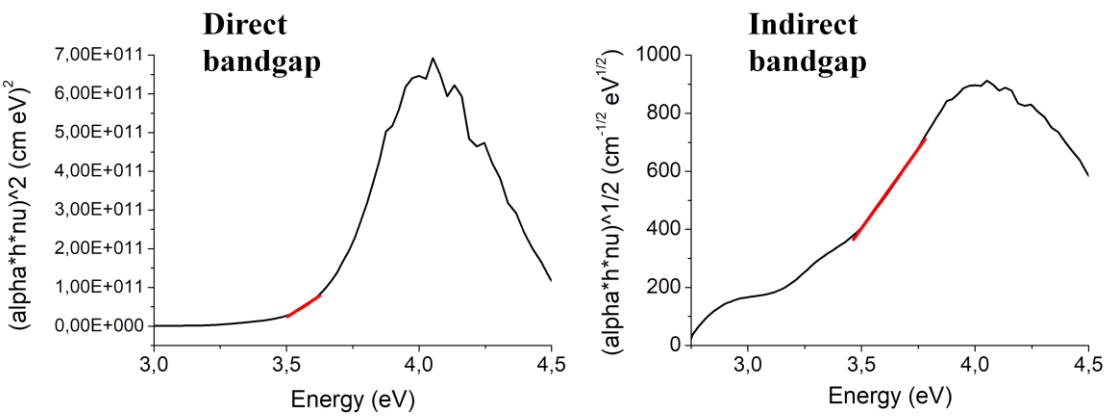

Figure 3.7: Direct and indirect band gap extrapolation through Tauc plot analysis for sample TiN_P10_F2.

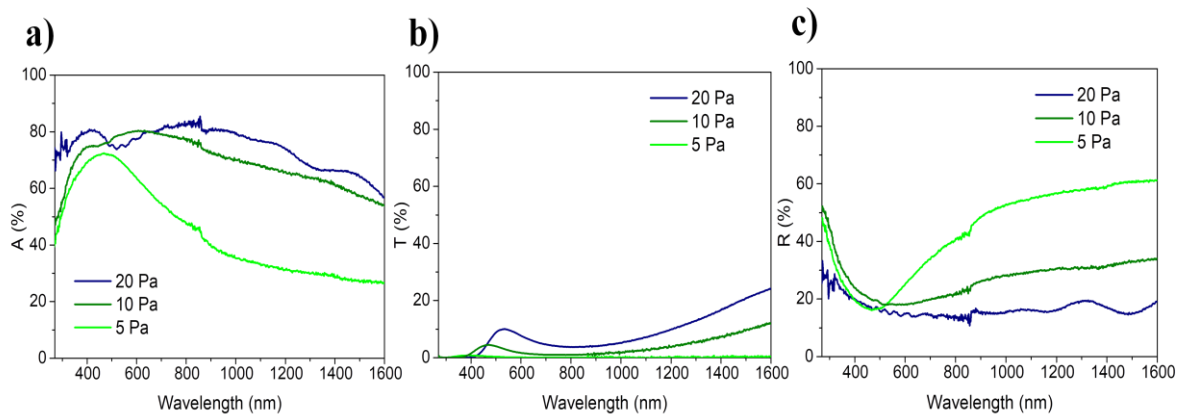

Figure 3.8: (a) Absorbance, (b) transmittance and (c) reflectance of samples TiN_P5_F3.5, TiN_P10_F3.5 and TiN_P20_F3.5, deposited at f = 3.5 J/cm^2.

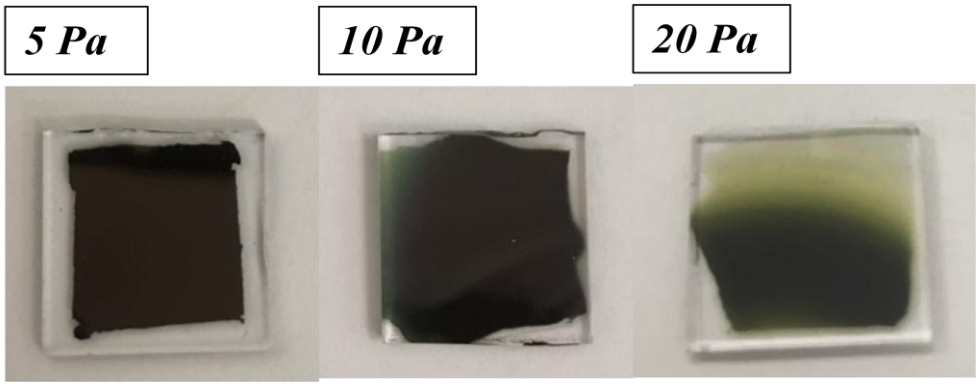

Figure 3.9: TiN_P5_F3.5, TiN_P10_F3.5 and TiN_P20_F3.5 samples (from left to right, respectively).

This study on the effect of pressure and fluence allowed us to obtain information on the morphology, qualitative composition and optical properties of the TiN films. In particular, keeping a constant fluence, it is possible, by increasing the pressure from 5 to 100 Pa, to move from compact-columnar to tree-like nanostructured films, and eventually to foams. On the other hand, at constant pressure, a higher laser energy density leads to a more compact structure. Moreover, pressure plays an important role in modifying the film composition, since higher p seem to favor nitrogen incorporation . The effect of fluence on film composition needs further investigation; by now, the only thing that can be affirmed is that a higher fluence allowed us to have thin films showing characteristics of TiN (or at least of TiO_xN_y) rather than of amorphous TiO_2 with lower density values. In fact, the most porous films deposited at $f = 2\,J/cm^2$ that shows Raman spectrum and optical curves that can be related to TiN (or to TiO_xN_y) is the sample TiN_P5_F2, with a density value $3.29\,g/cm^3$; while for $f = 3.5\,J/cm^2$ it is sample TiN_P20_F3.5, with $\rho = 2.08\,g/cm^3$.

3.2 Strategies for oxidation reduction

In general, all the samples analyzed by now seem to be either amorphous titanium oxide (samples TiN_P10_F2, TiN_P20_F2, TiN_P50_F2, TiN_P100_F2, TiN_P50_F3.5, TiN_P100_F3.5) or sub-stoichiometric titanium nitride (samples TiN_P5_F2 and TiN_P5_F3.5) or titanium oxynitride (samples TiN_P10_F3.5 and TiN_P20_F3.5). In order to reduce the oxygen incorporation in the abovementioned samples, thus extending the density-range in which titanium nitride films are formed, some strategies have been adopted. This was done considering that the oxidation of the deposited films can be mainly due to two factors:

1) Oxidation during deposition due to the poor vacuum environment or impurities in the background gas.

2) Oxidation of the film surface after deposition, due to air exposure.

3.2.1 Oxidation during deposition

One possible cause of oxidation during deposition is the poor vacuum environment in the chamber; for this reason, an evacuation to vacuum pressures $p < 5 \cdot 10^{-3}\ Pa$ has been done previous to every sample deposition.
Another possible cause of oxidation is the presence of impurities in the background gas. Especially for $p > 7\ Pa$ the impurities effect can be impactful [50, 101]. In fact, while sample TiN_P5_F2 (deposited at 5 Pa) is likely to be a sub-stoichiometric TiN with an absorption peak in the visible, sample TiN_P10_F2 (deposited at 10 Pa) is an amorphous, transparent titanium oxide. However, this could simply be due to the higher porosity of sample TiN_P10_F2, which makes it more prone to oxidation with respect to sample TiN_P5_F2. Considering instead sample TiN_P20_F3.5 (deposited at 20 Pa and at higher fluence), it can be observed that, despite its lower density and its higher deposition pressure (hence higher oxygen impurities) with respect to sample TiN_P10_F2, it presents features of TiN (or TiO_xN_y). So, for the same film density and morphology, using higher laser energy densities seem to be more efficient in reducing oxidation than reducing the background gas pressure and consequently its impurities. Possibly, higher laser fluences enhance the nitrogen species reactivity in the plasma plume, since the N_2 gas molecules gets more excited. In this way, the nitrogen incorporation may be favored above oxygen coming from either gas impurities or residual contamination in the chamber. Similar hypothesis were made in various literature papers [52, 53, 81]. It should be pointed out that the higher nitrogen incorporation promoted by higher laser fluences may also contribute to the reduction of air-exposure oxidation, because less surface N vacancies would be there to be filled by oxygen. However, in order to understand more precisely whether during or post-deposition oxidation is more reduced by raising the laser energy density, other measurements like *in-situ* Raman Spectroscopy should be performed.
Since in the aforesaid papers fluences of 5-7 J/cm^2 and laser energy pulses of ~ 500 mJ were adopted, we investigated the effect of using a fluence $f = 6.5\ J/cm^2$, corresponding in our case to a pulse energy of 500 mJ. The background pressure was set at 50 and 100 Pa. Moreover, the deposition time was increased from 30 minutes to 2 hours, in order to try to get more Raman signal from the small TiN crystalline phases present in the nanoporous films. The deposition conditions are summarized in Tab. 3.4. The film densities were estimated on the basis of QCM results obtained for the other samples. More specifically, the mass densities (m_A) for $f = 6.5\ J/cm^2$ and $p = 50 - 100\ Pa$ were not directly measured, but simply calculated from the mass densities previously obtained for $f = 2 - 3.5\ J/cm^2$ and $p = 50 - 100\ Pa$ (whose values are shown in Tab. 3.2 and Tab. 3.3) by assuming a linear increase of m_A with fluence. In Fig. 3.10 the estimated density values for $f = 6.5\ J/cm^2$ are represented in comparison to those obtained for the other fluences . It can be observed that samples TiN_P50_F6.5 and TiN_P100_F6.5 have similar density to samples TiN_P20_F3.5 (obtained at $f = 3.5\ J/cm^2$ and $p = 20\ Pa$) and TiN_P50_F3.5 (obtained at $f = 3.5\ J/cm^2$ and $p = 50\ Pa$), respectively. Moreover, in SEM cross section images (Fig. 3.11) it is shown that samples TiN_P50_F6.5 and TiN_P100_F6.5 have rather similar morphology to samples TiN_P20_F3.5 and TiN_P50_F3.5, respectively. Thus, by

confronting samples with similar porosity and morphology, an evaluation on the effects on film composition given by the use of a higher laser fluence can be made.

6.5 J/cm^2	**50 Pa**	**100 Pa**
Sample name	TiN_P50_F6.5	TiN_P100_F6.5
Density (g/cm^3)	2.31	1.12

Table 3.4: Summary of deposition conditions, denomination and estimated densities for the samples deposited at f = 6.5 J/cm^2 for 2 hours.

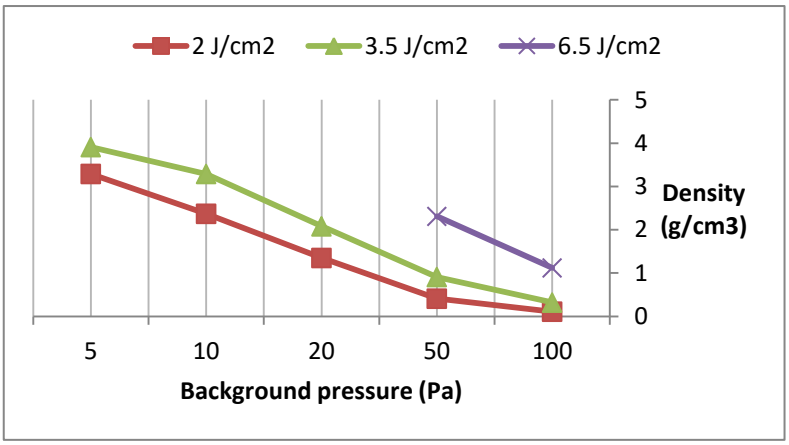

Figure 3.10: Density dependence on the operating pressure for films obtained at laser fluences (red line) 2 J/cm^2 , (green line) 3.5 J/cm^2, and (purple line) 6.5 J/cm^2.

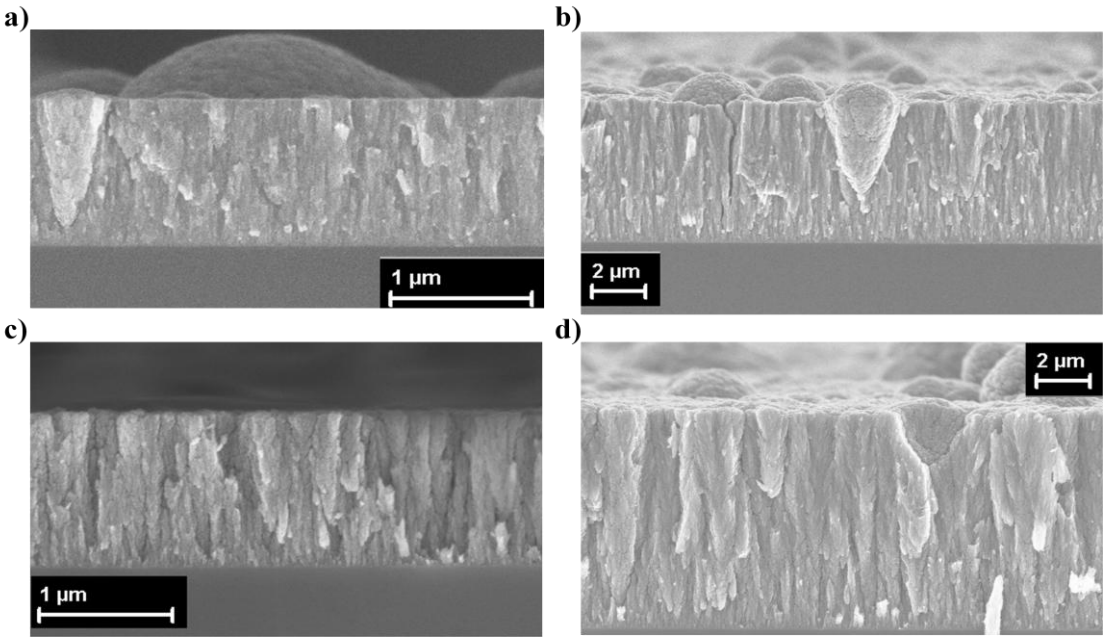

Figure 3.11: SEM cross section images of samples (a) TiN_P20_F3.5, (b)TiN_P50_F6.5, (c) TiN_P50_F3.5, and (d) TiN_P100_F6.5.

By analyzing Raman spectra in Fig. 3.12, it is possible to observe that the effect of fluence increase did not change much the structure of the denser film (Fig. 3.12a). In fact, the only differences between Raman spectra of samples TiN_P20_F3.5 and TiN_P50_F6.5 consist in the latter manifesting a more pronounced formation of TiN acoustic band (at 250-350 cm^{-1}) and a slight increase in intensity for the band at 450-600 cm^{-1}. On the other hand, fluence effect resulted to be effective in reducing film oxidation for the less dense film (Fig. 3.12b): while only an amorphous TiO_2 signal was given by sample TiN_P50_F3.5, the typical titanium oxynitride signal (with band at 300-400 cm^{-1}) was obtained for sample TiN_P100_F6.5. Similar spectra for TiO_xN_y have been reported in literature [29].
The analysis of optical curves (Fig. 3.13a,b) brought some unexpected but interesting results. The samples TiN_P50_F6.5 and TiN_P100_F6.5 have a broad-band and very high absorbance (~ 85-96 %) all over the UV-Vis-NIR spectrum (wavelengths range 270-2000 nm). They appeared as dark-gray/black (Fig. 3.13c,d). To verify that these optical features were not simply due to the high thickness of such films, which had been deposited for 2 hours, two samples (TiN_P20_F3.5_b and TiN_P50_F3.5_b) were fabricated at the same pressure and fluence conditions of TiN_P20_F3.5 and TiN_P50_F3.5, respectively, but with a deposition time of 2 hours. The obtained thicknesses and optical spectra in comparison with those of samples TiN_P20_F3.5 and TiN_P50_F3.5 are illustrated in Tab. 3.5 and Fig. 3.14, respectively. The higher film thickness seems to not influence much the absorbance spectra. So, this can suggest that the high and broadband absorbance of samples TiN_P50_F6.5 and TiN_P100_F6.5 is not due to their high thickness, but rather to their different structure with respect to samples TiN_P20_F3.5 and TiN_P50_F3.5. In particular, one possible explanation to the optical behavior of samples TiN_P50_F6.5 and TiN_P100_F6.5 may be that the obtained porous nanostructure acts as an efficient light trap, hence simultaneously stimulating different localized surface plasmon resonances which greatly enhance absorption.
Broadband "perfect" absorber can be applied to solar cells, thermal photovoltaics and hot-electron devices [102, 103, 104]. The best performances for TiN broadband absorption have been achieved in 2019 by Gao et al. [69]: thanks to a four layer structure and a TiN ring-square nanodisk array, they obtained from $\lambda = 200\,nm$ to $\lambda = 1200\,nm$ an absorption higher than 90% (with an average value of 94%) (see Fig. 1.24). However, existing ultraviolet to near-infrared broadband absorbers typically suffer from limited wavelength-range where absorption is high (i.e. higher than than 90%) and are made by complex structures difficult to fabricate. Our titanium (oxy)nitride nanoporous films could represent a promising alternative in terms of rather simple structure and broadband absorbance from the UV ($\lambda = 270\,nm$) to the NIR ($\lambda = 2000\,nm$). In particular, sample TiN_P100_F6.5, with its tree-like morphology constituted by compact arrangement of trees with average sizes around 400-500 nm (see Fig. 3.15), shows an absorbance higher than 90% in the wide range 270-2000 nm and an average absorbance of 94.8%.

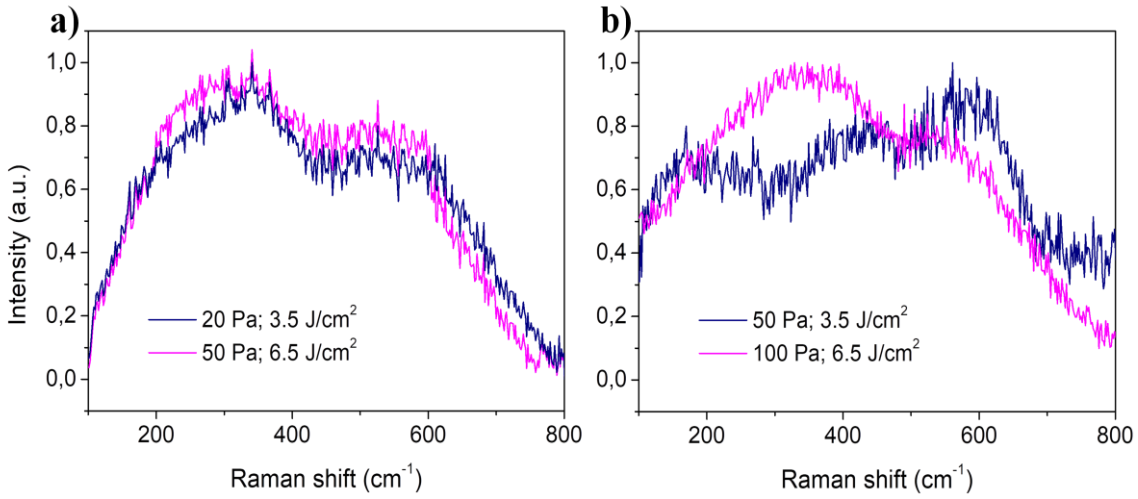

Figure 3.12: Comparison of Raman spectra of TiN thin films of similar densities deposited at different fluence (blue line for 3.5 J/cm^2, purple line for 6.5 J/cm^2) and pressure. (a) Samples TiN_P20_F3.5 and TiN_P50_F6.5; (b) samples TiN_P50_F3.5 and TiN_P100_F6.5.

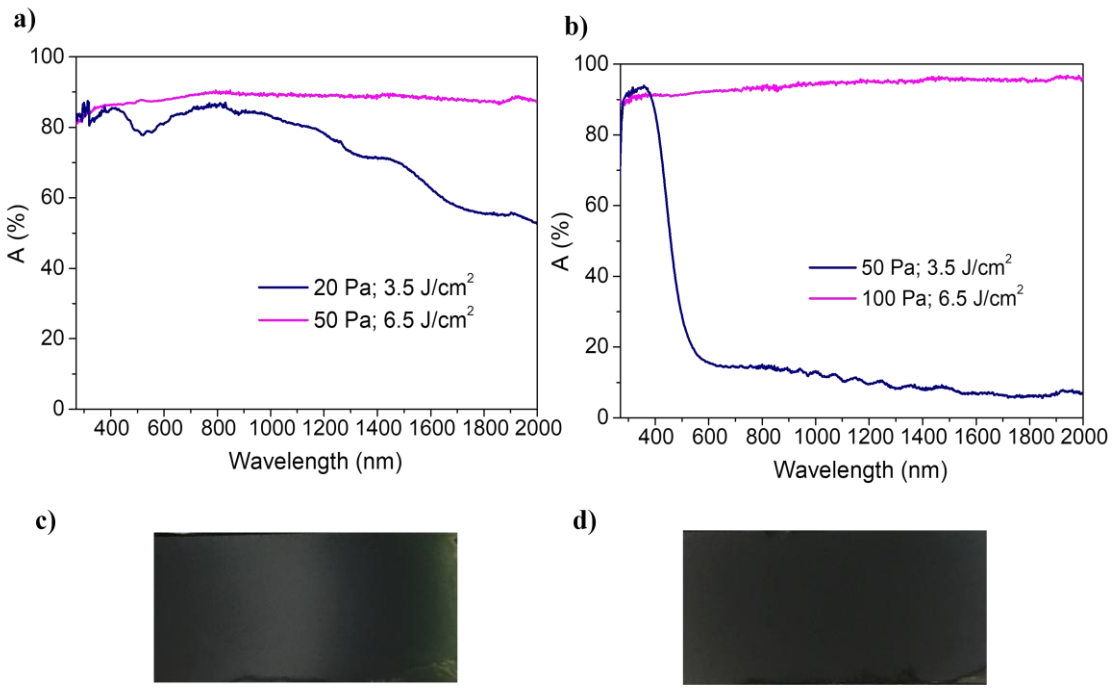

Figure 3.13: Comparison of absorbance spectra of TiN thin films of similar densities deposited at different fluence (blue line for 3.5 J/cm^2, purple line for 6.5 J/cm^2) and pressure. (a) Samples TiN_P20_F3.5 and TiN_P50_F6.5; (b) samples TiN_P50_F3.5 and TiN_P100_F6.5; pictures of (c) sample TiN_P50_F6.5 and (d) sample TiN_P100_F6.5 deposited on glass substrates.

3.5 J/cm^2	20 Pa		50 Pa	
Sample name	TiN_P20_F3.5	TiN_P20_F3.5_b	TiN_P50_F3.5	TiN_P50_F3.5_b
Deposition time (hr)	0.5	2	0.5	2
Thickness (nm)	950	3990	1350	5850

Table 3.5: Thickness values for samples TiN_P20_F3.5, TiN_P20_F3.5_b, TiN_P50_F3.5 and TiN_P50_F3.5_b, with related deposition conditions.

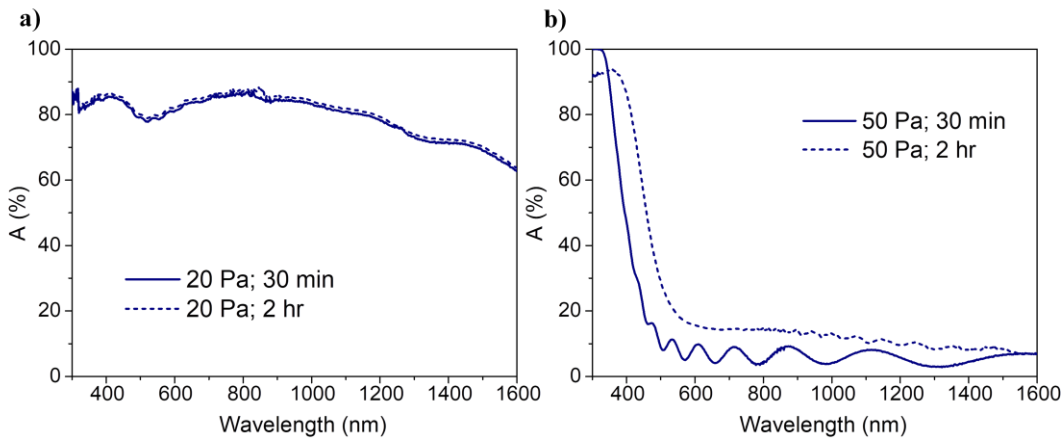

Figure 3.14: Absorbance spectra of samples (a) TiN_P20_F3.5 (solid line), TiN_P20_F3.5_b (dashed line); (b) TiN_P50_F3.5 (solid line), and TiN_P50_F3.5_b (dashed line).

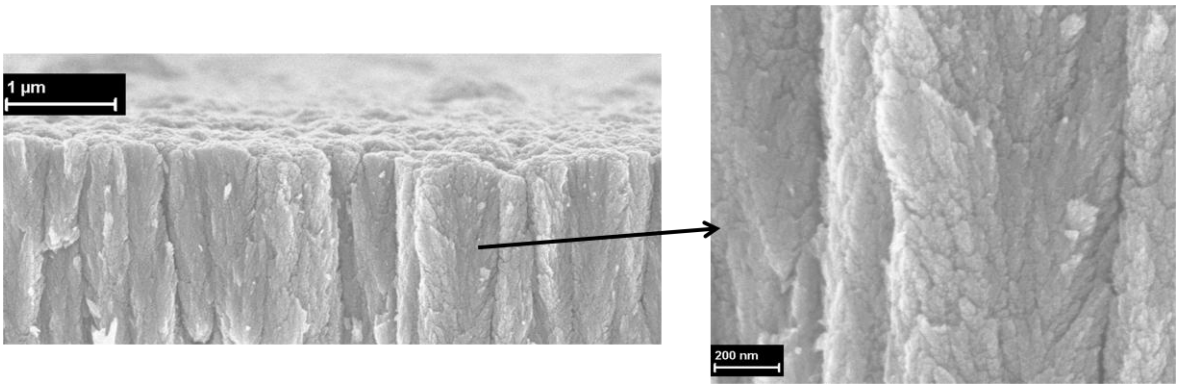

Figure 3.15: SEM cross-section images of sample TiN_P100_F6.5. Zoom out of the nano-trees details in the inset.

3.2.2 Oxidation after air exposure

Another possible source of oxidation comes from the oxygen that fills nitrogen vacancies of the fabricated TiN films after their exposure to air. This phenomenon is known to always occur for TiN films. In the case of compact films, this leads to the formation of a thin (~ few nm) oxide surface layer which is not affecting much the bulk composition [36, 37, 39]. However, films characterized by higher porosity (like our films constituted by NPs assemblies) have a much more extended surface area, hence they can severely suffer air exposure oxidation and their bulk composition can be modified by a considerable amount. In order to prevent this, Barragàn et al. [79] covered their TiN NPs with a Si_3N_4 (which eventually becomes SiO_xN_y after air exposure) capping layer. This was done just after NPs PECVD deposition, without taking the sample out of the vacuum chamber. Such capping layer reduced post-deposition oxidation by acting as a diffusion barrier against molecular oxygen.

In this work, we decided to cap our films with a compact layer of aluminum nitride (AlN), which in literature is found to be used as an efficient oxygen diffusion barrier [105, 106]. When in contact with air, AlN forms a AlO_xN_y interlayer, which is a very stable oxide and acts as a passivating protective layer.

Before starting to fabricate the capped TiN samples, we deposited some films of just the capping layer in order to optimize the operation conditions and to study their Raman and optical spectra. Even if we did not deeply study the structure of these films and we are not sure of what has been obtained (in fact there is no Raman signal, as it will be discussed below), we adopted the same deposition conditions used for compact TiN thin films, by analogy. In this way, we obtained an adherent, uniform and compact layer by ablating an Al target (purity 99.9%) with a laser fluence $f = 2\,J/cm^2$ and a N_2-H_2 background pressure of 1 Pa. The deposition time was set at 9 minutes in order to obtain a thickness of 200 nm. This thickness value was chosen because a lower one could have covered unevenly and only partially the nanoporous films; while a bigger one may have affected too much the underlying films' properties. Fig. 3.16a shows that the film has very high transparency and low absorbance and reflectivity all over the UV-Vis-NIR spectrum. From Fig. 3.16b it can be seen that the obtained film gives practically no Raman signal, since its spectrum is very similar to that of the glass substrate. Therefore, such cap layer will not affect much neither Raman nor optical spectra of the underlying TiN.

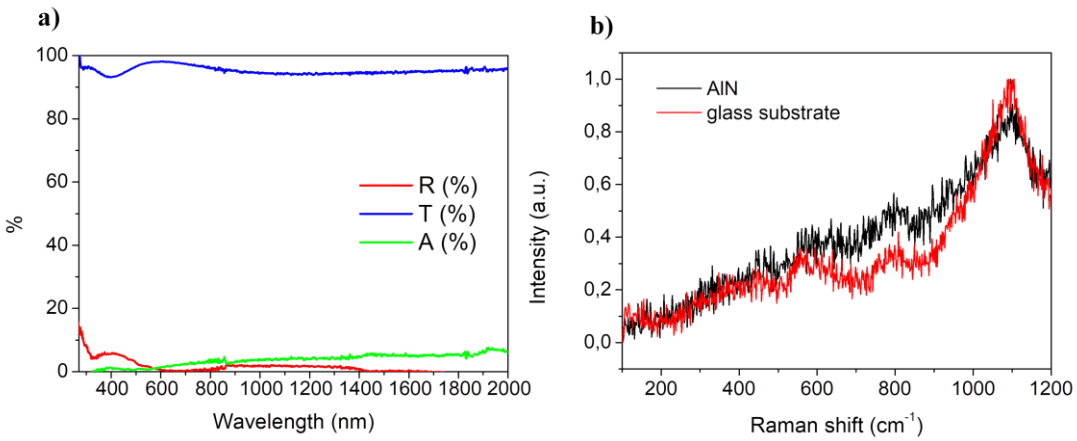

Figure 3.16: (a) Cap layer optical curves; (b) Cap layer Raman spectrum (black) compared to that of the glass substrate (red).

In order to deposit the capping layers on top of the films without opening the vacuum chamber, the following procedure was adopted. A small diameter (1 inch) TiN target (purity 99.9%) was attached on top of the bigger (2 inches) Al target (as shown in Fig. 3.17) using some carbon tape. First, the TiN films were deposited by ablating only the TiN target. Then, the target-holder translation was stopped and only rotational motion was allowed, in such a way that only the underlying Al target could be hit by the laser spot; the fluence and background pressure were changed and the compact AlN layer was synthesized. The deposition conditions of capped samples are summarized in Tab. 3.6. It should be underlined that samples denominated in Tab. 3.6 as Cap_P10_F3.5, Cap_P20_F3.5 and Cap_P50_F3.5 are the capped versions of samples TiN_P10_F3.5, TiN_P20_F3.5 and TiN_P50_F3.5, respectively.

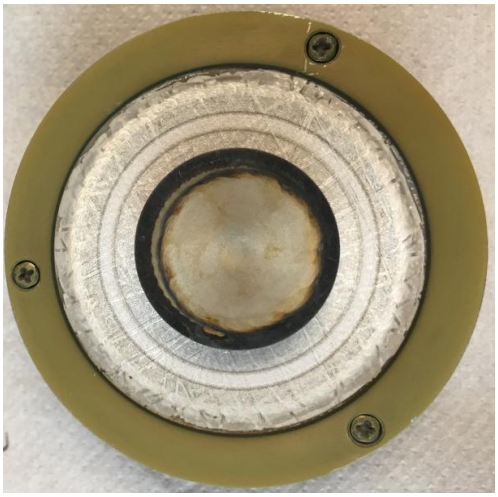

Figure 3.17: Targets configuration used to deposit films with capping layer. The white/gray underlying target is Al, the smaller gold/gray target on top is TiN.

Target	Deposition time (min)	Fluence (J/cm^2)	Pressure (Pa)		
TiN	30	3.5	10	20	50
Al	9	2	1	1	1
Sample name			Cap_P10_F3.5	Cap_P20_F3.5	Cap_P50_F3.5

Table 3.6: Summarization of deposition conditions adopted for the TiN films with AlN capping layer on top.

The presence of the capping layer did not affect much the structure of the two more compact films; in fact, the Raman spectra of samples Cap_P10_F3.5 and Cap_P20_F3.5 are rather similar to those of samples TiN_P10_F3.5 and TiN_P20_F3.5, respectively. In particular, the denser capped film (i.e. Cap_P10_F3.5) presented the smallest differences with respect to the uncapped counterpart (Fig. 3.18a). Sample Cap_P20_F3.5's Raman spectrum instead (Fig. 3.18b) showed a slightly higher intensity of the optical band at 550 cm^{-1} and a slightly blue-shifted acoustic band, which may indicate a small increase in nitrogen concentration with respect to the respective uncapped film. However, further analysis on films composition should be performed in order to verify these assumptions.
In Fig. 3.18c it can be seen that the absorption peak of sample Cap_P10_F3.5 is red-shifted to $\lambda \cong 790\, nm$ with respect to that of sample TiN_P10_F3.5 (which was located at $\lambda \cong 610\, nm$). Consequently, the inter-band transitions in the lower-wavelengths region become more visible. Besides, sample Cap_P20_F3.5's absorption peak is centered around the same wavelength of sample TiN_P20_F3.5 (Fig. 3.18d).
Nevertheless, the absorption peaks of the capped samples were expected to be blue-shifted with respect to the uncapped ones, because a lower oxygen incorporation would lead to a higher charge carrier concentration. The obtained results could be explained by considering that the presence of a high refractive index ($n \cong 2.01$ for AlN) cap layer may affect the underlying film's optical behavior. In particular, as discussed in section 1.3, a surrounding medium with a high refractive index can red-shift the intra-band absorption peak of the film. So, the cap layer may produce two contrasting effects on the absorbance curves: on one side the blue-shift induced by the lower oxidation, on the other side the red-shift generated by the high refractive index. The latter seems to be the dominant effect for sample Cap_P10_F3.5, whose porosity was probably not high enough to severely suffer from air-exposure oxidation. For sample Cap_P20_F3.5 the two effects seem to be perfectly counterbalanced; the absorption peak position is indeed unchanged.
On the other hand, for the least dense sample Cap_P50_F3.5 (whose SEM cross section is shown in Fig. 3.19a), the cap layer resulted to be highly effective in reducing air-exposure oxidation. In fact, as it is illustrated in Fig. 3.19b, while the uncapped sample (TiN_P50_F3.5) shows the typical Raman spectrum of amorphous TiO_2, the capped sample (Cap_P50_F3.5) shows a spectrum that can be associated to sub-stoichiometric TiN.

Moreover, while TiN_P50_F3.5 has a very low absorbance and very high transparency in the Vis-NIR (typical of amorphous titanium oxide), Cap_P50_F3.5 manifests a neat intra-band absorption peak located at $\lambda \cong 925\, nm$ and a transmittance peak at $\lambda \cong 685\, nm$ (Fig. 3.19c-d). In addition, the inter-band absorption peak is located in the visible, centered at $\lambda \cong 450\, nm$: this gives the sample a dark blue-ish color (while TiN_P50_F3.5 was transparent with some yellowish shades), as it can be seen in Fig. 3.20.

The presence of a transmittance peak and of an increasing transmittance at long wavelengths are features already encountered in other works dealing with TiN nanostructures (i.e. Fig. 1.35a), and can be related to the presence of a certain amount of oxidation. It should be specified that the intra-band absorption peak's position is probably influenced also by the cap layer's refractive index, as previously discussed.

It can be noticed from the optical curves of the three capped samples (purple lines in Fig. 3.18c-d and Fig. 3.19d) that the absorption peak located at shorter wavelengths (which may be associated to inter-band transitions) raises in intensity and red-shifts when going from sample Cap_P10_F3.5 to Cap_P20_F3.5 and eventually to Cap_P50_F3.5. At the same time, the absorption peak located at longer wavelengths (which may be indeed associated to intra-band transitions) decreases in intensity and red-shifts. As discussed in section 3.1, this variation in the absorption spectra may be due to the progressive transition from a more compact TiN film-like optical behavior to a more TiN NPs-like one.

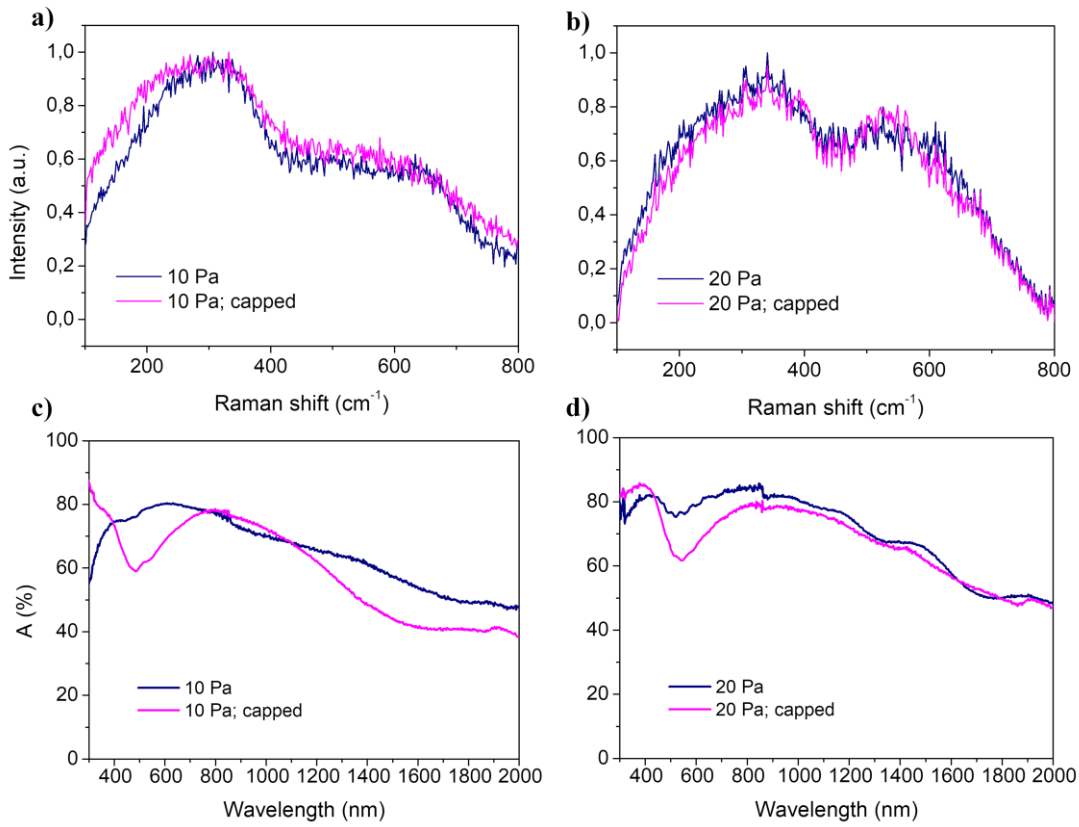

Figure 3.18: Comparison between TiN_P10_F3.5 and Cap_P10_F3.5 (a) Raman spectra and (c) absorbance spectra; comparison between TiN_P20_F3.5 and Cap_P20_F3.5 (b) Raman spectra and (d) absorbance spectra.

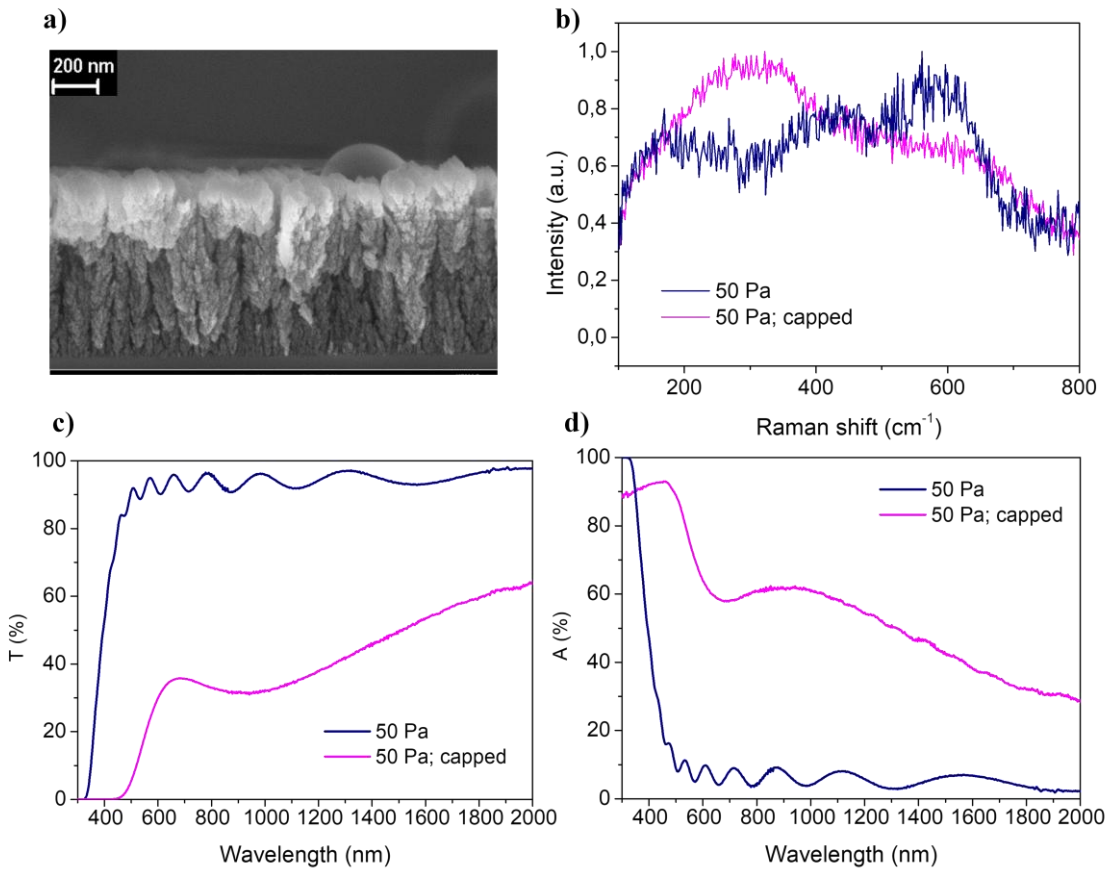

Figure 3.19: (a) SEM cross-section image of sample Cap_P50_F3.5; (b) Raman spectra of sample Cap_P50_F3.5 in comparison to that of sample TiN_P50_F3.5; (c) Transmittance and (d) absorbance curves of sample Cap_P50_F3.5 in comparison to those of sample TiN_P50_F3.5.

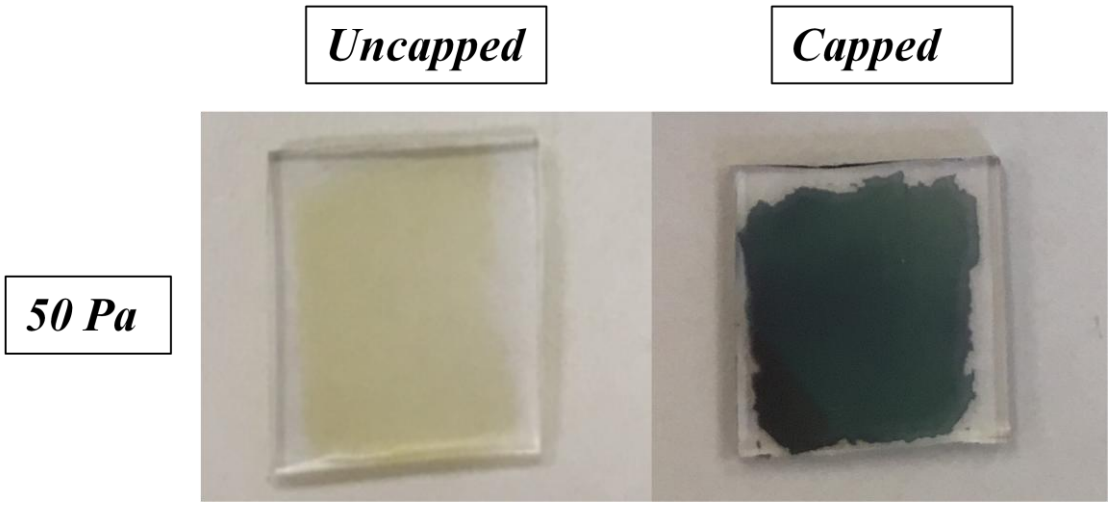

Figure 3.20: Samples TiN_P50_F3.5 (on the left) and Cap_P50_F3.5 (on the right).

In conclusion, the two adopted strategies resulted to be effective in reducing oxygen incorporation within the samples characterized by lower density values. In particular, tree-like nanostructured TiN films with density $\rho \cong 0.91\ g/cm^3$ have been obtained. In this way, the density range at which TiN thin films (rather than just amorphous TiO_2 films) are obtained has been extended from $\rho \cong 2.08\ g/cm^3$ (i.e. sample TiN_P20_F3.5) down to $\rho \cong 0.91\ g/cm^3$ (i.e. sample Cap_P50_F3.5).

First, by using a fluence $f = 6.5\ J/cm^2$ and a pressure $p = 100\ Pa$, we obtained a ~ 6 µm thick tree-like nanostructured TiO_xN_y film showing a very high and broad-band absorption all over the UV-Vis-NIR spectrum.

Second, by capping with a AlN 200 nm thick compact layer a film previously deposited with $f = 3.5\ J/cm^2$ and $p = 50\ Pa$, we obtained a tree-like nanostructured (sub-stoichiometric) TiN film featuring a intra-band absorption peak at $\lambda \cong 925\ nm$.

Effect of post deposition annealing on TiN nanostructured thin films

In this chapter, we analyzed the effect of thermal treatments on the structure and optical properties of both uncapped and capped samples.

In the first part of the chapter, the effect of different annealing atmospheres and temperatures on uncapped samples were investigated. In this section, the annealings were performed either in vacuum or with N_2-H_2 (95-5 %) supply at controlled overpressure of 1050 mbar; the process time and the heating ramp were kept constant at 1 hr and 10°C/min, respectively, while two different temperatures were selected (300 and 550°C, similar to those used in literature, as discussed in section 1.2). In particular, after annealing in vacuum a higher film crystallinity and the desorption of surface oxygen were expected, while after annealing in N_2-H_2 atmosphere the film composition was expected to become enriched in nitrogen and depleted in oxygen, and the film crystallinity was likely to improve as well. Two different annealing temperatures (i.e. 300 and 550°C) were investigated in order to find a good compromise between amorphous phase oxidation and crystallization (which are both favored by higher temperatures).

In the second part of the chapter, we analyzed the effect of annealing on samples where the strategies against oxidation had been adopted. In particular, we examined the effect of N_2-H_2 annealing at 300°C on capped samples deposited at both fluences 3.5 and 6.5 J/cm^2. Only the aforesaid thermal treatment's atmosphere and temperature were adopted since in the first section of the chapter they seemed to give better results.

In Tab. 4.1 the samples which have been thermally annealed are reported with their denomination. The structural and optical properties of these films were studied by SEM (see section 2.2), Raman spectroscopy (2.3) and UV-Vis-NIR spectrophotometry (2.4). The apparatus used for the thermal treatments has been illustrated in section 2.5. Finally, all the films have been deposited both on glass and silicon substrates.

Sample	Fluence (J/cm^2)	Pressure (Pa)	Cap layer	Annealing atmosphere	Annealing temperature (°C)
AV550_P10_F3.5	3.5	10	-	Vacuum	550
AN550_P10_F3.5	3.5	10	-	N_2-H_2	550
AN300_P10_F3.5	3.5	10	-	N_2-H_2	300
AV550_P20_F3.5	3.5	20	-	Vacuum	550
AN550_P20_F3.5	3.5	20	-	N_2-H_2	550
AN300_P20_F3.5	3.5	20	-	N_2-H_2	300
AV550_P50_F3.5	3.5	50	-	Vacuum	550
AN550_P50_F3.5	3.5	50	-	N_2-H_2	550
AN300_P50_F3.5	3.5	50	-	N_2-H_2	300
Cap_AN300_P10_F3.5	3.5	10	Yes	N_2-H_2	300
Cap_AN300_P20_F3.5	3.5	20	Yes	N_2-H_2	300
Cap_AN300_P50_F3.5	3.5	50	Yes	N_2-H_2	300
AN300_P50_F6.5	6.5	50	-	N_2-H_2	300
AN300_P100_F6.5	6.5	100	-	N_2-H_2	300
Cap_AN300_P50_F6.5	6.5	50	Yes	N_2-H_2	300
Cap_AN300_P100_F6.5	6.5	100	Yes	N_2-H_2	300

Table 4.1: Summary of the deposition and annealing conditions adopted for the samples studied in this chapter. In the upper part of the table, samples analyzed in section 4.2.1 are reported. In the bottom part instead, those of section 4.2.2 are reported.

4.1 Effect of annealing atmosphere and temperature

In this first section, the effect of annealing atmosphere and temperature will be studied. Only uncapped samples will be considered, as illustrated in Tab. 4.1. It should be specified that a deeper investigation using two different temperatures has been adopted only for the annealing in N_2-H_2 atmosphere, since, from a previous work on compact TiN films carried on in our laboratory [9], it resulted to be more efficient than vacuum annealing in reducing oxidation and increasing the nitrogen content within TiN films.
For compact TiN films with relatively large crystalline domains (i.e. sizes of few μm) a temperature of 550°C may be effective in enlarging such domains while keeping a low thermal oxidation [41]. Moreover, our group has previously performed thermal annealing on compact TiN films at 550°C in our laboratory. So, the first annealing temperature we decided to adopt was T =550°C. However, for porous tree-like nanostructured TiN films deposited by PLD, which in literature have been found to be constituted by very small

crystallites (i.e. sizes of few nm) immersed in an amorphous matrix [87], the thermal budget for oxidation is expected to be much lower. For this reason, temperatures lower than 400°C may be used [41, 46]. In this work, we decided to select also an annealing temperature T = 300°C in order to investigate whether a better compromise between film crystallization and oxidation (which is possibly due to the oxygen adsorbed on the film surface) could be achieved.

Let us first analyze the effect of the different thermal treatments on the Raman spectra of the synthesized TiN films, trying to get information on crystallinity (which affects the width of the bands) and nitrogen vacancies (connected to the optical band intensity). In Fig. 4.1 the Raman spectra of all the samples are shown, grouped on the basis of deposition and annealing conditions. Some observations can be made:

- For samples deposited at 10 and 20 Pa the annealing in N_2-H_2 overpressure at 300°C gives a higher relative intensity of the acoustic band at 250-350 cm^{-1} . This could be related to a greater concentration of nitrogen vacancies hence to a smaller number of nitrogen atoms incorporated within the TiN crystal lattice. Nevertheless, we suppose that the main reason for this variation in Raman spectrum is the lower oxygen content within the film. This hypothesis may be supported by considering that, after the annealing, the intense broad band at 450-650 cm^{-1} (which can be associated to the presence of a underlying amorphous TiO_2 Raman signal, as discussed in section 3.1) has a lower intensity. On the other side, this behavior is not observed for the annealings carried out at 550°C.
  So, the lower temperature T = 300°C adopted for the thermal treatment in N_2-H_2 seems to have reduced the oxidation within the films deposited at 10 and 20 Pa.
  However, this hypothesis should be further verified with other techniques like EDXS or XPS.

- The acoustic band of sample deposited at 10 Pa gets narrower after annealing in N_2-H_2 overpressure at 300°C. This may be due to the higher crystallinity of the annealed film. On the other hand, annealing in vacuum and in N_2-H_2 overpressure at 550°C performed on the same sample do not give any evident difference in terms of Raman spectrum.
  Furthermore, for the film deposited at 20 Pa, the appearance of the transverse acoustic mode contribution around 250 cm^{-1} (indicated by a red arrow in Fig. 4.1) after annealing in N_2-H_2 at 300°C may indicate a slightly improved crystallization of the TiN film (as reported in literature [29]). On the other side, the annealing in vacuum give an amorphous TiO_2 spectrum, while the annealing in N_2-H_2 at 550°C give broader and more undefined bands.
  So, annealing in N_2-H_2 overpressure at 300°C seems to have improved the crystallinity of the films deposited at 10 and 20 Pa.
  However, this hypothesis should be further verified with other techniques like XRD.

- Contrary to the hypothesis made in section 3.1, according to which a longer exposure to nitrogen leads to a blue-shift of the acoustic band below 400 cm^{-1}, none of the spectra of the films annealed in N_2-H_2 present this shift. Moreover, the intensity of the optical band around 600 cm^{-1} does not increase for any film after annealing in N_2-H_2. Probably the nitrogen incorporation during such N_2-H_2 annealing was not sufficiently high to bring visible changes in the Raman spectrum.

- For samples deposited at 50 Pa, all the thermal treatments lead to the crystallization of the amorphous TiO_2 present. Sample AV550_P50_F3.5 shows the Raman spectrum of a mixed rutile-anatase phase, while sample AN550_P50_F3.5 of anatase and sample AN300_P50_F3.5 of amorphous TiO_2. So, none of the three annealings seem to have been successful in reducing oxidation within the as-deposited (uncapped) tree-like nanostructured TiN film (i.e. sample TiN_P50_F3.5).

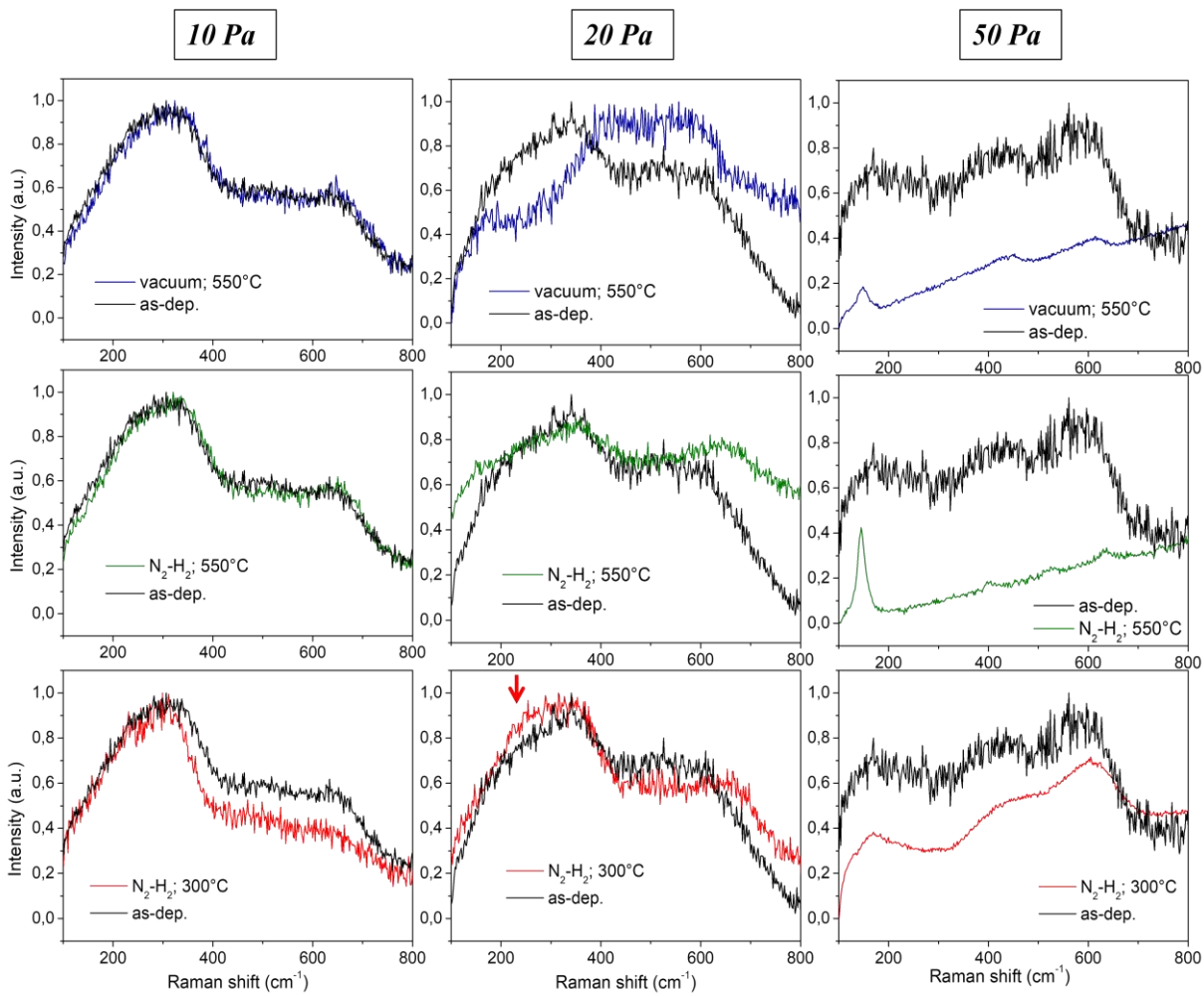

Figure 4.1: Raman spectra of TiN films deposited with f = 3.5 J/cm^2 at 10, 20 and 50 Pa and annealed: in vacuum at 550°C (blue lines), in N_2-H_2 overpressure at 550°C (green lines), and in N_2-H_2 overpressure at 300°C (red lines).

The color of the sample deposited at 20 Pa slightly changes from black/dark-green to brown, while the color of the sample deposited at 10 Pa goes from dark-blue to bronze after annealing in N_2-H_2 overpressure at 300°C (see Fig. 4.3). In literature, such color change towards bronze-brown tones typically occur for TiN films annealed in N_2 at temperatures around 300-400°C, and they can be related to the higher nitrogen content within the film together with the creation of different titanium oxynitride phases [46].
In Fig. 4.2 the transmittance, reflectance and absorbance curves for samples deposited at 10, 20 and 50 Pa with (f = 3.5 J/cm^2) before and after the three different thermal treatments are illustrated. By analyzing these optical curves, we can make some observations:

- For samples deposited at 10 and 20 Pa the annealing in N_2-H_2 overpressure at 300°C is the thermal treatment that reduces the most the transmittance peak, and it is the only one to blue-shift such a peak (from $\lambda \approx 500\,nm$ to $\lambda \approx 380\,nm$ for AN300_P10_F3.5 and from $\lambda \approx 550\,nm$ to $\lambda \approx 480\,nm$ for AN300_P20_F3.5). As previously mentioned (in section 3.1), this behavior can be associated to a lower oxygen content incorporated within the film. Moreover, the transmittance tail at longer wavelengths reduces.
  So, in accordance with Raman spectra analysis, the lower temperature T = 300°C adopted for the thermal treatment in N_2-H_2 seems to have reduced the oxidation within the films deposited at 10 and 20 Pa. However, this hypothesis should be further verified with other techniques like EDXS or XPS.

- The reflectance of the sample deposited at 10 Pa significantly changes after annealing in N_2-H_2 overpressure at 300°C. It gets higher, especially at longer wavelengths where it reaches values around 65 % after a steep plasma reflectance edge. Moreover, a reflectance minimum appears at $\lambda \approx 470\,nm$. A blue-shifted and more intense reflectance minimum together with a steeper reflectance edge are generally associated in literature to a higher carrier density. The latter increases with both decreasing nitrogen and oxygen content within the film. So, the annealing may have reduced either oxidation or nitrogen incorporation, or both. Nevertheless, since the reflectance curve's features are similar to those of nearly-stoichiometric TiN films found in literature [48] and since the Raman spectra analysis did not show any vacancy concentration variation, we could hypothesize that the nitrogen content within the film did not change much. Consequently, the increase in carrier density may be mostly due to oxidation reduction. Again, it should be specified that this whole discussion is just an hypothesis which should be further verified.
  The absorbance peak of the sample deposited at 10 Pa becomes narrower and blue-shifted to $\lambda \approx 470\,nm$ after the thermal annealing in N_2-H_2 at 300°C. Furthermore, instead of the two absorbance maxima of the as-deposited TiN film, after annealing there is just a single peak. It can be assumed that the contributions to absorption given by inter and intra-band transitions overlap in the same wavelength range.
  As discussed in section 3.1, this variation in the absorption curve may be due to the progressive transition from a more TiN NPs-like optical behavior to a more compact TiN film-like one. However, from SEM cross section images no clear

change towards a more compact morphology can be detected. Moreover, since this "single-peak" absorption spectrum cannot be observed for the samples thermally annealed at 550°C, it is not clear how this hypothetical change in morphology could have been achieved only for the film annealed in N_2-H_2 overpressure at 300°C and not, for example, for the film annealed at 550°C in the same atmosphere.
So, this variation in the absorption curve could be due to the lower oxygen content within the film, that may have become considerably enriched in free electrons after annealing.

- For sample deposited at 20 Pa the reflectance does not change upon annealing, and stays low and constant along the whole wavelengths spectrum. On the other hand, considering that the transmittance peak decreases, the two absorbance maxima of the as deposited film almost completely overlap into one single-peak after thermal treatment in N_2-H_2 at 300°C. Moreover, this single-peak is broad and with an intensity around 80% for almost the whole analyzed wavelength interval.
  The different color and different absorbance curve after annealing suggest a modification in the film structure and composition.

- For sample deposited at 10 Pa, the vacuum annealing at 550°C and the N_2-H_2 annealing at 550°C do not give evident variations of the optical curves. This seems to be in accordance with the fact that these thermal treatments did not bring any clear structural modification, as observed from the Raman spectra analysis.
  For samples deposited at 20 Pa, the two aforesaid thermal treatments lead to higher transmittance peaks and lower intra-band absorption intensities. In particular, the sample annealed in vacuum (i.e. AV550_P20_F3.5) shows very high transmittance and low absorbance, indicating a great oxidation extent. This is in accordance with Raman analysis, where a typical signal of amorphous TiO_2 was measured for that sample.

- For sample deposited at 50 Pa, all the three thermal treatments do not give any optical feature that can be associated to TiN. This is in accordance with Raman analysis, where the spectra of either amorphous or crystalline TiO_2 were obtained.
  The color of the sample changes from transparent (with some yellowish shades) to a slightly more intense brownish tone (as it is shown in Fig. 4.3 for the case of thermal treatment in N_2-H_2 at 300°C) .
  The transmittance reduces and the absorbance increases after all the annealings, but neither a transmittance nor an absorbance peak which can be associated to titanium nitride are formed. This optical behavior is similar to what can be found in literature for amorphous TiO_2 films annealed in air and in Ar/H_2 at 500°C [10].

To conclude, this study on the effects of thermal treatment on the deposited samples allowed us to obtain information regarding the films' morphological, structural, and optical properties variation as a function of different annealing atmospheres and temperatures. In

particular, the annealing in vacuum seemed to increase the oxidation extent within the films (especially the more porous ones), thus making their structural and optical properties more similar to those of titanium oxide rather than of TiN. Furthermore, lowering the annealing temperature (i.e. 300°C instead of 550°C) gave more substantial differences in terms of Raman and optical spectra with respect to changing the annealing atmosphere. In fact, the annealing in N_2-H_2 at 300°C may have reduced the oxidation and increased crystallinity within the films deposited at 10 Pa and 20 Pa, as we supposed by observing their color, Raman spectra and optical curves. More specifically, the sample deposited at 10 Pa and annealed at N_2-H_2 at 300°C may be a nearly-stoichiometric TiN characterized by a high reflectivity and by an intense and narrow absorption peak at $\lambda \approx 470\ nm$. Instead, the sample deposited at 20 Pa is a TiN (with possibly some oxide and oxynitride phases) characterized by a broad and intense absorbance in the whole Vis-NIR range.

Finally, for sample deposited at 50 Pa, all the three thermal treatments do not give any optical feature that can be associated to TiN. The annealed samples deposited at 50 Pa are indeed TiO_2 characterized by an either amorphous, anatase or rutile-anatase mixed phase. So, the adopted thermal annealings are not effective in reducing the high oxidation extent of the more porous film.

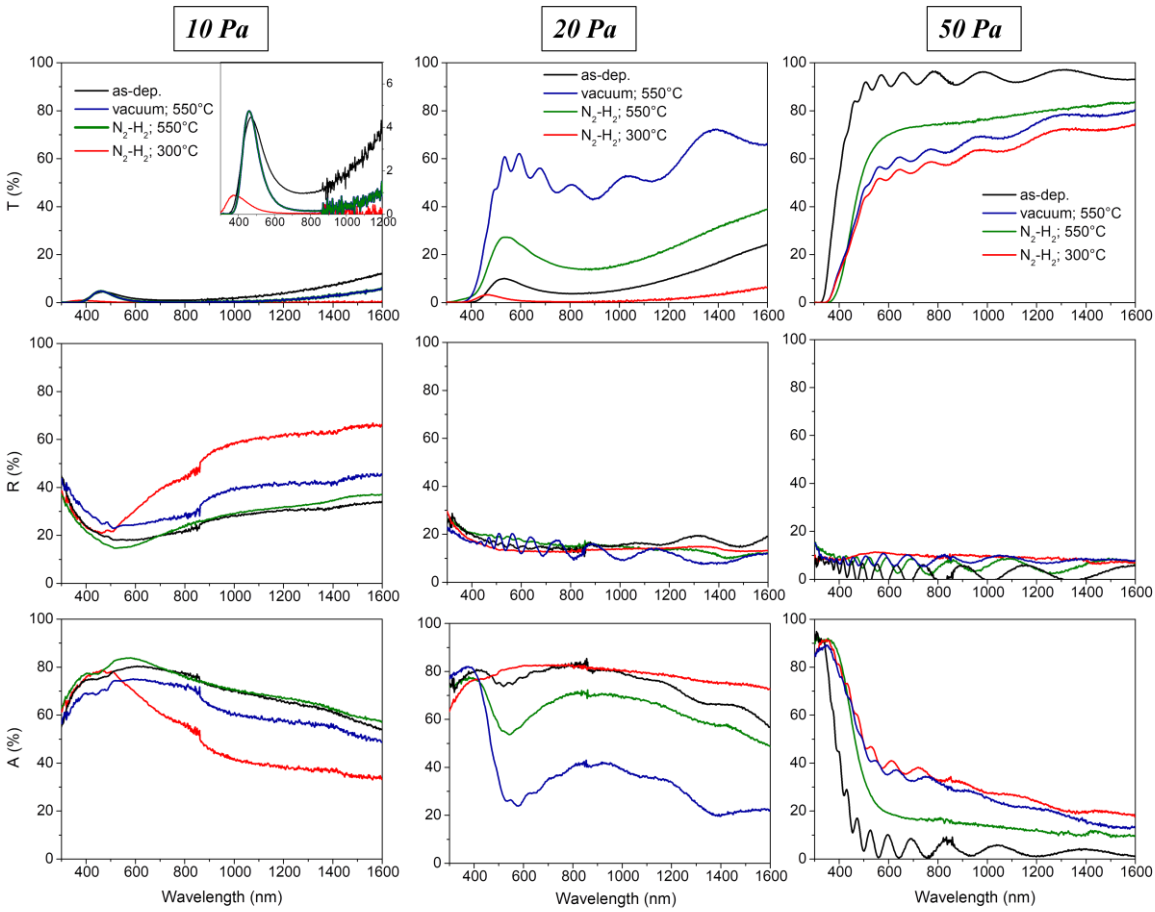

Figure 4.2: Transmittance (T), reflectance (R) and absorbance (A) curves for samples deposited at 10, 20 and 50 Pa and f = 3.5 J/cm^2 as deposited (black lines), and after thermal annealing in vacuum at 550°C (blue lines), in N_2-H_2 overpressure at 550°C (green lines) and in N_2-H_2 overpressure at 300°C (red lines).

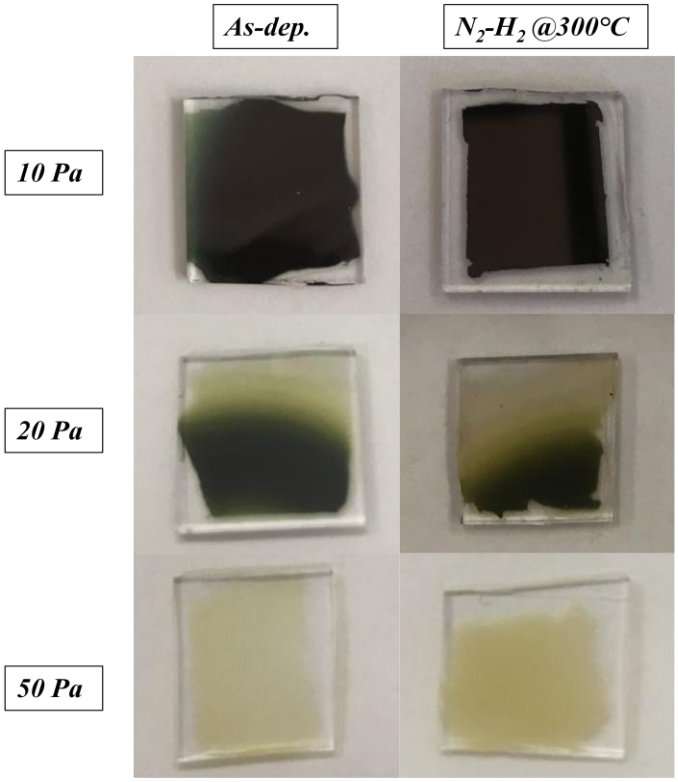

Figure 4.3: Samples deposited at 10, 20 and 50 Pa with f = 3.5 J/cm^2 before and after annealing in N_2-H_2 overpressure at T= 300°C.

4.2 Effect of annealing after strategies against oxidation

In this section, we analyzed the effect of annealing on samples where the strategies against oxidation had been adopted. In particular, we examined the effect of N_2-H_2 annealing at 300°C on capped samples deposited at fluence 3.5 J/cm^2. Then, at the end of the chapter, the annealing effect on both uncapped and capped samples obtained with fluence 6.5 J/cm^2 was briefly analyzed. Only the aforesaid thermal treatment's atmosphere and temperature were adopted since in the first section of the chapter they seemed to give better results in terms of structure and optical properties.
Moreover, the thermal annealing of samples on which the strategies against oxidation have been adopted was expected to affect the films' properties not exactly as the annealing of bare samples (which is discussed in section 4.1) did, but with some differences due to the modifications induced by the aforesaid strategies. In this way, the influence of such strategies on the behavior of the film during thermal annealing could be investigated.
All the samples analyzed in this section are reported in the bottom part of Tab. 4.1.

Let us first consider the effect of thermal treatment on the capped samples deposited at 10, 20 and 50 Pa using a fluence 3.5 J/cm^2.
From the investigation of their Raman spectra, which are reported in Fig. 4.4, we can make the following observations:

- The effect of the annealing on capped samples deposited at 10 and 50 Pa is comparable in terms of Raman spectra variation. In fact, for both samples the acoustic band at 250-350 cm^{-1} gets narrower, while the broad band at higher wave numbers (450-650 cm^{-1}) gets less intense. The acoustic-band narrowing can be associated (as already mentioned in section 4.1) to an increase in the films crystallinity. The lower intensity of the band at higher wave numbers, instead (as already mentioned in section 3.1), can be related either to a lower nitrogen content within the film or to a lower presence of oxide and oxynitride phases. The acoustic-band narrowing is the more relevant effect of the annealing on the capped sample deposited at 10 Pa, while on the capped sample deposited at 50 Pa it is the lower intensity of the band at high wave numbers.
  The annealing affects the Raman spectra of capped and uncapped samples deposited at 10 Pa in the same way (see Fig. 4.5). Apparently, the capping layer did not hinder the oxidation of the underlying films during annealing. In fact (as already observed in section 3.2) the presence of a capping layer is not effective in reducing the oxygen contamination within these more compact films, because they suffer less from air-exposure oxidation. As it can be seen in Fig. 4.6, the fact that the colors of such capped and uncapped samples after annealing are very similar (i.e. bronze) may confirm this hypothesis.

On the other hand, while the annealing did not change the structure of the uncapped film deposited at 50 Pa, which remained amorphous titanium oxide, it did change the one of the respective capped sample (see Fig. 4.5). So, the capping layer protects the more porous films from oxygen contamination during air exposure (as already supposed in section 3.2), thus preventing their oxidation during thermal treatment. This can also be clearly seen from the different colors of samples AN300_P50_F3.5 and Cap_AN300_P50_F3.5 (see Fig. 4.6).

- The effect of annealing on Raman spectrum of sample deposited at 20 Pa consists in the shift towards higher wave numbers of the peak located around 550 cm^{-1}, which can be identified as the first order defect-induced TiN optical mode (as discussed in section 2.3). However, since this peak is blue-shifted to ~ 650 cm^{-1}, it could also be due to the signal of underlying amorphous TiO_2; in fact, normally the optical mode peak lays within the wave numbers range 550-600 cm^{-1} and it does not shift much. Another possibility is that this is the peak of a crystalline AlN Raman active mode which is found in literature to be located around 655 cm^{-1} [107, 108], that may arise after the thermal treatment.
  The Raman spectra obtained are quite different between samples AN300_P20_F3.5 (see Fig. 4.5) and Cap_AN300_P20_F3.5. Thus, the presence of a capping layer affected the structure of the film deposited at 20 Pa. This hypothesis may find a further confirm in the different color of capped an uncapped samples after annealing (see fig. 4.6). Nevertheless, these structural modifications cannot be well understood because of the aforementioned various interpretations that may be given of the Raman spectrum of Cap_AN300_P20_F3.5.

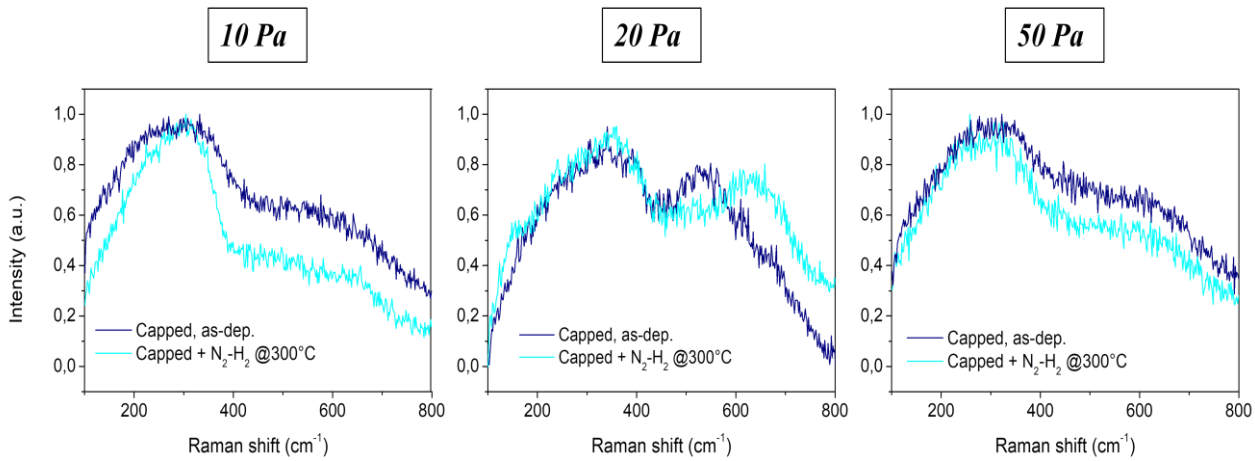

Figure 4.4: Raman spectra of capped samples deposited with f = 3.5 J/cm^2 at 10, 20, and 50 Pa (blue lines) as-deposited and (light blue lines) after annealing in N_2-H_2 at 300°C.

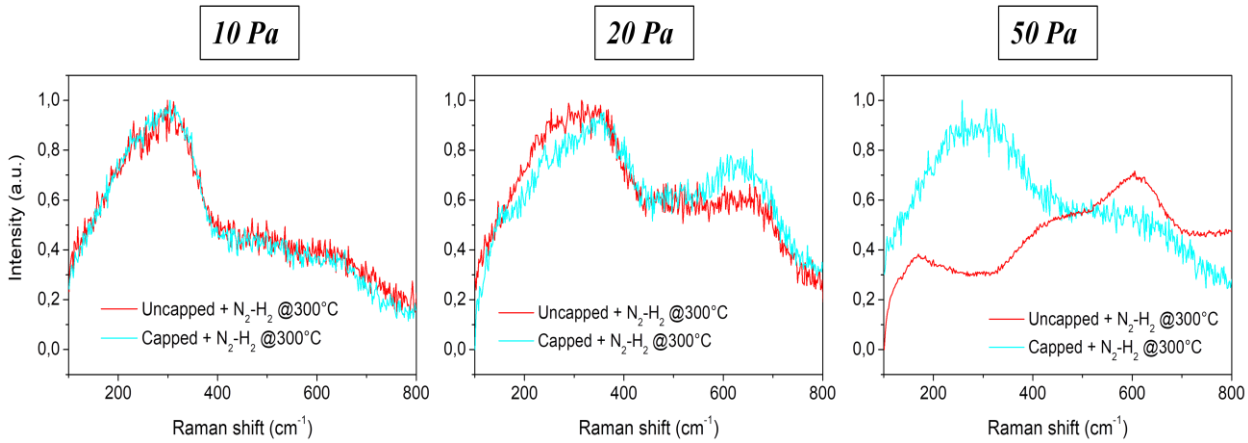

Figure 4.5: Raman spectra of samples deposited with f = 3.5 J/cm^2 at 10, 20, and 50 Pa after annealing in N_2-H_2 at 300°C , both (red lines) uncapped and (light blue lines) capped.

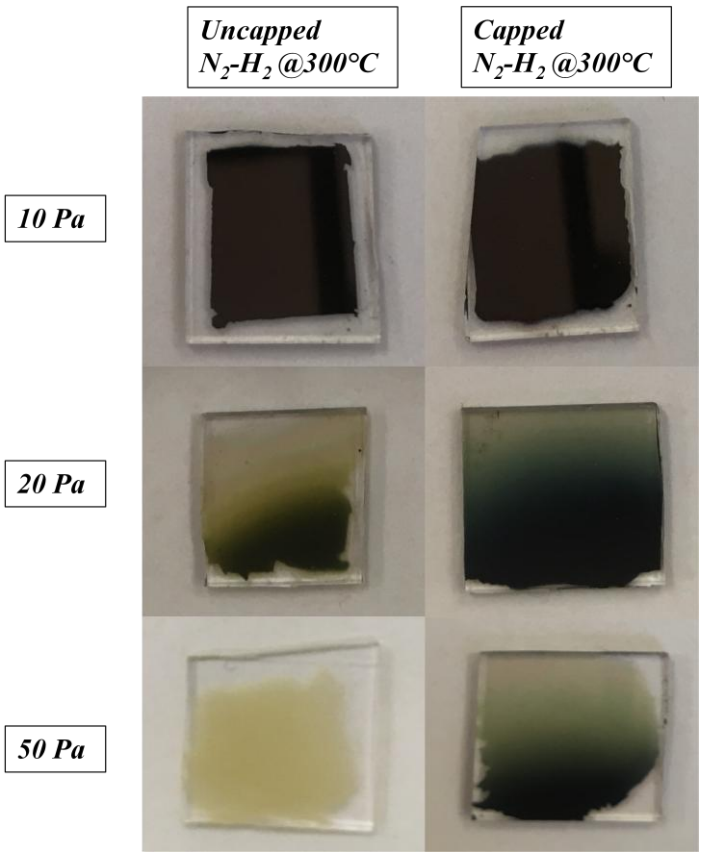

Figure 4.6: Annealed (in N_2-H_2 overpressure at 300°C) samples deposited with f = 3.5 J/cm^2 at 10, 20, and 50 Pa, both uncapped (left side) and capped (right side).

From the investigation of the optical spectra (which are reported in Fig. 4.7) of the annealed capped samples (deposited at 10, 20 and 50 Pa using a fluence 3.5 J/cm^2), we can make the following observations:

- For the capped sample deposited at 10 Pa, the optical behavior after annealing is very similar to that of the annealed uncapped counterpart (see Fig.4.2 for comparison). This seems to confirm the previously made hypothesis, according to which the structure and the optical properties of the more compact film are more affected by the thermal treatment than by the presence of a capping layer.

- For the capped sample deposited at 20 Pa, the annealing seems to improve the optical properties. The transmittance peak around 550 nm decreases and blue-shifts to ~ 480 nm. As already discussed in section 1.2, this can be associated to a lower oxygen content within the film. Moreover, the reflectance gets lower, while the absorbance gets higher. In particular, a broad and intense absorption peak centered at $\lambda \approx 780\ nm$ is obtained, with a maximum absorbance value of ~ 93 %.
  It is possible to conclude that the thermal treatment affects the optical properties of both capped and uncapped films deposited at 20 Pa, but in a different way (as it may be also observed by looking at the two films' colors, in Fig. 4.6):

  - For the uncapped sample (see Fig. 4.2) the annealing did not change much the reflectance, hence the variation in the absorbance curve was entirely due to the change in the transmittance curve.
    On the other hand, for the capped sample (see Fig. 4.7) the annealing decreased the reflectance. This may be associated to a decrease in carrier density (as discussed in section 3.1), because of either higher nitrogen or higher oxygen content within the film. In order to have a deeper understanding of the film composition, other measurements (like XPS or EDXS) should be performed.

  - For the uncapped sample (see Fig. 4.2) the annealing decreased a lot the transmittance peak and the transmittance tail at longer wavelengths, hence giving broad absorption band covering the whole Vis-NIR spectrum.
    On the other hand, for the capped sample (see Fig. 4.7) the annealing decreased the transmittance peak but did not make the transmittance tail at longer wavelengths disappear, hence giving a more defined absorption peak with a maximum located at $\lambda \approx 780\ nm$. This could be due to the fact that the capping layer may have "protected" the underlying film during the annealing. In fact, in literature the presence of a cap layer on TiN NPs was found to avoid their absorbance peak to broaden after annealing [79].

- For the capped sample deposited at 50 Pa, the reflectance does not change after annealing. Thus, considering that the transmittance slightly decreases, the

absorbance slightly increases. The variation in optical behavior before and after annealing is rather small. This may indicate that the cap layer "protects" well the underlying porous film during annealing, limiting its oxidation (as the Raman spectrum in Fig. 4.4 could suggest). As already mentioned in section 1.3, the presence of a cap layer on top of TiN NPs was found to give higher thermal stability to the optical properties of the nanoparticles [79].

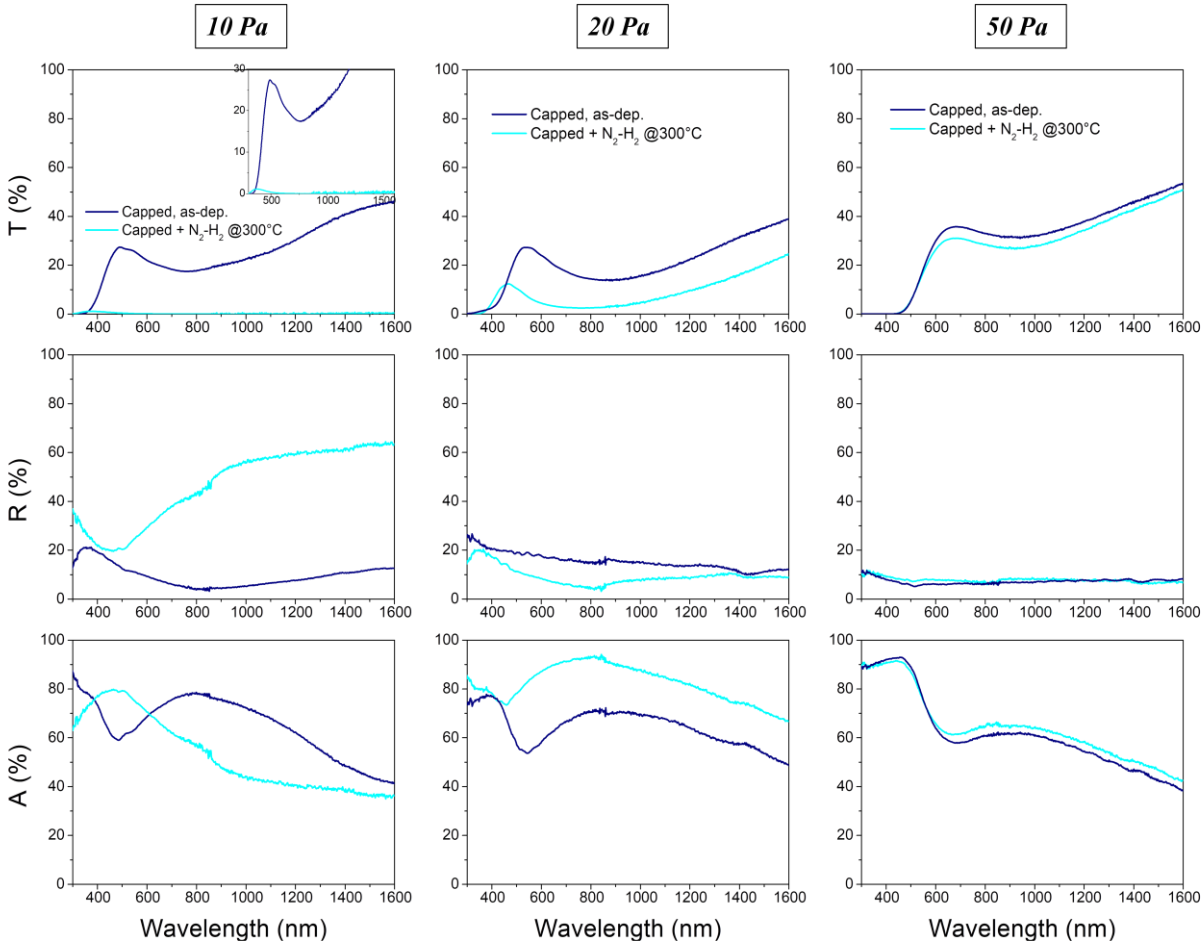

Figure 4.7: Transmittance (T), reflectance (R) and absorbance (A) of capped samples deposited with f = 3.5 J/cm^2 at 10, 20 and 50 Pa: (dark-blue lines) as-deposited; (light-blue lines) after annealing in N_2-H_2 overpressure at 300°C.

Finally, in order to have a more complete overview, we will briefly analyze also the uncapped and capped samples deposited at 50 and 100 Pa with $f = 6.5\, J/cm^2$, both before and after thermal treatment. As already discussed in section 3.2, the samples deposited with $f = 6.5\, J/cm^2$ at 50 and 100 Pa are comparable in terms of morphology and density to the samples deposited with $f = 3.5\, J/cm^2$ at 20 and 50 Pa, respectively. In Fig. 4.8 the

Raman spectra of both capped and uncapped samples deposited with f = 6.5 J/cm^2 at 50 and 100 Pa (on glass substrates) are reported, before and after annealing in N_2-H_2 overpressure at 300°C. In Fig. 4.9 the reflectance and absorbance curves of as-deposited samples deposited with f = 6.5 J/cm^2 at 50 and 100 Pa (with and without the capping layer) are shown. It should be specified that the optical curves of the samples deposited with f = 6.5 J/cm^2 after thermal annealing are not reported, since they resembled the ones of the as-deposited counterparts.
From their Raman and optical spectra we can make the following observations:

- The capping layer does not affect much neither the Raman spectra (see Fig. 4.8) nor the optical curves of the as-deposited samples. The biggest difference is the slightly higher absorbance in the visible range (see Fig. 4.9). This is due to the slightly lower reflectance in the visible range, which may be caused by an anti-reflection effect generated by the cap layer. So, the broad-band absorption obtained for the films with on top the capping layer is even more intense than that obtained for the uncapped counterparts.
  As already discussed in section 3.2, the obtained nanoporous TiN films deposited with fluence 6.5 J/cm^2 are excellent broadband absorbers, which could represent promising candidates for various exciting applications like solar cells, thermal photovoltaics and hot electron devices. The presence of the capping layer further improves these films' broadband absorption performance. Especially, such improvement can be observed for sample Cap_P100_F6.5, where maximum absorbance values of ~ 97.2 % are reached (instead of ~ 95.8 % reached for TiN_P100_F6.5). Moreover, the absorbance of Cap_P100_F6.5 stays higher than ~ 92 % in the analyzed wavelengths interval (i.e. 270-2000 nm) and its average value is ~ 96 % (while TiN_P100_F6.5 had absorbance values higher than ~ 90 % in the abovementioned wavelength interval, with an average of ~ 94.8 %).

- From the Raman spectra of annealed uncapped and capped samples (see Fig. 4.8) we can observe the formation of two peaks at wave numbers ~150 cm^{-1} and ~520 cm^{-1} , which can be associated to the crystallization of some oxynitride phases [34].
  The annealing, for both the uncapped and capped samples, does not change much the optical behavior with respect to the as-deposited counterparts. For this reason, the optical curves of the annealed samples have not been reported.

To conclude, this study on the effects of thermal treatment on the samples after the strategies against oxidation (especially the capping layer) allowed us to obtain further information regarding the variation of structural and optical properties with annealing. Moreover, by comparing the annealing effect on uncapped and capped films we could reach a deeper understanding of the utility of the capping layer. In particular, we could investigate if the films' properties were more affected by the thermal treatment or by the capping layer, and we could evaluate the effectiveness of the capping layer in "protecting" the underlying film's structure during annealing.

The structure and the optical properties of the more compact film (i.e. deposited at 10 Pa) are much more affected by the thermal treatment (whose effects were already discussed in section 4.1) than by the presence of a capping layer (see section 3.2). In fact, the properties after annealing are the same for the uncapped and the capped films. Probably, it is not necessary to protect the film deposited at 10 Pa from air exposure oxidation because it is more compact; thus, the ineffectiveness of the capping layer can be explained.

On the other side, the features of the more porous film (i.e. deposited at 50 Pa) are much more affected by the presence of a capping layer than by the annealing alone. The capping layer in fact allows (differently from the thermal treatment alone) to obtain tree-like nanostrutured TiN films instead of amorphous TiO_2. In addition, the cap layer seems to efficiently protect the underlying film, hence limiting its oxidation during the thermal annealing.

Eventually, the structure and the optical properties of the film deposited at 20 Pa (which has a density value in the middle between the other two, as shown in section 3.1) are affected by both the thermal treatment and the capping layer. More specifically, while the capping layer alone seemed to not affect much the film properties (see section 3.2), it has indeed an influence when the thermal annealing is performed. In fact, the main effect of the thermal treatment alone was to lower the transmittance peak hence giving a broadband absorption (as already discussed in section 4.1); the cap layer instead prevents such broadening of the absorbance peak by “protecting” the underlying film.

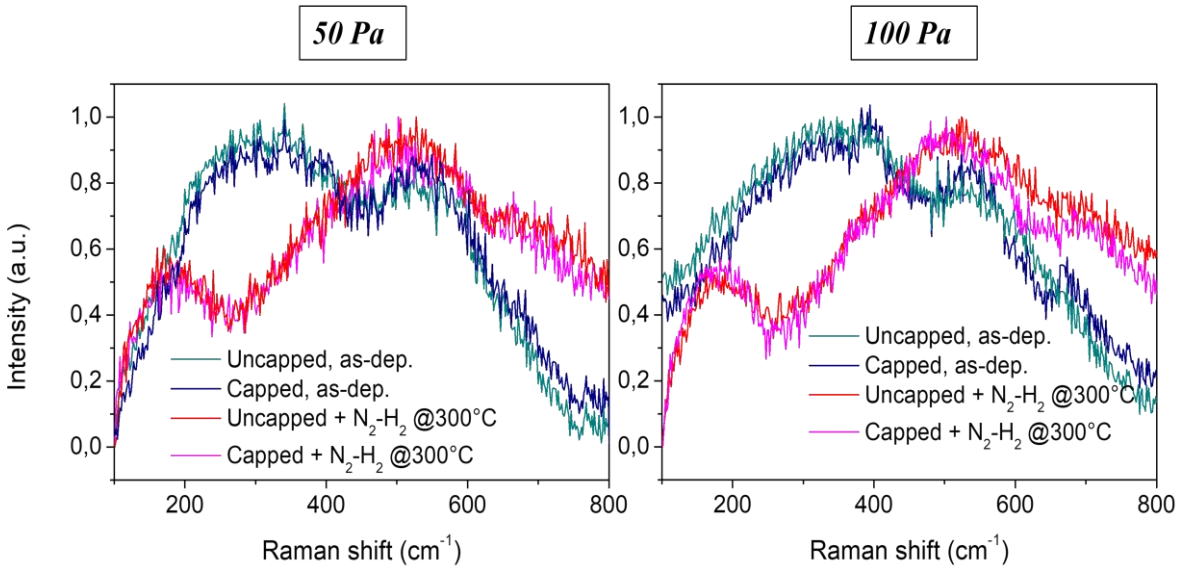

Figure 4.8: Raman spectra of both capped and uncapped samples deposited with f = 6.5 J/cm^2 at 50 and 100 Pa on glass substrates, before and after annealing in N_2-H_2 overpressure at 300°C.

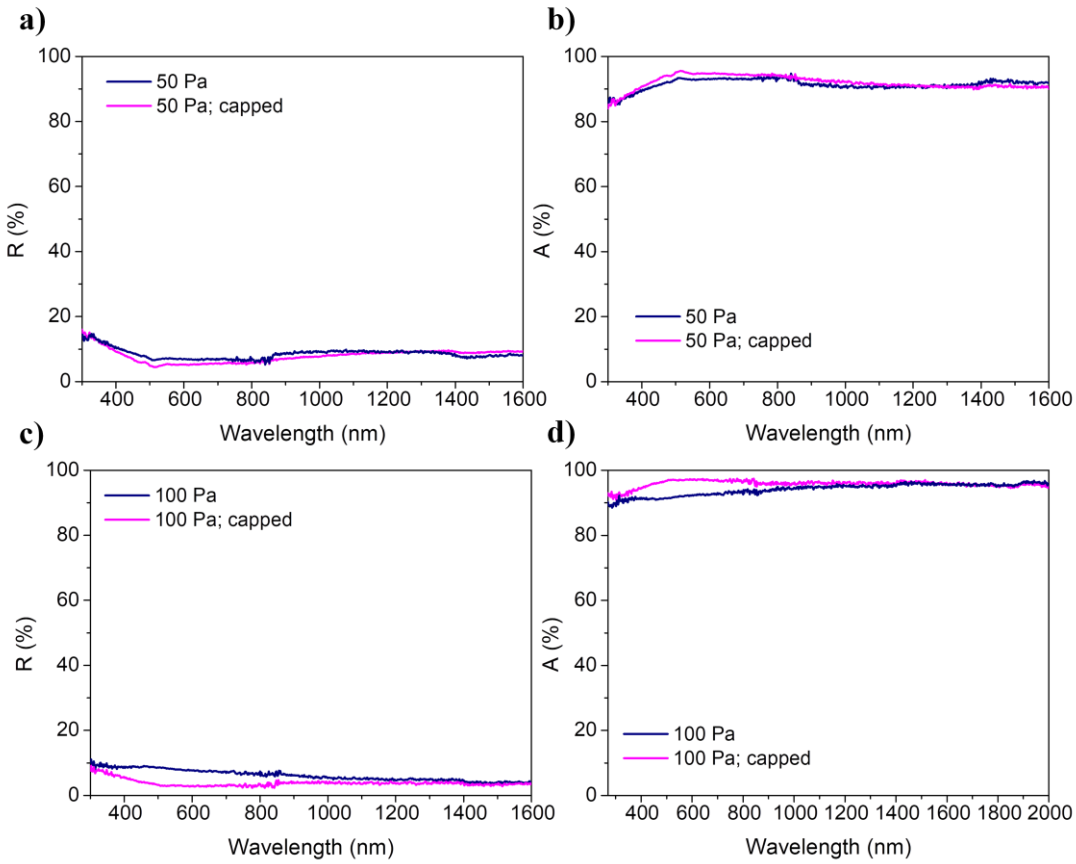

Figure 4.9: Reflectance (R) and absorbance (A) curves of samples deposited with f = 6.5 J/cm^2 at 50 and 100 Pa: (dark-blue lines) uncapped; (magenta lines) capped.

Ion Beam-Assisted Deposition of a compact TiN thin film

In this brief chapter, a first attempt of nitrogen ion beam-assisted deposition of a compact TiN thin film is presented.
The film structural, compositional, optical and electrical properties were studied and compared to those of a film deposited in the same pressure and fluence conditions but without the ion beam assist.
Moreover, the film was annealed in N_2-H_2 (at 550°C), and the variation of its main properties was investigated.
The obtained film electrical properties and stoichiometry were good if compared to the best results previously obtained by our group for TiN thin films by PLD [9]. Therefore, this deposition approach could be further developed in future studies.

We first used the RF ion source in order to produce a nitrogen ion beam which could have induced a nitridation of the fabricated TiN nanostructured films (that were analyzed in section 3.1). In this way, the nitrogen ion bombardment may have increased the nitrogen concentration within the films. However, no evident differences in Raman spectra nor in optical curves could be seen.
So, we decided to implement the RF ion source in assisting the deposition in vacuum of a compact TiN thin film with a beam of nitrogen ions, to try to increase the nitrogen incorporation within the film.

The RF ion source apparatus we used is described in section 2.1.1. In this work, the forward power was set at 300 W and the applied voltage at 380 V, giving a current of 45 mA. The N_2-H_2 gas flow was fixed at 10 sccm. Since our ion source can only work under vacuum conditions, only depositions in vacuum could be performed, hence only compact films could be produced. For this reason, the pressure in the chamber was kept at $p \sim 10^{-2}\ Pa$. Moreover, a laser fluence of $f = 2\,J/cm^2$ and a deposition time of 30 minutes were chosen. The obtained sample will be referred to as *sample IBAD_PV_F2*.

Then, sample IBAD_PV_F2 was annealed with a N_2-H_2 (95-5 %) supply at controlled overpressure of 1050 mbar, for 1 hr and with a heating ramp of 10°C/min. The annealed sample will be referred to as *sample IBAD_AN550_PV_F2*.

The two samples were analyzed with the SEM apparatus described in section 2.1. both of their cross section images (see Fig. 5.1) show a compact morphology and a thickness of 324 nm (sample IBAD_PV_F2) and 321 nm (sample IBAD_AN550_PV_F2).

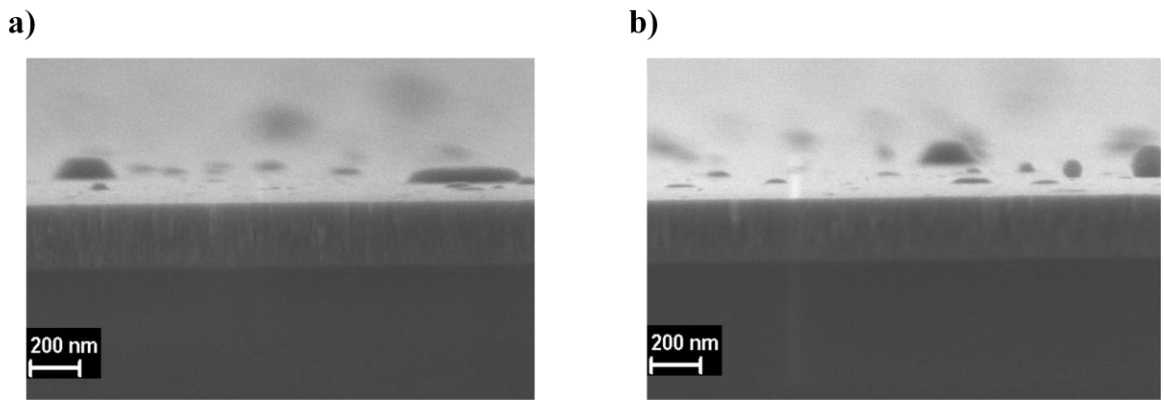

Figure 5.1: SEM cross section images of sample (a) IBAD_PV_F2 and (b) IBAD_AN550_PV_F2.

Raman spectra of the samples deposited on glass are shown in Fig. 5.2. The Raman spectrum of a film deposited in vacuum and fluence 2 J/cm^2 but without the ion beam-assist is also put as comparison. By analyzing the Raman spectrum of sample IBAD_PV_F2 (red line in Fig. 5.2) , it can be observed that the nitrogen ion beam-assist effect leads to:

- A blue-shift of the TiN acoustic band (at 200-300 cm^{-1}) towards higher Raman shifts;
- The splitting of the TiN acoustic band into two peaks, corresponding to transverse (at lower shifts) and longitudinal (at higher shifts) acoustic modes;
- The large increase in the optical band intensity (at 500-600 cm^{-1}).

All these features suggest the much bigger nitrogen concentration achieved within the film. Furthermore, by analyzing the Raman spectrum of sample IBAD_AN550_PV_F2 (green line in Fig. 5.2), it can be seen that the thermal treatment effect consist in:

- A further slight blue-shift of the TiN acoustic band (at 200-300 cm^{-1}) towards higher Raman shifts;
- The even neater separation between the transverse and longitudinal acoustic peaks;
- The even larger increase in the optical band intensity (at 500-600 cm^{-1});
- The formation of a shoulder around 550 cm^{-1}, which is associated to second order scattering of the transverse acoustic mode.

All these features suggest a nitrogen incorporation even greater than in sample IBAD_PV_F2. In particular, the appearance of the shoulder associated to second order Raman scattering indicates the fact that sample IBAD_AN550_PV_F2 is a (nearly) stoichiometric TiN [29, 31, 32]. This may find a further confirm in the fact that the acoustic and optical peaks intensity ratio is close to 1. As discussed in section 1.2 , this intensity ratio is often adopted as a way to qualitatively estimate the N/Ti ratio within the

film. However, in order to have more precise and quantitative information about the films composition, other measurements (like EDXS or XPS) should be done.

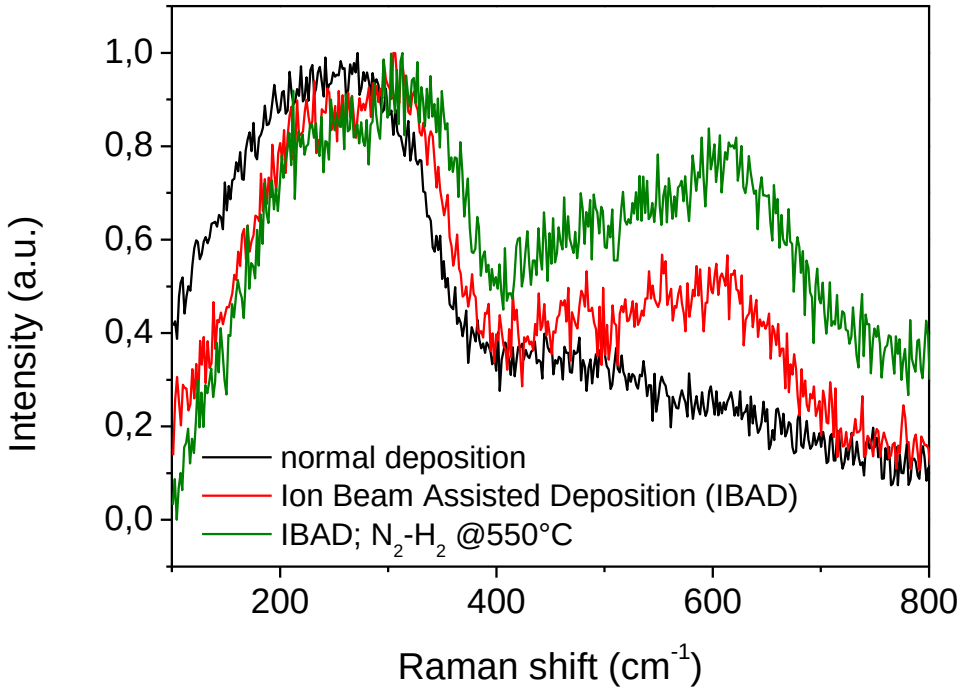

Figure 5.2: Raman spectra of TiN films deposited in vacuum at fluence 2 J/cm^2 (black line) without ion beam-assist, (red line) with ion beam-assist, and (green line) with ion-beam assist and annealed.

In Fig. 5.3 the optical spectra of samples IBAD_PV_F2 and IBAD_AN550_PV_F2 (Fig. 5.3c-d) are compared to those of sample deposited without the use of an ion beam (Fig. 5.3a-b). The curves have been obtained from spectrophotometry measurements as described in section 2.4. The narrow absorption peak, which may be associated to the surface plasmon resonance, red-shifts from $\lambda = 362\ nm$ (for sample deposited without ion beam) to $\lambda = 432\ nm$ (for sample IBAD_PV_F2) and to $\lambda = 478\ nm$ (for sample IBAD_AN550_PV_F2). Correspondingly, the reflectance dip red-shifted as well. It can be assumed that a higher nitrogen incorporation made the real part of the dielectric function (ε_1) go to zero at longer wavelengths. In fact, as discussed in section 1.2, a higher nitrogen concentration leads to a lower density of free charge carriers, hence to a red-shift of the reflectance minimum (which is associated to the plasma frequency). This may suggest that, within the films deposited with ion beam-assist, a higher N/Ti has been achieved. In particular, accordingly to Raman spectra (Fig. 5.2), the annealing in N_2-H_2 at 550°C gave an almost stoichiometric TiN film, with a N/Ti ratio close to one. Besides, its absorption peak (Fig. 5.3c) is located at $\lambda = 478\ nm$, like it is for stoichiometric TiN films (according to literature [12, 25]). Once again, it has to be pointed out that these assumptions should be verified by deeper composition analysis.

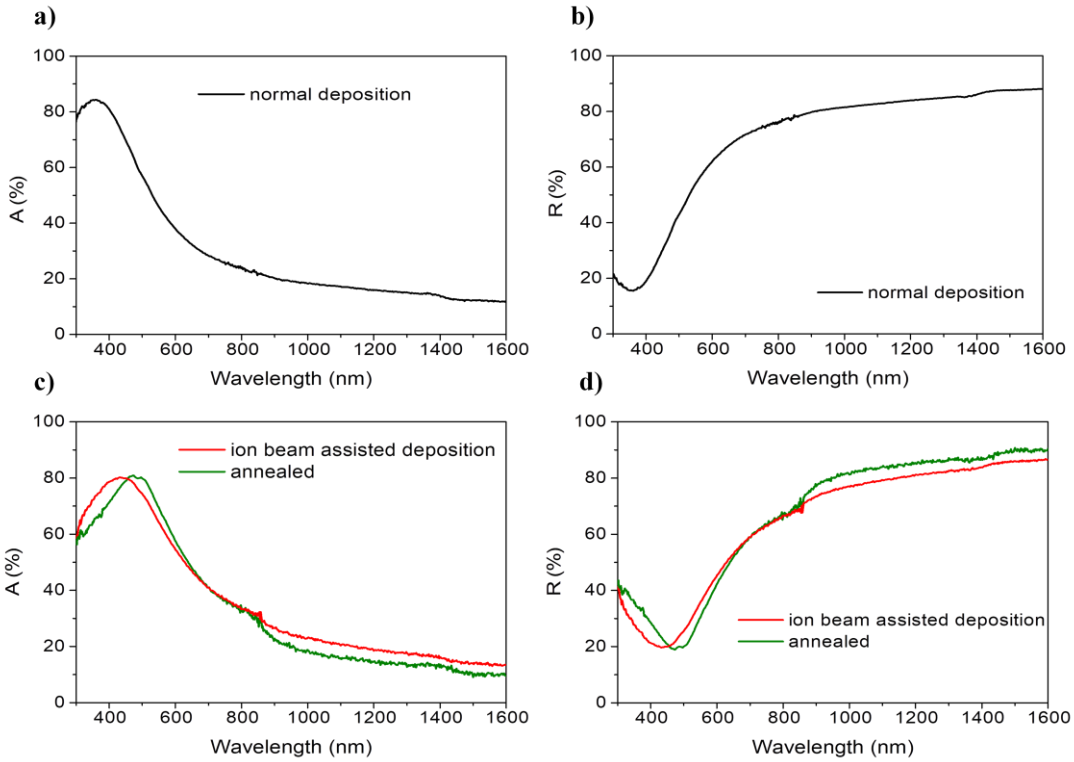

Figure 5.3: Top images: (a) absorbance and (b) reflectance curves of the sample deposited without ion beam assist. Bottom images: (a) absorbance and (b) reflectance curves of sample IBAD_ PV_F2 (red line) and IBAD_AN550_PV_F2 (green line).

Electrical resistivity measurements have been performed on the samples IBAD_PV_F2 and IBAD_AN550_PV_F2 deposited on glass using the Van der Pauw method described in section 2.6. The results from electrical measurements on the sample deposited without ion beam-assist have been taken from the work previously carried on by our group [9]. The results are presented in Tab. 5.1.

Deposition conditions	Resistivity (Ω cm)
Vacuum, *f* = 2 J/cm^2, as-dep. [9]	$2.8 \cdot 10^{-4} \pm 3.1 \cdot 10^{-6}$
IBAD, vacuum, *f* = 2 J/cm^2, as-dep.	$2.8 \cdot 10^{-4}$
IBAD, vacuum, *f* = 2 J/cm^2, N_2-H_2 @550°C	$2.8 \cdot 10^{-4} \pm 3.2 \cdot 10^{-8}$

Table 5.1: Resistivity values of sample deposited without ion assist compared to those of samples IBAD_ PV_F2 and IBAD_AN550_PV_F2.

It is clear that neither ion beam-assist nor annealing managed to improve the TiN film resistivity, whose value remained unchanged. Only an improvement in the standard deviation of the data is observed, which decreases by two orders of magnitude. It should be

specified that the data regarding sample IBAD_PV_F2 resistivity's standard deviation are missing; however, it is likely that such standard deviation values would lay between 10^{-6} and 10^{-8}.
In general, the measured values are one order of magnitude higher than the best results found in literature [109, 110, 111].
The results of Hall measurements were not reported for all the samples, since the obtained data were often unreliable. In fact, a parameter called Figure of Merit (FoM) can be defined, which provides an indication of the error on the measured carrier density:

$$FoM = \frac{zero_check}{V_h}$$

where $zero_check$ is the reference potential measured with no applied magnetic field, averaged over the four possible configurations discussed in section 2.6; V_h is the sum of the four terms $(V_+ - V_-)$, one for each configurations (while V_+ and V_- are the voltages measured between the same two contacts, but with the magnetic field oriented in opposite directions). Ideally, $zero_check$ should be zero. Thus, for non-ideal systems, this term must be as small as possible, or at least much smaller than V_h. In order to have reliable data, the FoM must be smaller than 1 (and preferably close to zero).
For the sample deposited without ion beam and for sample IBAD_PV_F2 the Hall measurements were not reported, because $FoMs > 1$ were obtained. On the other hand, for sample IBAD_AN550_PV_F2 the FoM was small enough to consider the obtained data reliable, hence the density of carriers and Hall mobility could be calculated and reported in Tab. 5.2.

Sample name	Figure of Merit	Charge carrier density n (cm^{-3})	Hall mobility μ ($cm^2/V\cdot s$)
IBAD_AN550_PV_F2	0.103	$4.86\cdot10^{22} \pm 2.94\cdot10^{21}$	0.46 ± 0.03

Table 5.2: Hall measurements for sample IBAD_AN550_PV_F2.

The obtained $n = 4.86 \cdot 10^{22}\text{cm}^{-3}$ for sample IBAD_AN550_PV_F2 is a rather high value (and with a small error bar), comparable to the best values obtained in literature. In particular, the highest n value obtained by PLD (by heating the substrate at 700°C) is $n \sim 4.5 \cdot 10^{22}\text{cm}^{-3}$ [111], while for sputtered single crystal film is $n \sim 5 \cdot 10^{22}\text{cm}^{-3}$ [112], and the theoretical conduction electron density is $n \sim 5.25 \cdot 10^{22}\text{cm}^{-3}$ [113].
The Hall mobility obtained for sample IBAD_AN550_PV_F2 has a rather low value, probably because of the TiN film's polycrystalline structure characterized by small grains and by many defects.

Conclusions and perspectives

This thesis work investigated the synthesis and characterization of titanium nitride nanostructured thin films in the perspective of potential applications in the field of plasmonics. In particular, the relation between the deposition conditions and the films morphology, structure and optical properties was explored. In fact, one of the potential advantages of TiN over conventional plasmonic materials (like gold and silver) is the possibility of tuning its optical behavior by playing with its structure and composition, which are determined by the synthesis parameters. A strong focus was put on the oxidation problem and on its consequences on the film synthesis and plasmonic behavior.

First, we performed Pulsed Laser Deposition (PLD) of TiN films on Si and glass substrates at room temperature, exploring different combinations of laser energy density (fluence, 2 and 3.5 J/cm^2) and background N_2-H_2 gas pressures (5, 10, 20, 50 and 100 Pa), in order to obtain optimum conditions for the deposition of uniform and adherent nanostructured films. This study on the effect of pressure and fluence allowed us to obtain information on the morphology, qualitative composition and optical properties of the TiN films. In particular, keeping a constant fluence, it is possible, by increasing the pressure from 5 to 100 Pa, to move from compact-columnar to tree-like nanostructured films, and eventually to foams. The films density values at the various deposition conditions, which have been obtained from quartz crystal microbalance (QCM) measurements, showed a rather linear decrease with increasing pressure. On the other hand, at constant pressure, a higher laser energy density leads to a more compact structure and to higher film density values. Furthermore, pressure plays an important role in modifying the film composition, since higher *p* seems to favor either nitrogen incorporation or oxide phases formation.
From the beginning of the work, we dealt with serious oxidation issues, especially for the more porous samples, whose high surface area makes them more prone to oxygen contamination. In particular, films with a density lower than a certain threshold value resembled amorphous titanium oxide rather than titanium nitride. In order to reduce the oxygen incorporation within these samples, thus managing to obtain TiN films with lower densities, two strategies have been adopted:

a) We deposited 200 nm thick aluminum nitride diffusion barriers (*capping layers*) on top of the nanoporous films without opening the vacuum chamber, to try to hinder surface oxidation due to air exposure. Such capping layers were effective in reducing oxidation within the more porous samples, which were characterized by a tree-like nanostructured morphology (i.e. samples deposited at 50 Pa). In fact, while the uncapped samples showed an amorphous TiO_2 Raman signal and very high transparency and low absorbance in the Vis-NIR, the capped samples instead

showed the typical TiN Raman spectrum and featured an intra-band absorption peak located in the near-infrared (centered at $\lambda \cong 925\ nm$).

b) We performed depositions at higher fluence (6.5 J/cm^2) in order to try to reduce oxygen incorporation during deposition. In fact, a higher energy per pulse may lead to higher nitrogen gas molecules dissociation, hence to higher nitrogen radicals reactivity in the plasma plume. While the films (with comparable density and morphology) deposited at fluences 2 and 3.5 J/cm^2 were amorphous TiO_2, the ones deposited at fluence 6.5 J/cm^2 were likely tree-like nanostructured TiO_xN_y films (as suggested by Raman spectra analysis) showing very high and broadband absorption all over the UV-Vis-NIR spectrum. Therefore, these films could be promising candidates for applications like solar energy harvesting and hot electron devices.

Subsequently, we studied the effect of different annealing atmospheres (vacuum and N_2-H_2 overpressure) and temperatures (300 and 550°C) on the uncapped samples deposited with fluence 3.5 J/cm^2 at 10, 20 and 50 Pa. The annealing time was set constant at 1 hr. Our goal was to favor the desorption of surface oxygen, while improving the crystallization of TiN. Moreover, we expected the annealing in N_2-H_2 overpressure to enrich the films in nitrogen. The following main results were obtained:

- The annealing in vacuum and in N_2-H_2 overpressure at 550°C made the structural and optical properties of the films (especially of the more porous, i.e. deposited at 20 and 50 Pa) more similar to those of TiO_2 rather than of TiN. We associated this to an increase of the oxidation extent within the films. Possibly, the high quantity of oxygen previously adsorbed at the surface upon air-exposure led to oxidation of the samples during annealing. Moreover, the high temperature (550°C) may have favored the oxidation reactions.

- After annealing in N_2-H_2 overpressure at 300°C, the Raman spectra of samples deposited at 10 and 20 Pa indicated a higher TiN crystallization and a lower presence of TiO_2 phases. Moreover, the transmittance peak of these samples significantly reduced in intensity and blue-shifted (from $\lambda \cong 500\ nm$ to $\lambda \cong 380\ nm$ and from $\lambda \cong 550\ nm$ to $\lambda \cong 480\ nm$, respectively). We ascribed this behavior to a reduced oxygen content within the films after thermal treatment.

- For the more porous films (i.e. deposited at 50 Pa), none of the adopted thermal treatments led to the formation of TiN, but of either amorphous or crystalline TiO_2.

- Contrary to what expected, no evidence of higher nitrogen incorporation within the films annealed in N_2-H_2 overpressure was found.

Then, we carried out thermal treatments of 1 hr in N_2-H_2 overpressure at 300°C on samples after adopting the strategies against oxidation (i.e. on samples with capping layer and on samples deposited at fluence 6.5 J/cm^2). Our goal was to analyze the influence of such

strategies on the behavior of the film during thermal annealing. In particular, we wanted to evaluate the effectiveness of the capping layer in protecting the underlying film from thermal oxidation. The main obtained results are listed below:

- The structure and optical properties of the more compact film deposited at 10 Pa after thermal treatment are the same for both uncapped and capped samples. Thus, it is probably not necessary to protect such film from air exposure oxidation because it is more compact.

- The optical behavior of the more porous capped film (deposited at 50 Pa) do not change after annealing. Therefore, the capping layer seems to efficiently protect the underlying film from air-exposure oxygen contamination, limiting its oxidation during thermal annealing.

- For the samples deposited at higher fluence (6.5 J/cm^2), both capped and uncapped, the optical properties do not change after annealing, while the Raman spectra show the formation of two peaks that can be related to the presence of oxynitride phases.

Finally, in the last part of this thesis work a first attempt of nitrogen ion beam assisted deposition was performed, in order to try to obtain a compact TiN thin film with a high nitrogen content. Besides, the effect of annealing in N_2-H_2 overpressure at 550°C on the obtained film was studied. The resulting annealed film's electrical properties and stoichiometry were very good if compared to the best results previously obtained by our group for TiN thin films by PLD [49]. Therefore, this deposition approach could be further developed in future studies.

The most relevant achievements of this work thesis can be summarized as follows:

1. The successful fabrication by PLD of uniform and adherent nanostructured TiN thin films on glass and Si substrates at room temperature. In particular, we were able to overcome the severe oxidation issues involving the highly porous tree-like nanostructured films by depositing a protective capping layer on top of them, or alternatively by using a higher laser fluence during deposition.

2. We correlated the effects of deposition parameters like fluence and background pressure with the morphology, structure and optical properties of the obtained samples.

3. We correlated the effects of post-growth annealing conditions with the structure and optical properties of the obtained samples.

4. We established the existence of a strong influence (for the more porous samples) of the capping layer on the optical properties variation upon annealing.

However, to achieve better knowledge and control of the optical and plasmonic properties of nanostructured TiN thin films there is still a long way to go. For example, it is still needed to understand more deeply the influence of deposition and annealing conditions on the film stoichiometry and composition. In fact, Raman spectroscopy data are not of easy interpretation, since the Raman signal of TiN is activated by defects; thus, they can only give qualitative indications of the film structure. In order to perform a deep investigation of the film composition and stoichiometry, other characterization techniques would be needed, e.g. XPS or EDXS. Moreover, we were not able to measure the charge carrier density of our nanostructured films. Knowing the charge carrier densities would be crucial in order to verify the interpretations of the optical behavior. In fact, the parameter characterizing the plasmonic response of a material (i.e. the plasma frequency) mostly depends on the free carrier concentration. Besides, XRD measurements would be useful in order to verify the presence of crystalline TiN, TiO_xN_y or TiO_2 phases within the samples before and after annealing. Lastly, in order to have a clearer distinction between plasmonic and inter-band absorptions within the more compact films, ellipsometry measurements would be extremely useful.

The long terms perspectives include:

- Developing the growth of compact TiN thin films by Ion Beam Assisted Deposition, in order to try to obtain TiN films with good stoichiometry, low electrical resistivity, high mobility, and with the possibility to tune their N/Ti ratio and consequently their plasmonic response.

- Studying more deeply the tree-like nanostructured TiO_xN_y films obtained with fluence 6.5 J/cm^2 and characterized by broadband absorption. In particular, different annealing conditions may be explored. Moreover, in a long-term view, the design of devices able to incorporate such films is necessary.

- Varying the thickness of the capping layer, to study more deeply its influence on the plasmonic behavior of the underlying nanoporous TiN films.

- Developing the innovative setup adopted for the deposition of capped TiN films in order to fabricate multilayered structures made of alternating (either compact or porous) TiN and AlN layers, acting as conductive and dielectric layer, respectively. This could be one route to synthesize TiN-based hyperbolic metamaterials.

- Performing nitrogen ion implantation in the nanoporous TiN films (using the RF ion source integrated in the PLD apparatus), in order to try to enrich them in nitrogen, and with the possibility to tune their N/Ti ratio and consequently their plasmonic response.

Bibliography

[1] Maier, S. A. (2007). "*Plasmonics: fundamentals and applications"*. Springer Science & Business Media.

[2] Naik, G. V., Shalaev, V. M., & Boltasseva, A. (2013). "Alternative plasmonic materials: beyond gold and silver". *Advanced Materials*, *25*(24), 3264-3294.

[3] Guler, U., Shalaev, V. M., & Boltasseva, A. (2015). "Nanoparticle plasmonics: going practical with transition metal nitrides". *Materials Today*, *18*(4), 227-237.

[4] Kaisar, N., Huang, Y. T., Jou, S., Kuo, H. F., Huang, B. R., Chen, C. C., ... & Chung, Y. C. (2018). "Surface-enhanced Raman scattering substrates of flat and wrinkly titanium nitride thin films by sputter deposition". *Surface and Coatings Technology*, *337*, 434-438.

[5] Podder, S., & Pal, A. R. (2019). "Hot carrier devices using visible and NIR responsive titanium nitride nanostructures with stoichiometry variation". *Optical Materials*, *97*, 109379.

[6] Liu, F., Yang, X., Dang, D., & Tian, X. (2019). "Engineering of Hierarchical and Three-Dimensional Architectures Constructed by Titanium Nitride Nanowire Assemblies for Efficient Electrocatalysis". *ChemElectroChem*, *6*(8), 2208-2214.

[7] Naik, G. V., Schroeder, J. L., Ni, X., Kildishev, A. V., Sands, T. D., & Boltasseva, A. (2012). "Titanium nitride as a plasmonic material for visible and near-infrared wavelengths". *Optical Materials Express*, *2*(4), 478-489.

[8] Guler, U., Ndukaife, J. C., Naik, G. V., Nnanna, A. A., Kildishev, A. V., Shalaev, V. M., & Boltasseva, A. (2013). "Local heating with lithographically fabricated plasmonic titanium nitride nanoparticles". *Nano letters*, *13*(12), 6078-6083.

[9] Garattoni S. "Synthesis of titanium nitride thin films with tunable optical and electrical properties". MA thesis. Politecnico di Milano, 2019.

[10] Mascaretti, L., Ferrulli, S., Mazzolini, P., Casari, C. S., Russo, V., Matarrese, R., ... & Li Bassi, A. (2017). "Hydrogen-treated hierarchical titanium

oxide nanostructures for photoelectrochemical water splitting". *Solar Energy Materials and Solar Cells*, *169*, 19-27.

[11] Lee, T., Delley, B., Stampfl, C., & Soon, A. (2012). "Environment-dependent nanomorphology of TiN: the influence of surface vacancies". *Nanoscale*, *4*(16), 5183-5188.

[12] Patsalas, P., Kalfagiannis, N., Kassavetis, S., Abadias, G., Bellas, D. V., Lekka, C., & Lidorikis, E. J. M. S. (2018). "Conductive nitrides: Growth principles, optical and electronic properties, and their perspectives in photonics and plasmonics". *Materials Science and Engineering: R: Reports*, *123*, 1-55.

[13] Kim, S. H., Park, H., Lee, K. H., Jee, S. H., Kim, D. J., Yoon, Y. S., & Chae, H. B. (2009). "Structure and mechanical properties of titanium nitride thin films grown by reactive pulsed laser deposition". *Journal of Ceramic Processing Research*, *10*(1), 49-53.

[14] Peng, Z., Miao, H., Qi, L., Yang, S., & Liu, C. (2003). "Hard and wear-resistant titanium nitride coatings for cemented carbide cutting tools by pulsed high energy density plasma". *Acta Materialia*, *51*(11), 3085-3094.

[15] Niyomsoan, S., Grant, W., Olson, D. L., & Mishra, A. B. (2002). "Variation of color in titanium and zirconium nitride decorative thin films". *Thin Solid Films*, *415*(1-2), 187-194.

[16] Tang, T., Wei, C. C., Haken, R., Holloway, T., Wan, C. F., & Douglas, M. (1985, December). "VLSI local interconnect level using titanium nitride". In *1985 International Electron Devices Meeting* (pp. 590-593). IEEE.

[17] Ruterana, P., Nouet, G., Kehagias, T., Komninou, P., Karakostas, T., di Forte Poisson, M. A., ... & Morkoc, H. (1999). "The microstructure of Ti/Al and TiN ohmic contacts to gallium nitride". *physica status solidi (a)*, *176*(1), 767-771.

[18] Serro, A. P., Completo, C., Colaço, R., Dos Santos, F., Da Silva, C. L., Cabral, J. M. S., ... & Saramago, B. (2009). "A comparative study of titanium nitrides, TiN, TiNbN and TiCN, as coatings for biomedical applications". *Surface and Coatings Technology*, *203*(24), 3701-3707.

[19] Patsalas, P., Charitidis, C., Logothetidis, S., Dimitriadis, C. A., & Valassiades, O. (1999). "Combined electrical and mechanical properties of titanium nitride thin films as metallization materials". *Journal of applied physics*, *86*(9), 5296-5298.

[20] Dimitriadis, C. A., Logothetidis, S., & Alexandrou, I. (1995). “Schottky barrier contacts of titanium nitride on n-type silicon”. *Applied physics letters*, *66*(4), 502-504.

[21] Kumar, M., Umezawa, N., Ishii, S., & Nagao, T. (2016). “Examining the performance of refractory conductive ceramics as plasmonic materials: a theoretical approach”. *ACS Photonics*, *3*(1), 43-50.

[22] Patsalas, P., & Logothetidis, S. (2001). “Optical, electronic, and transport properties of nanocrystalline titanium nitride thin films”. *Journal of Applied Physics*, *90*(9), 4725-4734.

[23] Shan, W., Walukiewicz, W., Yu, K. M., Ager III, J. W., Haller, E. E., Geisz, J. F., ... & Nauka, C. (2000). “Effect of nitrogen on the electronic band structure of group III-NV alloys”. *Physical Review B*, *62*(7), 4211.

[24] Patsalas, P., Kalfagiannis, N., & Kassavetis, S. (2015). “Optical properties and plasmonic performance of titanium nitride”. *Materials*, *8*(6), 3128-3154.

[25] Sugavaneshwar, R. P., Ishii, S., Dao, T. D., Ohi, A., Nabatame, T., & Nagao, T. (2017). “Fabrication of highly metallic TiN films by pulsed laser deposition method for plasmonic applications”. *ACS Photonics*, *5*(3), 814-819.

[26] Zhao, G., Zhang, T., Zhang, T., Wang, J., & Han, G. (2008). “Electrical and optical properties of titanium nitride coatings prepared by atmospheric pressure chemical vapor deposition”. *Journal of non-crystalline solids*, *354*(12-13), 1272-1275.

[27] Lousa, A., Esteve, J., Mejia, J. P., & Devia, A. (2007). “Influence of deposition pressure on the structural mechanical and decorative properties of TiN thin films deposited by cathodic arc evaporation”. *Vacuum*, *81*(11-12), 1507-1510.

[28] Paulitsch, J., Schenkel, M., Zufraß, T., Mayrhofer, P. H., & Münz, W. D. (2010). “Structure and properties of high power impulse magnetron sputtering and DC magnetron sputtering CrN and TiN films deposited in an industrial scale unit”. *Thin Solid Films*, *518*(19), 5558-5564.

[29] Trenczek-Zajac, A., Radecka, M., Zakrzewska, K., Brudnik, A., Kusior, E., Bourgeois, S., ... & Imhoff, L. (2009). “Structural and electrical properties of magnetron sputtered Ti (ON) thin films: the case of TiN doped in situ with oxygen”. *Journal of Power Sources*, *194*(1), 93-103.

[30] Guillot, J., Jouaiti, A., Imhoff, L., Domenichini, B., Heintz, O., Zerkout, S., ... & Bourgeois, S. (2002). “Nitrogen plasma pressure influence on the composition of TiNxOy sputtered films”. *Surface and Interface Analysis: An International Journal devoted to the development and application of techniques for the analysis of surfaces, interfaces and thin films*, *33*(7), 577-582.

[31] Spengler, W., Kaiser, R., Christensen, A. N., & Müller-Vogt, G. (1978). “Raman scattering, superconductivity, and phonon density of states of stoichiometric and nonstoichiometric TiN”. *physical review b*, *17*(3), 1095.

[32] Constable, C. P., Yarwood, J., & Münz, W. D. (1999). “Raman microscopic studies of PVD hard coatings”. *Surface and Coatings Technology*, *116*, 155-159.

[33] Radecka, M., Pamula, E., Trenczek-Zajac, A., Zakrzewska, K., Brudnik, A., Kusior, E., ... & Balogh, A. G. (2011). “Chemical composition, crystallographic structure and impedance spectroscopy of titanium oxynitride TiNxOy thin films”. *Solid State Ionics*, *192*(1), 693-698.

[34] Padmavathy, P., Ananthakumar, R., Subramanian, B., Ravidhas, C., & Jayachandran, M. (2011). “Structural and electrochemical impedance spectroscopic studies on reactive magnetron sputtered titanium oxynitride (TiON) thin films”. *Journal of Applied Electrochemistry*, *41*(6), 751.

[35] Sousa, R. R. M. D., Araújo, F. O. D., Costa, T. H. D. C., Nascimento, I. O., Santos, F. E. P., Alves Júnior, C., & Feitor, M. C. (2015). “Thin TiN and TiO2 film deposition in glass samples by cathodic cage”. *Materials Research*, *18*(2), 347-352.

[36] Ernsberger, C., Nickerson, J., Smith, T., Miller, A. E., & Banks, D. (1986). “Low temperature oxidation behavior of reactively sputtered TiN by X-ray photoelectron spectroscopy and contact resistance measurements”. *Journal of Vacuum Science & Technology A: Vacuum, Surfaces, and Films*, *4*(6), 2784-2788.

[37] Milošev, I., Strehblow, H. H., & Navinšek, B. (1997). “Comparison of TiN, ZrN and CrN hard nitride coatings: Electrochemical and thermal oxidation”. *Thin solid films*, *303*(1-2), 246-254.

[38] Achour, A., Porto, R. L., Soussou, M. A., Islam, M., Boujtita, M., Aissa, K. A., ... & Brousse, T. (2015). “Titanium nitride films for micro-supercapacitors: effect of surface chemistry and film morphology on the capacitance”. *Journal of Power Sources*, *300*, 525-532.

[39] Yin, Y., Hang, L., Zhang, S., & Bui, X. L. (2007). “Thermal oxidation properties of titanium nitride and titanium–aluminum nitride materials—A

perspective for high temperature air-stable solar selective absorber applications". *Thin Solid Films*, *515*(5), 2829-2832.

[40] Achour, A., Chaker, M., Achour, H., Arman, A., Islam, M., Mardani, M., ... & Brousse, T. (2017). "Role of nitrogen doping at the surface of titanium nitride thin films towards capacitive charge storage enhancement". *Journal of Power Sources*, *359*, 349-354.

[41] Tarniowy, A., Mania, R., & Rekas, M. (1997). "The effect of thermal treatment on the structure, optical and electrical properties of amorphous titanium nitride thin films". *Thin Solid Films*, *311*(1-2), 93-100.

[42] Kavitha, A., Kannan, R., Reddy, P. S., & Rajashabala, S. (2016). "The effect of annealing on the structural, optical and electrical properties of Titanium Nitride (TiN) thin films prepared by DC magnetron sputtering with supported discharge". *Journal of Materials Science: Materials in Electronics*, *27*(10), 10427-10434.

[43] Xi, Y., Fan, H., & Liu, W. (2010). "The effect of annealing treatment on microstructure and properties of TiN films prepared by unbalanced magnetron sputtering". *Journal of alloys and compounds*, *496*(1-2), 695-698.

[44] Bittar, A., Cochrane, D., Caughley, S., & Vickeridge, I. (1997). "Study of TiOxNy thin film selective surfaces produced by ion assisted deposition". *Journal of Vacuum Science & Technology A: Vacuum, Surfaces, and Films*, *15*(2), 223-229.

[45] Lu, F. H., & Chen, H. Y. (1999). "XPS analyses of TiN films on Cu substrates after annealing in the controlled atmosphere". *Thin Solid Films*, *355*, 374-379.

[46] Wang, J. M., Liu, W. G., & Mei, T. (2004). "The effect of thermal treatment on the electrical properties of titanium nitride thin films by filtered arc plasma method". *Ceramics international*, *30*(7), 1921-1924.

[47] Huang, J. H., Yu, K. J., Sit, P., & Yu, G. P. (2006). "Heat treatment of nanocrystalline TiN films deposited by unbalanced magnetron sputtering". *Surface and Coatings Technology*, *200*(14-15), 4291-4299.

[48] Subramanian, B., & Jayachandran, M. (2007). "Characterization of reactive magnetron sputtered nanocrystalline titanium nitride (TiN) thin films with brush plated Ni interlayer". *Journal of applied electrochemistry*, *37*(9), 1069-1075.

[49] Rasic, D., Sachan, R., Chisholm, M. F., Prater, J., & Narayan, J. (2017). "Room temperature growth of epitaxial titanium nitride films by pulsed laser deposition". *Crystal Growth & Design*, *17*(12), 6634-6640.

[50] Mihailescu, I. N., Gyorgy, E., Chitica, N., Teodorescu, V. S., Mavin, G., Luches, A., ... & Neamtu, J. (1996). "A parametric study of the deposition of the TiN thin films by laser reactive ablation of titanium targets in nitrogen: the roles of the total gas pressure and the contaminations with oxides". *Journal of materials science*, *31*(11), 2909-2915.

[51] Gu, H. D., Leung, K. M., Chung, C. Y., & Han, X. D. (1998). "Room-temperature growth of high-purity titanium nitride by laser ablation of titanium in a nitrogen atmosphere". *Surface and Coatings Technology*, *110*(3), 153-157.

[52] Krishnan, R., Mathews, T., Balamurugan, A. K., Dash, S., Tyagi, A. K., Raj, B., & Jayaram, V. (2010). "Reactive Pulsed Laser Deposition of titanium nitride thin film: Optimization of process parameters using Secondary Ion Mass Spectrometry". *Applied surface science*, *256*(10), 3077-3080.

[53] Craciun, D., Socol, G., Stefan, N., Dorcioman, G., Hanna, M., Taylor, C. R., ... & Craciun, V. (2014). "The effect of deposition atmosphere on the chemical composition of TiN and ZrN thin films grown by pulsed laser deposition". *Applied Surface Science*, *302*, 124-128.

[54] Guo, H., Chen, W., Shan, Y., Wang, W., Zhang, Z., & Jia, J. (2015). "Microstructures and properties of titanium nitride films prepared by pulsed laser deposition at different substrate temperatures". *Applied Surface Science*, *357*, 473-478.

[55] Marhaba, S. (2017). "Effect of Size, Shape and Environment on the Optical Response of Metallic Nanoparticles". In *Noble and Precious Metals-Properties, Nanoscale Effects and Applications*. IntechOpen.

[56] Faraday, M. (1857). X. The Bakerian Lecture. "Experimental relations of gold (and other metals) to light". *Philosophical Transactions of the Royal Society of London*, (147), 145-181.

[57] Romo-Herrera, J. M., Alvarez-Puebla, R. A., & Liz-Marzán, L. M. (2011). "Controlled assembly of plasmonic colloidal nanoparticle clusters". *Nanoscale*, *3*(4), 1304-1315.

[58] Smith, A. M., Mancini, M. C., & Nie, S. (2009). "Bioimaging: second window for in vivo imaging". *Nature nanotechnology*, *4*(11), 710.

[59] Hirsch, L. R., Stafford, R. J., Bankson, J. A., Sershen, S. R., Rivera, B., Price, R. E., ... & West, J. L. (2003). "Nanoshell-mediated near-infrared thermal therapy of tumors under magnetic resonance guidance". *Proceedings of the National Academy of Sciences*, *100*(23), 13549-13554.

[60] Baffou, G., Quidant, R., & Girard, C. (2009). "Heat generation in plasmonic nanostructures: Influence of morphology". *Applied Physics Letters*, *94*(15), 153109.

[61] Nehl, C. L., Liao, H., & Hafner, J. H. (2006). "Optical properties of star-shaped gold nanoparticles". *Nano letters*, *6*(4), 683-688.

[62] Radloff, C., & Halas, N. J. (2001). "Enhanced thermal stability of silica-encapsulated metal nanoshells". *Applied Physics Letters*, *79*(5), 674-676.

[63] Bobb, D. A., Zhu, G., Mayy, M., Gavrilenko, A. V., Mead, P., Gavrilenko, V. I., & Noginov, M. A. (2009). "Engineering of low-loss metal for nanoplasmonic and metamaterials applications". *Applied Physics Letters*, *95*(15), 151102.

[64] Wu, P. C., Kim, T. H., Suvorova, A., Giangregorio, M., Saunders, M., Bruno, G., ... & Losurdo, M. (2011). "GaMg alloy nanoparticles for broadly tunable plasmonics". *Small*, *7*(6), 751-756.

[65] Freestone, I., Meeks, N., Sax, M., & Higgitt, C. (2007). "The Lycurgus cup: a roman nanotechnology". *Gold bulletin*, *40*(4), 270-277.

[66] Loo, C., Lin, A., Hirsch, L., Lee, M. H., Barton, J., Halas, N., ... & Drezek, R. (2004). "Nanoshell-enabled photonics-based imaging and therapy of cancer". *Technology in cancer research & treatment*, *3*(1), 33-40.

[67] Ayala-Orozco, C., Urban, C., Knight, M. W., Urban, A. S., Neumann, O., Bishnoi, S. W., ... & Shea, M. (2014). "Au nanomatryoshkas as efficient near-infrared photothermal transducers for cancer treatment: benchmarking against nanoshells". *ACS nano*, *8*(6), 6372-6381.

[68] Huang, P., Lin, J., Li, W., Rong, P., Wang, Z., Wang, S., ... & Leapman, R. D. (2013). "Biodegradable gold nanovesicles with an ultrastrong plasmonic coupling effect for photoacoustic imaging and photothermal therapy". *Angewandte Chemie International Edition*, *52*(52), 13958-13964.

[69] Gao, H., Peng, W., Cui, W., Chu, S., Yu, L., & Yang, X. (2019). "Ultraviolet to near infrared titanium nitride broadband plasmonic absorber". *Optical Materials*, *97*, 109377.

[70] Ishii, S., Sugavaneshwar, R. P., & Nagao, T. (2016). "Titanium nitride nanoparticles as plasmonic solar heat transducers". *The Journal of Physical Chemistry C*, *120*(4), 2343-2348.

[71] Guler, U., Kildishev, A. V., Boltasseva, A., & Shalaev, V. M. (2015). "Plasmonics on the slope of enlightenment: the role of transition metal nitrides". *Faraday discussions*, *178*, 71-86.

[72] Clatworthy, E. B., Yick, S., Murdock, A. T., Allison, M. C., Bendavid, A., Masters, A. F., & Maschmeyer, T. (2019). "Enhanced Photocatalytic Hydrogen Evolution with TiO_2–TiN Nanoparticle Composites". *The Journal of Physical Chemistry C*, *123*(6), 3740-3749.

[73] Li, J., Gao, L., Sun, J., Zhang, Q., Guo, J., & Yan, D. (2001). "Synthesis of nanocrystalline titanium nitride powders by direct nitridation of titanium oxide". *Journal of the American Ceramic Society*, *84*(12), 3045-3047.

[74] Tavares, J., Coulombe, S., & Meunier, J. L. (2009). "Synthesis of cubic-structured monocrystalline titanium nitride nanoparticles by means of a dual plasma process". *Journal of Physics D: Applied Physics*, *42*(10), 102001.

[75] Kumar, S. M., Murugan, K., Chandrasekhar, S. B., Hebalkar, N., Krishna, M., Satyanarayana, B. S., & Madras, G. (2012). "Synthesis and characterization of nano silicon and titanium nitride powders using atmospheric microwave plasma technique". *Journal of Chemical Sciences*, *124*(3), 557-563.

[76] Reinholdt, A., Pecenka, R., Pinchuk, A., Runte, S., Stepanov, A. L., Weirich, T. E., & Kreibig, U. (2004). "Structural, compositional, optical and colorimetric characterization of TiN-nanoparticles". *The European Physical Journal D-Atomic, Molecular, Optical and Plasma Physics*, *31*(1), 69-76.

[77] Takada, N., Sasaki, T., & Sasaki, K. (2008). "Synthesis of crystalline TiN and Si particles by laser ablation in liquid nitrogen". *Applied Physics A*, *93*(4), 833-836.

[78] Popov, A. A., Tselikov, G., Dumas, N., Berard, C., Metwally, K., Jones, N., ... & Da Silva, A. (2019). "Laser-synthesized TiN nanoparticles as promising plasmonic alternative for biomedical applications". *Scientific reports*, *9*(1), 1-11.

[79] Barragan, A. J. A. (2019). "*Nanomaterials for Energy Applications: From Photovoltaics to Plasmonic Catalysis"*. University of California, Riverside.

[80] Guler, U., Suslov, S., Kildishev, A. V., Boltasseva, A., & Shalaev, V. M. (2015). "Colloidal plasmonic titanium nitride nanoparticles: properties and applications". *Nanophotonics*, *4*(3), 269-276.

[81] Yick, S., Murdock, A. T., Martin, P. J., Kennedy, D. F., Maschmeyer, T., & Bendavid, A. (2018). "Tuning the plasmonic response of TiN nanoparticles synthesised by the transferred arc plasma technique". *Nanoscale*, *10*(16), 7566-7574.

[82] He, W., Ai, K., Jiang, C., Li, Y., Song, X., & Lu, L. (2017). "Plasmonic titanium nitride nanoparticles for in vivo photoacoustic tomography imaging and photothermal cancer therapy". *Biomaterials*, *132*, 37-47.

[83] Baturina, O. A., Epshteyn, A., Simpkins, B. S., Bhattarai, N., Brintlinger, T. H., Santiago, E. Y., & Govorov, A. O. (2019). "Comparing Photoelectrochemical Methanol Oxidation Mechanisms for Gold versus Titanium Nitride Nanoparticles Dispersed in TiO_2 Matrix". *Journal of The Electrochemical Society*, *166*(10), H485-H493.

[84] Cortie, M. B., Giddings, J., & Dowd, A. (2010). "Optical properties and plasmon resonances of titanium nitride nanostructures". *Nanotechnology*, *21*(11), 115201.

[85] Dong, Z., Wei, H., Chen, Y., Wang, R., Zhao, J., Lin, J., ... & Yu, Y. (2015, October). "Surface enhanced Raman scattering activity of TiN thin film prepared via nitridation of sol-gel derived TiO_2 film". In *AOPC 2015: Advanced Display Technology; and Micro/Nano Optical Imaging Technologies and Applications* (Vol. 9672, p. 967209). International Society for Optics and Photonics.

[86] Ohnishi, R., Takanabe, K., Katayama, M., Kubota, J., & Domen, K. (2013). "Nano-nitride cathode catalysts of Ti, Ta, and Nb for polymer electrolyte fuel cells: Temperature-programmed desorption investigation of molecularly adsorbed oxygen at low temperature". *The Journal of Physical Chemistry C*, *117*(1), 496-502.

[87] Perego, A., Giuffredi, G., Mazzolini, P., Colombo, M., Brescia, R., Prato, M., ... & Casalegno, A. (2019). "Hierarchical TiN nanostructured thin film electrode for highly stable PEM fuel cells". *ACS Applied Energy Materials*, *2*(3), 1911-1922.

[88] Casari, C. S., & LI BASSI, A. (2011). "Pulsed laser deposition of nanostructured oxides: from clusters to functional films".

[89] Bailini, A., Di Fonzo, F., Fusi, M., Casari, C. S., Bassi, A. L., Russo, V., ... & Bottani, C. E. (2007). "Pulsed laser deposition of tungsten and tungsten oxide thin films with tailored structure at the nano-and mesoscale". *Applied surface science*, *253*(19), 8130-8135.

[90] Di Fonzo, F., Casari, C. S., Russo, V., Brunella, M. F., Li Bassi, A., & Bottani, C. E. (2008). "Hierarchically organized nanostructured TiO2 for photocatalysis applications". *Nanotechnology*, *20*(1), 015604.

[91] Willmott, P. R., & Huber, J. R. (2000). "Pulsed laser vaporization and deposition". *Reviews of Modern Physics*, *72*(1), 315.

[92] Ul-Hamid, A. (2018). "*A Beginners' Guide to Scanning Electron Microscopy"*. Springer.

[93] Kim, Y. I., Jeong, S., Jun, B. H., Lee, Y. S., Lee, Y. S., Jeong, D. H., & Lee, D. S. (2017). "Endoscopic imaging using surface-enhanced Raman scattering". *European Journal of nanomedicine*, *9*(3-4), 91-104.

[94] Carden, A., Rajachar, R. M., Morris, M. D., & Kohn, D. H. (2003). "Ultrastructural changes accompanying the mechanical deformation of bone tissue: a Raman imaging study". *Calcified Tissue International*, *72*(2), 166-175.

[95] Mancarella C. "Development of plasmonic gold nanostructures with tunable optical and electrical properties". MA thesis. Politecnico di Milano, 2019.

[96] Gaetani F. "Development of tantalum-doped titanium oxide nanostructures for plasmonic applications". MA thesis. Politecnico di Milano, 2019.

[97] Philips'Gloeilampenfabrieken, O. (1958). "A method of measuring specific resistivity and Hall effect of discs of arbitrary shape". *Philips Res. Rep*, *13*(1), 1-9.

[98] Chan, M. H., & Lu, F. H. (2009). "Characterization of N-doped TiO2 films prepared by reactive sputtering using air/Ar mixtures". *Thin Solid Films*, *518*(5), 1369-1372.

[99] Naik, G. V., Shalaev, V. M., & Boltasseva, A. (2013). "Alternative plasmonic materials: beyond gold and silver". *Advanced Materials*, *25*(24), 3264-3294.

[100] Yang, Z. Y., Chen, Y. H., Liao, B. H., & Chen, K. P. (2016). "Room temperature fabrication of titanium nitride thin films as plasmonic materials by high-power impulse magnetron sputtering". *Optical Materials Express*, *6*(2), 540-551.

[101] Auciello, O., Barnes, T., Chevacharoenkul, S., Schreiner, A. F., & McGuire, G. E. (1989). "Laser ablation deposition of titanium nitride films on silicon substrates at room temperature". *Thin Solid Films*, *181*(1-2), 65-73.

[102] Khan, A. D., Iqbal, J., & ur Rehman, S. (2018). "Polarization-sensitive perfect plasmonic absorber for thin-film solar cell application". *Applied Physics A*, *124*(9), 610.

[103] Deng, H., Li, Z., Stan, L., Rosenmann, D., Czaplewski, D., Gao, J., & Yang, X. (2015). "Broadband perfect absorber based on one ultrathin layer of refractory metal". *Optics letters*, *40*(11), 2592-2595.

[104] Gao, H., Peng, W., Chu, S., Cui, W., Liu, Z., Yu, L., & Jing, Z. (2018). "Refractory ultra-broadband perfect absorber from visible to near-infrared". *Nanomaterials*, *8*(12), 1038.

[105] Taylor, K. J., & Shih, W. Y. (2002). *U.S. Patent No. 6,465,350*. Washington, DC: U.S. Patent and Trademark Office.

[106] Kraus, B. D., Moore, J. T., & Deboer, S. J. (2001). *U.S. Patent No. 6,218,293*. Washington, DC: U.S. Patent and Trademark Office.

[107] McNeil, L. E., Grimsditch, M., & French, R. H. (1993). "Vibrational spectroscopy of aluminum nitride". *Journal of the American Ceramic Society*, *76*(5), 1132-1136.

[108] Yamashita, M., Sasaki, Y., Ito, H., OHSATO, H., & SHIBATA, N. (2006). "Fabrication of aluminum nitride thin film and its oxidation behavior". *Journal of the Society of Materials Science, Japan*, *55*(8), 785-789.

[109] Lee, M. B., Kawasaki, M., Yoshimoto, M., Kumagai, M., & Koinuma, H. (1994). "Epitaxial growth of highly crystalline and conductive nitride films by pulsed laser deposition". *Japanese journal of applied physics*, *33*(11R), 6308.

[110] Chowdhury, R., Vispute, R. D., Jagannadham, K., & Narayan, J. (1996). "Characteristics of titanium nitride films grown by pulsed laser deposition". *Journal of materials research*, *11*(6), 1458-1469.

[111] Torgovkin, A., Chaudhuri, S., Ruhtinas, A., Lahtinen, M., Sajavaara, T., & Maasilta, I. J. (2018). "High quality superconducting titanium nitride thin film growth using infrared pulsed laser deposition". *Superconductor Science and Technology*, *31*(5), 055017.

[112] Johansson, B. O., Sundgren, J. E., Greene, J. E., Rockett, A., & Barnett, S. A. (1985). "Growth and properties of single crystal TiN films deposited by reactive magnetron sputtering". *Journal of Vacuum Science & Technology A: Vacuum, Surfaces, and Films*, *3*(2), 303-307.

[113] Gall, D., Petrov, I., & Greene, J. E. (2001). Epitaxial Sc1−x TixN (001): "Optical and electronic transport properties". *Journal of Applied Physics*, *89*(1), 401-409.